NTNU
Norwegian University of
Science and Technology

Different shaped hybrid nanocarriers for theranostic applications

Anuvansh Sharma

Chemical Engineering
Submission date: June 2016
Supervisor: Wilhelm Robert Glomm, IKP

Norwegian University of Science and Technology
Department of Chemical Engineering

Acknowledgement

I would like to show my sincerest gratitude to my supervisor, Dr. Wilhelm Robert Glomm, Senior Researcher at SINTEF and an Adjunct Professor at NTNU, for the continuous support throughout the course of this thesis. His patience, immense knowledge, insightful comments and motivation have helped me see through tough times. I could not have imagined having a better advisor and mentor for my master's thesis.

Secondly, I am heartily grateful to Mr. Sulalit Bandyopadhyay, PhD student at the Chemical Engineering Department, NTNU, for showing faith in my abilities and encouraging me till the very end. His unparalleled knowledge and mentoring skills have proven to be of huge help in theoretical as well as practical work. This project work would have not seen light had it not been for his insight.

Thirdly, I would like to thank Dr. Gurvinder Singh, Researcher, Department of Materials Science and Engineering for all his help working in the NTNU nanolab as well as his insightful advice. I would also like to show my appreciation to all the people working at the Ugelstad Laboratory and in my study-room for their generous support and for making working at the department fun.

Last but not least, my family, for their ever growing love and undying support.

Thank you all !

Abstract

Nanomaterials have gained a lot of attention in the past few decades as potential candidates for biomedical applications. They are being used as smart drug delivery vehicles among other applications such as wound dressing, tissue engineering, imaging, etc. Both polymeric and inorganic nanoparticles (NPs) are used, out of these materials, hydrogels and gold nanoparticles (AuNPs), have especially caught the global eye in medical field. Hydrogel's affinity towards water make them flexible and soft resembling the living cell tissue, thus rendering them apt for biomedical uses. Other properties like biocompatibility and biodegradability also add to their potential uses. Stimuli responsive hydrogels have provided a possible gateway for a triggered release of loaded material like drug, to the desired location thus, reducing toxicity and undesired side effects. AuNPs possess remarkable imaging and photothermal properties which are being currently exploited in medical research and applications. Hybrid NPs, formed by combining inorganic and polymeric NPs, have gained the attention of researchers around the globe aiming at combining the properties of different nano-systems into one single moiety. Thus, by combining the stimuli-responsive (temperature and pH) properties of hydrogels with the optical properties of AuNPs, a gateway to synthesis of smart NPs can be explored.

In this thesis, five different shapes of AuNPs namely, nanorods (AuNR), tetrahexahedral (AuHex), bipyramids (AuBP), nanomakura (AuNM) and spheres (AuNS), have been synthesized. The anisotropic NPs have been synthesized using a one-pot silver assisted seed-mediated synthesis protocol developed at Ugelstad laboratory, while the AuNS have been synthesized using a modified Turkevich method. The NPs have been characterized using Dynamic Light Scattering (DLS), zeta potential measurements, UV-Visible spectrophotometry (UV-Vis) and Scanning Transmission Electron Microscopy (S(T)EM).

A control study was performed involving three different nanocarrier systems to estimate the effect of incorporation method (incorporation of Fe@Au NPs in hydrogels) on loading and release of Cyt C, a model protein drug. The swelling-collapse properties of hydrogel, in situ grown hydrogels atop Fe@Au NPs (Fe@Au_insitu) and hydrogel coated Fe@Au NPs (Fe@Au_coated) were mapped using DLS. Fe@Au_coated showed an increase in size upon heating from 25°C to 45°C,

Abstract

resembling the behavior of Fe@Au NPs, while Fe@Au_insitu collapsed (volumetric collapse efficiency ~ 94%) under similar conditions, resembling the behavior of the hydrogels. These three systems, hydrogel, Fe@Au_insitu and Fe@Au_coated were thereafter loaded with Cyt C and showed high loading efficiencies (L.E.s) of 96%, 86% and 78% respectively. Release of the drug was monitored over a period of 48 hours under conditions of high temperature (45^OC) and low pH (3.5). Fe@Au_coated hybrid NPs showed the highest release (34%) while hydrogel and Fe@Au_insitu showed ~ 12% release. Release kinetics showed anomalous transport for hydrogel systems which converted to super case-II transport with the incorporation of Fe@Au NPs.

Following the success of Fe@Au_coated NPs in drug release, all the five AuNPs were coated with PEG, followed by hydrogel. The increase in the size of NPs with successive PEG and hydrogel coating was observed from the DLS measurements. This was further supported by the decrease in zeta potential of anisotropic AuNPs resulting from the successful replacement of cationic CTAB by PEG and hydrogel. The effect of varying temperature and pH on the hybrid NPs was studied by changing the temperature from 25^OC to 45^OC and pH from 9 to 3. The systems showed maximum volumetric swelling/collapse at 45^OC and pH 3, with smaller particles (AuNS and AuNR) showing collapse and larger particles (AuBP and AuNM) showing swelling; forming the basis for using the same conditions for monitoring release.

The effect of amount of hydrogel on Cyt C L.E. and release of the drug was investigated. The AuNPs were coated with two different weights of hydrogel (1.67 mg and 3.3 mg). The NPs were loaded with Cyt C using breathing in technique. The L.E. for all the NPs increased with increased hydrogel content. The effect was stronger in smaller NPs (AuNR, AuHex and AuNS). Drug release study was conducted using a dialysis based setup at 45^OC and 3.5 pH. The percentage of drug released over a period of 48 hours increased over two folds for these NPs. While for AuBP and AuNM, a marginal increase in size was observed. Finally, the release data were fitted to different kinetic models. The selected models were zero order, first order, Higuchi and power law. For NPs coated with 1.67 mg hydrogels, the release transport was governed by the NPs (super case-II) similar to the case with hydrogel incorporated with Fe@Au NPs. With increasing hydrogel concentration of the coated AuNPs to 3.3 mg, the transport mechanism shifted to anomalous

Abstract

regime and was dominated by the hydrogel for smaller NPs (AuNR, AuHex and AuNS). The shift was less for AuBP and AuNM which stayed in the supper case-II transport mechanism region.

Table of Contents

Table of Contents

Table of Contents

List of figures

List of figures

List of figures

List of figures

List of tables

1. Introduction

Nanotechnology is the science that deals with particles of the size of a billionth of a meter. By working at this small a scale provides a control over the properties of the macroscopic material by making alterations at the molecular level [1]. Thus, by carefully choosing the synthesis and assembly process for these nanoparticles (NPs), one can design the final product having specifically desired chemical and physical properties which can further be used for defined applications such a medicine [2, 3], catalysis [4], electronics [5], etc.

The use of NPs in the field of medicine has lately gained immense importance. Their effective size along with their ability to be multi-functionalized possess a great variety of advantages in various medical applications, namely; cancer therapeutics, antimicrobial actions, vaccine delivery, gene delivery and site-specific targeting to avoid the undesirable side effects of the current therapeutics [6].

In January, 2000, the National Nanotechnology Institute announced the advent of nanoscale science and engineering on a global scale. Recent advancements in the field of biosystems research has established one of the most dynamic science and technology realms at the convergence of physical sciences, molecular engineering, biology, biotechnology and medicine. This included a better understanding of the living and thinking systems, revolutionary biotechnology processes, synthesis of new drugs and their targeted delivery, regenerative medicine and developing a sustainable environment [7].

The delivery of drug to its desired target site still remains one of the most challenging tasks in the medicine industry due to poor solubility, cytotoxicity, poor biodistribution and selectivity towards target tissues [8]. Thus, drug delivery is gaining fast pace interest worldwide and attracting researchers from all over the globe. Pharmaceutical firms and biotechnology industries are investing heavily in their research divisions in order to arrive at a novel way to transport the drugs efficiently and effectively to the desired target sites. Delivery of the drug is not the sole issue. Effective loading and release of the drug is also an important factor in effective drug targeting. The drug is loaded in the NPs, which then act as transport vehicles for the drug. These vehicles

1. Introduction

must prevent detection by the human immune system in order to avoid expulsion from the body. This poses another immense challenge in the design of these carriers.

In the following sections, types of nanoparticles used as payload carriers have been described. The sections also shed light upon the importance of gold nanoparticles (AuNPs) in the field of medicine. The effect of anisotropy as well as the growing significance of hybrid nanoparticles have been discussed.

2. Nanocarriers in Biological Applications

Various methods have been applied in synthesizing different types of nanocarriers. These nanocarriers are designed and functionalised according to their desired application. Two different kinds of nanoparticles that exist in medical applications, inorganic and polymeric, will be discussed in the following sections.

2.1 Inorganic NPs

Inorganic NPs are usually opted as they provide optical, magnetic or catalytic features. Their properties are considerably different from their bulk materials [9]. The properties become discrete at the level of quanta rather than being continuous over the bulk of the material [10].

2.1.1 Gold NPs

Metallic NPs being synthesised in extremely small sizes have larger surface areas. This characteristic enables greater quantities of drug to be loaded over the surfaces of these NPs. Among these, AuNPs have managed to attract the maximum attention owing to their marked benefits. Besides simple, reliable and inexpensive synthesis methods, AuNPs offer good control over shape and size. Additionally, AuNPs have a rich surface chemistry that enables them to be used for a variety of applications just by tuning the surface groups. They can be easily functionalized with different biomolecules such as citrate, amine, nucleic acid, peptide and lipid ligands [11]. They are also biocompatible and nontoxic [12]. Figure 1 shows alkylthiol-terminated oligonucleotide functionalised AuNPs for the use of intracellular gene regulation [13].

Figure 1 Oligonucleotides functionalized AuNPs[13].

Antibodies such as Vascular Endothelial Growth Factor (VEGF) have been attached to AuNPs, showing a marked increase in the apoptosis of B-Chronic Lymphocytic Leukemia (CLL) cells [14]. A protein found in humans, ubiquitin, has been shown to interact successfully with the Au NPs [15]. Increase in the hydrodynamic radius of the system as well a shift in the plasmon resonance band of Au confirmed the successful interaction of the protein with AuNPs in this study.

2.1.2 Magnetic NPs

Magnetic NPs (MNPs) have been used extensively for biotechnological and biomedical applications. The ability to be used for specific site targeting is one of their greatest asset. A successful use of this property would lead to reduced cytotoxic effect of the drug at undesired locations, thereby increasing the efficacy of the drug. This in turn would automatically reduce the required dosage of the drug [16]. Magnetic iron oxide particle with no coating possesses a hydrophobic surface having larger area-volume ratio. Thus, the system aims to lower the surface area and results in agglomeration of the particles forming large clusters. Increased particle size results in loss of intrinsic superparamagnetic properties and initiates the opsonization process [17]. Fe based MNPs, functionalized with glyceryl mono-oleate (GMO), successfully showed dual drug

loading [18]. Paclitaxel and rapamycin were loaded with entrapment efficiency of about 95% to fight against breast cancer cells. These nanocarriers can be functionalized using copolymers such as poly-ethylene glycol (PEG), chitosan and poly-ethylene imine. An *in vitro* study demonstrated loading and release of 6-mercaptopurine (6MP), a thiol containing anticancer drug, using poly(N-isopropylacrylamide-co-maleic anhydride-g-S-S-py) grafted FeNPs [19]. Surface modified with pullulan coated superparamagnetic iron oxide NPs showed reduced toxicity as well as enhanced cellular uptake [20].

2.1.3 Silicon NPs

These nanocarriers are gaining fast pace importance in biomedical applications for therapeutic as well as diagnostic imaging due to the property of luminescence. Partly due to their biodegradability, SiNPs undergo efficient renal clearance. Besides this, high porosity and a suitable surface chemistry makes them ideal nanocarriers [21]. Functionalized hollow mesoporous SiNPs have gained focus in molecular imaging [22]. Organically modified SiNPs are attaining interest as potential nanoprobes [23]. Silica core-PEG-amino shell NPs showed low cytotoxicity with persistent fluorescent signal depicting cellular uptake. This method can be utilized for cell traceability and detection [24]. A fluorescence study confirmed release of dye from pH responsive polymer functionalized SiNPs [25].

2.1.4 Silver NPs

They prove to be good against skin infections due to their anti-microbial characteristic [26]. Highly luminescent glutathione protected silver nanoclusters (AgNC) of size less than 2 nm were synthesized. These showed antimicrobial properties against multidrug resistant bacteria, Pseudomonas aeruginosa, by generating a high concentration of intracellular reactive oxygen species [27].

2.2 Polymeric NPs

The characteristic features of most polymeric NPs, i.e. biodegradability and biocompatibility, have attracted the interest of researchers in developing these NPs as effective drug delivery systems. Apart from these features, they show excellent surface modification and functionalization with different ligands along with admirable pharmacokinetic control. They depict good encapsulation and deliverability for numerous therapeutic drugs such as Cytochrome-C, L-dopa, Coumarin, etc. Their structure depends on the synthesis process employed and can be nanospheres or nanocapsules [28].

2.2.1 Solid Lipid NPs
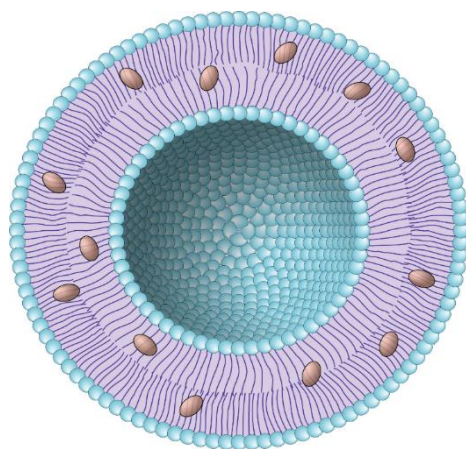
Figure 2 Liposomes [29].

Liposomes are spheres comprising at least one lipid bilayer (Figure 2). Usually, they are composed of phospholipids, especially phosphatidylcholine [30]. Solid Lipid NPs coated with PEG, which provides stealth ability to the particle, helps evading the reticuloendothelial system (RES) [31]. The ethylene oxide (EO) groups are hydrophilic and extend into the solution thereby shielding the surface of the particle [32]. The extended PEG chains contract as the opsonins approach the particle surface. This results in a more condensed and a higher energy conformation. Thus, an opposing force is generated which counter balances the attractive force between the opsonin and the particle surface.

2.2.2 Polymeric Micelles

Polymeric micelles are block copolymers having both hydrophilic as well as the hydrophobic monomer units [33]. Their structure represents a corona formed by hydrophilic chains enclosing a core of hydrophobic chains. Usually, PEG is used as the polymer to enclose the core, although other hydrophilic polymers can be used. The length of the chains forming the core is usually less than the corona chain lengths [34]. Figure 3 shows a micellar representation.
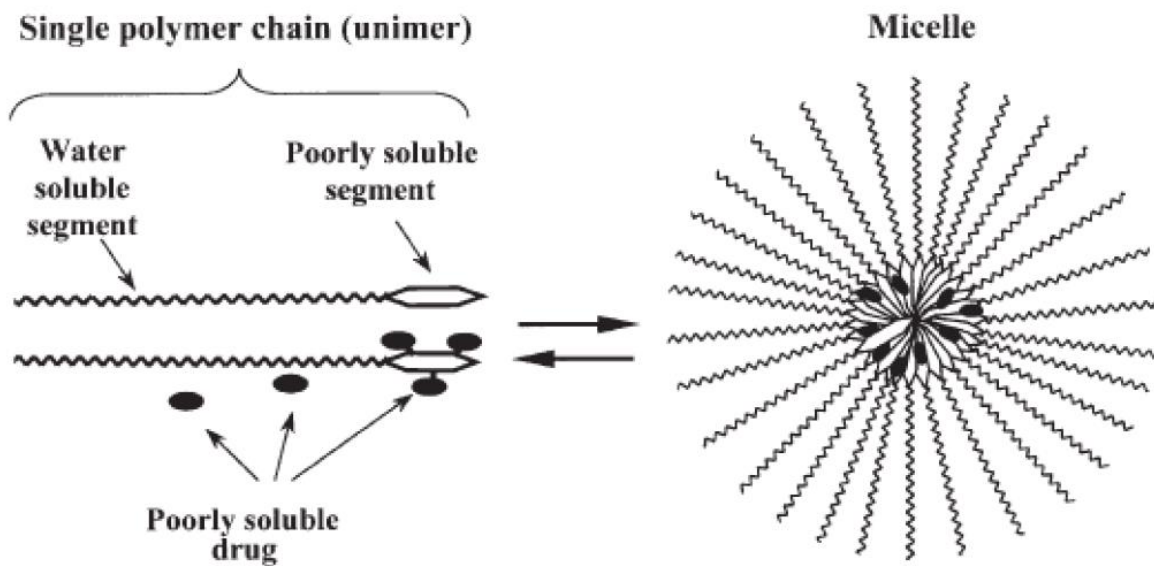
Figure 3 Polymeric Micelle[33].

2.2.3 Dendrimers

Another category of polymeric NPs is dendrimers. The word dendrimer originates from the Greek word 'dendra', meaning reminiscent of a tree. Their structures depict a number of symmetric branched monomers emanating radially outward from a central core. Out of the many dendrimers such as polyamidoamines (PAMAMs), polyamines, polyamides (polypeptides), poly (aryl ethers), polyesters, carbohydrates and DNA, PAMAM dendrimers are mostly used [35], [36]. Figure 4 represents a typical dendritic structure.
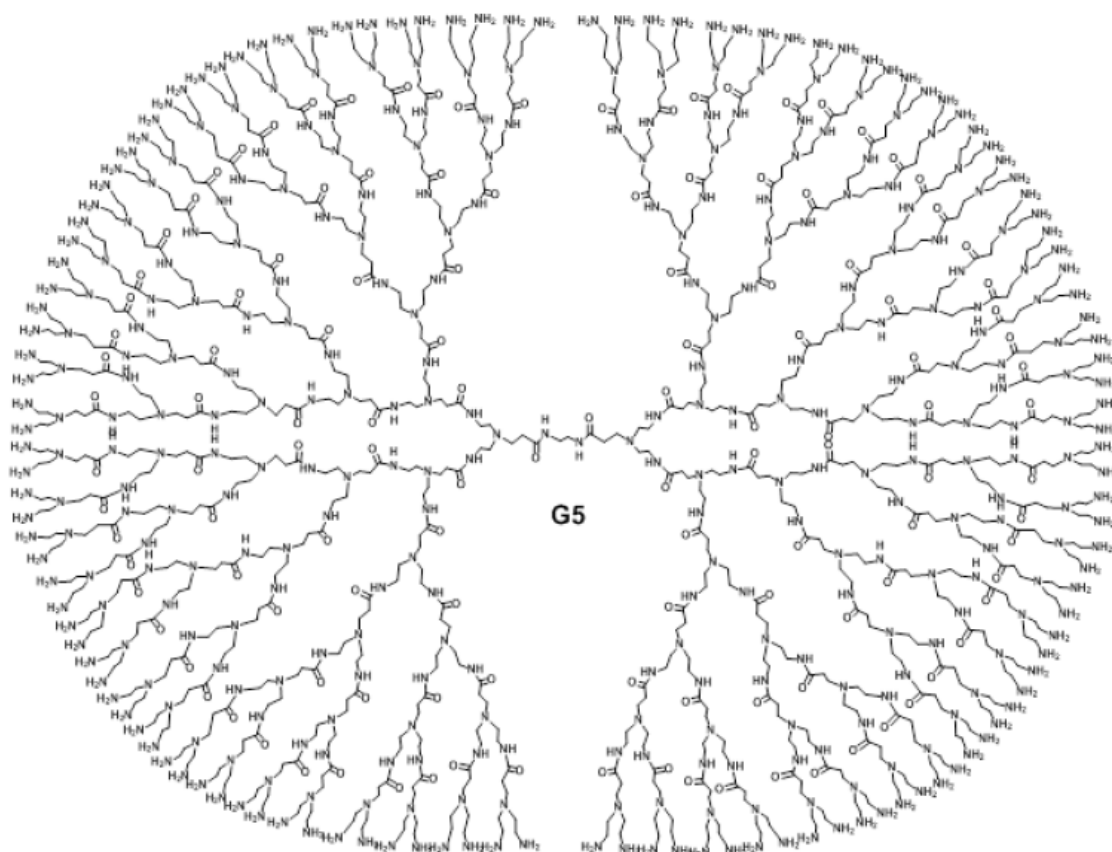
Figure 4 Dendrimer[37].

2.2.4 Hydrogels

The last couple of decades has seen a massive rise in the search for smart and intelligent materials for the use in medical science. Among these, hydrogels in particular have caught the attention of researchers around the globe. As everything inside the human body is a complex mixture of substances, interfacial properties become extremely important in governing the applicability of a foreign substance and avoid its rejection. Hydrogels are three dimensional, porous structures having a high affinity for water. They are rendered insoluble due to the crosslinking in the polymer chains. The crosslinking can be due to entanglements or crystallite structures or due to hydrogen bonding. Due to their porous nature, water can enter the polymer's network forming swollen structures of hydrogels [38]. This water retention capability as well as biocompatibility make

hydrogels one of the most sought after materials in biomedical applications [39]. They transform into soft and rubbery matter resembling the living tissue thereby exhibiting excellent biocompatibility [40].

As hydrogels have been used extensively within the scope of this thesis, different types of hydrogels as well as their characteristic properties have been discussed in detail in Chapter 4.

3. Gold Nanoparticles

3.1 AuNPs in Medical Applications

As mentioned in the previous section, gold has proven to be one of the most promising candidate for biomedical applications. Its unique characteristic of allowing itself to be multi-functionalized, as shown by Figure 5, has diversified its use in different fields.
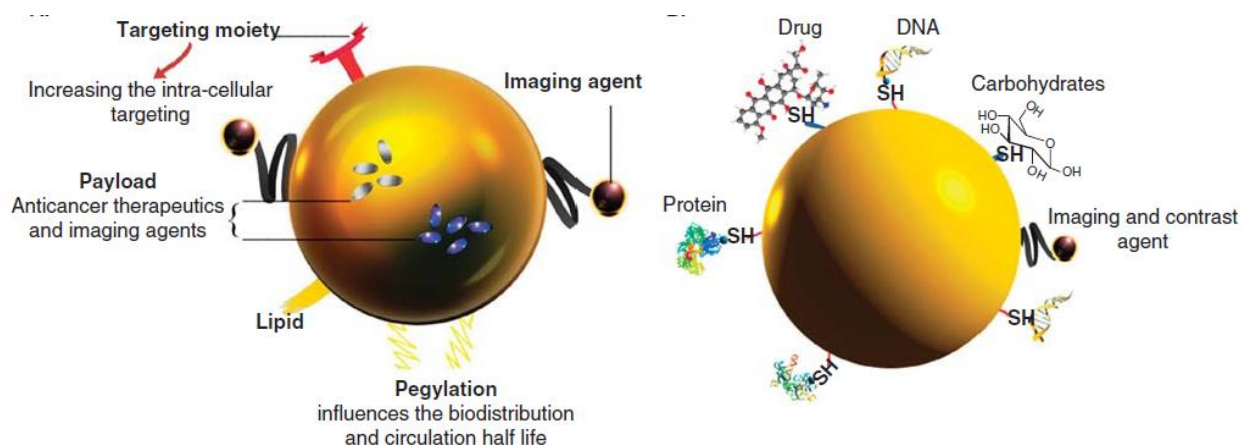
Figure 5 Schematic depicting multifunctional nature of AuNPs[41].

One highly recognizable property of AuNPs is the localized surface plasmon resonance (LSPR). For AuNPs, having radius much smaller than the incident light's wavelength ($r/\lambda < 0.1$), a fluctuating electric field causes oscillation of electrons in the conduction band. Thus, the particle surface becomes polarized. A repulsive force is generated due to the Coulombic attraction to bring back the displaced electron cloud. This creates a resonance condition at a particular frequency. A dipolar field is generated at the surface of the NPs which is responsible for increased absorptions, cattering cross-sections and greatly enhanced electromagnetic fields near the particle surface. This phenomenon is known as LSPR (Figure 6).
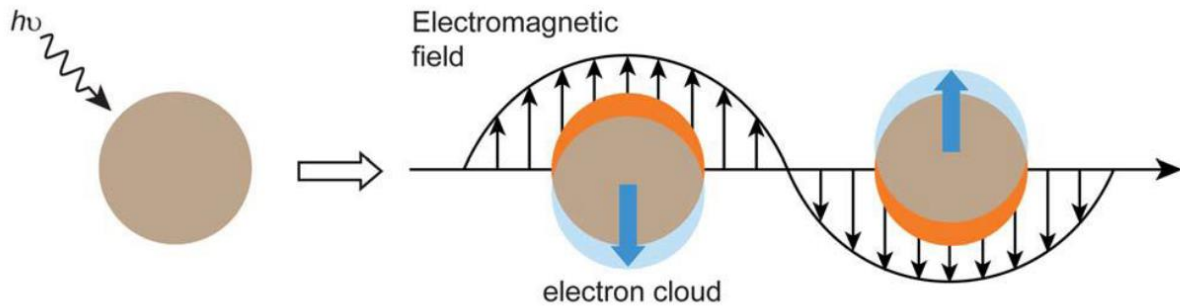
Figure 6 LSPR shown by AuNPs [42].

Au shows an LSPR band near around 520 nm and is dependent on the particle shape and size [43]. LSPR depends on the particle size, the electron density as well as the dielectric constant of the surrounding medium and usually increases with all these factors. It also depends on the geometry of the NPs. Generally, an increase in the aspect ratios (defined as ratio of length to diameter) enhances LSPR. Figure 7 shows the variation in the LSPR of Au NPs with different sizes.
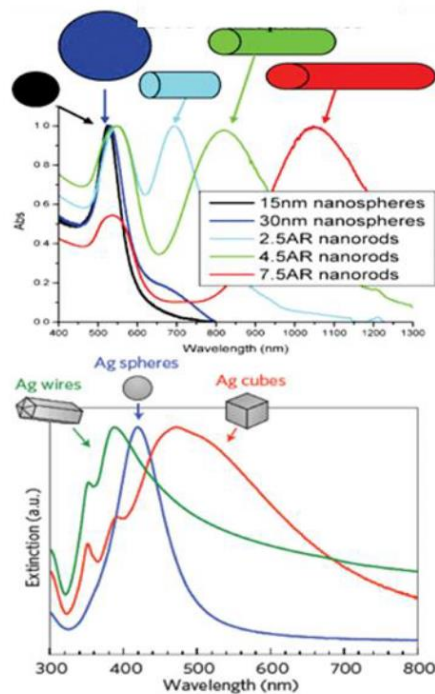
Figure 7 LSPR shown by different shaped AuNPs [44].

3. Gold Nanoparticles

Some of the applications of AuNPs have been discussed in the following section.

3.1.1 Diagnostics

AuNPs have been used as *in vivo* radioactive since 1950s and have expanded their usage to immuno-AuNPs associated to antibodies for biological staining in electron microscopy since the 1980s. AuNPs possess numerous advantages over quantum dots and organic dyes when it comes to diagnostics such as [45]:

- reduced or no toxicity
- better contrast agents for imaging as compared to organic dyes that suffer from rapid photobleaching
- surface-enhanced and refractive index-dependent spectroscopic properties.

Gold Nanorods (AuNRs) can strongly absorb and scatter near infrared region (NIR) and find tremendous applications in cancer cell imaging (Figure 8) [46]. This property is also used in fluorescence microscopy. Multiphoton luminescence of AuNPs has been utilized to carry out *in vitro* imaging of embryonic stem cells [47]. The process of inelastic Raman Scattering has been used for probing of molecular structures but its extremely small cross sectional area ($\sim 10^{-30}$ to $\sim 10^{-25}$ cm^2) limits its uses when it comes to ultrasensitive trace detection. However, the phenomenon of LSPR in AuNPs enhances the signals of the molecules attached to them in an effect known as the surface enhanced Raman scattering (SERS) [48]. Silica gold core-shell NPs have been used for high resolution biomedical imaging technique known as the optical coherence tomography (OCT). It interferometrically measures the amplitude as well as echo time delay of the backscattered light to generate cross-sectional and 3-D images of tissue microstructures [49].

3. Gold Nanoparticles
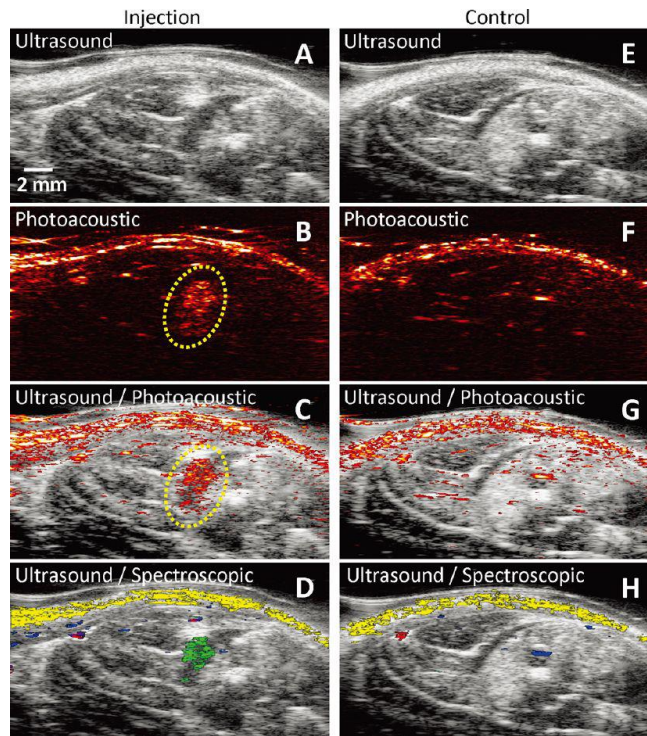
Figure 8 In-vivo photoacoustic imaging of stem cells via labelling with AuNPs. (A-D) with injection, (E-H) without injection [50].

AuNPs are extensively used as contrast agents. PEG coated AuNPs have been studied in X-ray Computed Tomography (CT) in mice as blood-pool contrast agents. The NPs were 38nm in size and the AuNPs-PEG proved to be biocompatible in mice without any toxicity [51]. Even smaller sized AuNPs (1.9nm) used as X-ray contrast agents have shown to have longer retention times than iodine based agents [52]. LSPR based optical biosensors have been used as biomarkers for Alzheimer's disease [53]. Electrochemical impedance spectroscopy (EIS) using ferrocene-peptide conjugate AuNP single-walled carbon nanotube (SWCNT) has been used to detect HIV-1 protease [54]. Thiolated oligonucleotide functionalized AuNPs have been used for the identification of Mycobacterium Tuberculosis DNA [55].

3.1.2 Therapeutics

Cancer is probably one of the deadliest and hence one of the most dreaded diseases of current times. Early detection and early treatment is the only way to survive it. Here, nanoscience proves

to be a boon in cancer treatment. Small AuNPs can be synthesized which can easily cross the blood brain tumor barrier (BBTB) and be expelled from the body [56]. The biocompatibility of the NPs can be enhanced by functionalizing with PEG which further decreases rapid clearance by the reticuloendothelial system (RES) [57]. These PEGylated AuNPs have been used for photodynamic therapy of cancer [58]. NPs as small as 5nm have shown to treat human gastrointestinal cancer cells (Panc-1 and Hep3B) by thermal destruction using non-invasive radiofrequency [59]. Formation of new blood vessels from old ones is termed as Angiogenesis. However, in cancer cells abnormal angiogenesis takes place which is a primary reason for cancer growth as it provides the cells with oxygen and nutrients. Spherical AuNPs have shown to hinder angiogenesis by binding to the heparin-binding growth factor thus, preventing the new cells to be formed [60]. They have also been used to eliminate bacteria. _Staphylococcus aureus_ is a pathogen causing diseases such as septic arthritis, endocarditis, osteomyelitis, etc. 10, 20 and 40nm AuNPs have been shown to kill the bacteria by photothermal approach [61].

3.1.3 Theranostics
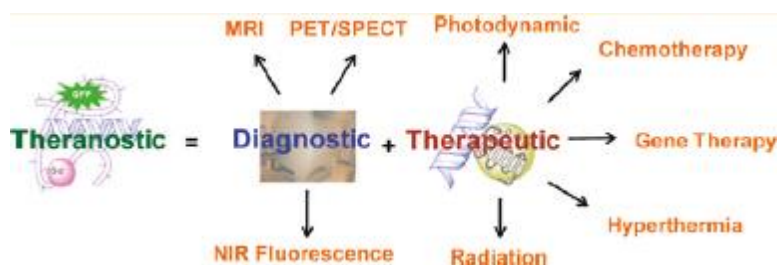
Figure 9 The meaning of theranostics [62].

The term theranostics is a portmanteau of therapeutics and diagnostics (Figure 9). Thus, the NPs can be used for both the applications simultaneously. Two strategies are involved in therapeutic targeting in cancerous tissues. First is 'passive targeting', which exploits the enhanced permeability and retention effect (EPR) as shown in Figure 10. The blood vessels present in the tumor are leaky, defective, dilated and irregularly shaped. Also, the endothelial cells are poorly aligned with numerous fenestrations. The wider lumen of tumor vessels along with poor lymphatic drainage of tissues allows blood plasma components to leak inside the tumor [63]. The macromolecular drugs circulating in the blood stream accumulate near the cancer cells and are

taken up by the cells [64]. The second approach is 'active targeting' in which the surface of the drug carrier is functionalized with a ligand having affinity to the desired target site [65].
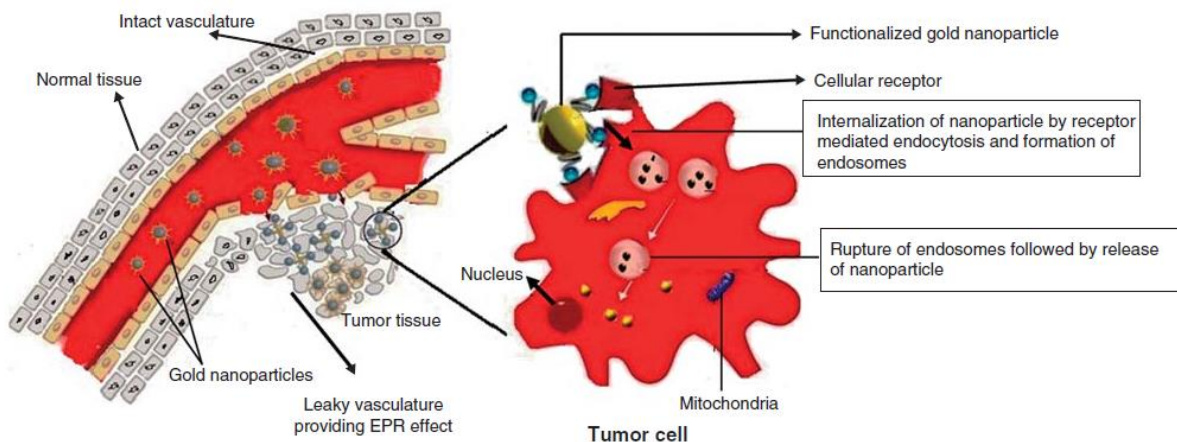
Figure 10 Schematic showing passive targeting[41].

PEG is used for passive targeting as it reduces interaction with cells and prolongs circulation time by preventing clearance by the RES [66]. Bifunctional PEGs are generally used enabling the attachment of a targeting ligand thus, combining the shielding effect of PEG as well as active targeting by the ligand. PEGylated surface functionalized AuNPs with paclitaxel drug and biotin receptors have been used for cancer therapy [67]. PEG-AuNPs have been coated with stimuli responsive polymers which can be triggered by changes in the surroundings such as temperature, pH, light, etc. One such thermo-responsive polymer is N-isopropylacrylamide (pNIPAm) hydrogel. Techniques like irradiation by NIR laser can cause a collapse in the hydrogel thereby releasing the drug load [68].

Among other metals, AuNPs are primarily used for hyperthermia due to their unique feature of SPR. The excited oscillating electrons decay via releasing heat [69, 70]. The absorption of light at by biological fluorochromes and water is low at NIR wavelengths. Thus, light can easily penetrate much deeper into the tissues without causing any harm to the healthy cells in the surroundings [71]. Iron oxide@Au core-shell NPs have been exploited widely in order to combine the benefits of imaging and therapeutics. Au coating shields the magnetic NPs, such as magnetite (Fe_2O_4) and

maghemite (γ-Fe_2O_4), from aggregating and masks their cytotoxicity [72]. Magnetic field-directed hyperthermia is a therapeutic technique in which the iron oxide NPs impart high T_2 relaxivity and can be localized to a desired site in the presence of a magnetic field [73]. Using this technique, Au nanoshell coated iron oxide NPs have been successfully shown to cause significant damage to SKBR3 breast cancer cells as shown in Figure 11 [74, 75].
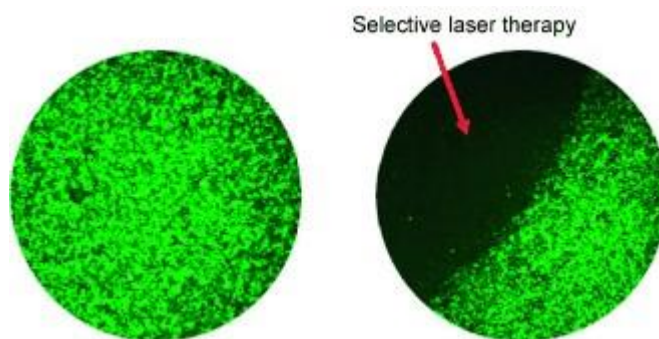
Figure 11 SKBR3 cells incubated with the targeted HGNS (Fe2O3@Au) and stained with calcein-AM (green). Irradiation with an 808 nm laser resulted in a significant decrease in survival of treated cells [75].

Nanorods have shown to have few advantages over nanospheres. They show drastic reduction of plasmon damping exhibition significantly narrower linewidths at comparable frequencies than spherical NPs [76]. They have been shown to possess highest thermal gradients thereby converting light energy into heat as compared to nanospheres [77]. This property can be utilized for hyperthermia treatments. Thus, effect of anisotropy on NP properties is discussed in the following section.

3.2 Effect of Anisotropy

AuNPs in specific shapes like nano-rods, nano-stars, nano-cages and nano-shells show localized surface plasmon resonant properties that strongly favour their applicability in oncology. Differently shaped AuNPs exert different photothermal characteristics which have been exploited for the use of AuNPs as cytotoxic agents [78].

3. Gold Nanoparticles

As already stated, AuNPs through excitation of LSPR strongly couple with light. Along with localization and enhanced electromagnetic (EM) field, this novel phenomenon of enhanced coupling at nanoscale level can be utilized for energy transport and storage [79], sensors and spectroscopies with increased sensitivities [80], controlled growth of NPs through enhanced optical forces [81], photovoltaic devices with improved light absorption [82], photothermal destruction of cancer cells and pathogenic bacteria [83, 84] among other applications.
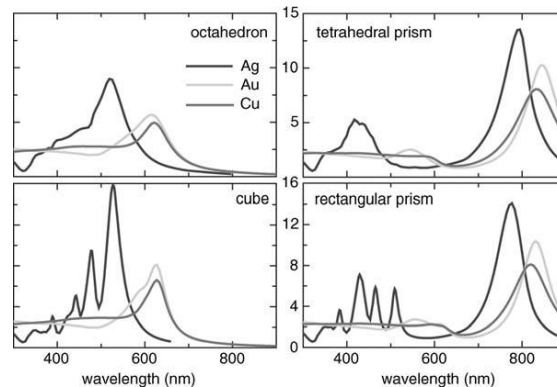
Figure 12 Extinction efficiencies as a function of wavelength for different NP morphologies[78].

In case of spherical NPs, the displacement of charge is homogeneous which leads to a dipolar charge distribution at the surface. This results in one kind of resonance which is independent of the direction of incident light as well as NP size thus giving rise to one proper mode. However, the resonance is dependent on the NP shape as multifaceted NPs possess multipolar charge distribution. For instance, ellipsoidal NPs having three axes possess tensor polarizability with three different dipole modes thus giving rise to three plasmon resonances corresponding to the three axes [85]. Figure 12 shows the effect of different morphologies on the extinction efficiency. Therefore, the aim for searching the most novel plasmonic structures is to seek particles or array of particles yielding the strongest EM enhancement. Larger enhancement factors are possible with narrower gaps between NPs as well as sharp edges, corners and tips of AuNPs [86].

Another property which is affected by the morphology of NPs is Raman scattering. Most of the photons which are scattered by an atom or a molecule are elastically scattered, known as Rayleigh

scattering. The scattered photons have the same energy as of the incident photons. A very minute fraction is scattered inelastically, thereby changing the frequency of the scattered photons. The phenomenon of inelastic scattering was observed by C. V. Raman and is known as Raman scattering as shown by Figure 13 [87]. Although the phenomenon holds great importance and tremendous use, one of its limitation is an extremely low scattering cross section area (~ 10^{-29} cm^2). But, this has shown to be improved by absorption of Raman active molecules onto a rough metal surfaces, resulting in surface-enhanced Raman scattering (SERS) [88, 89].
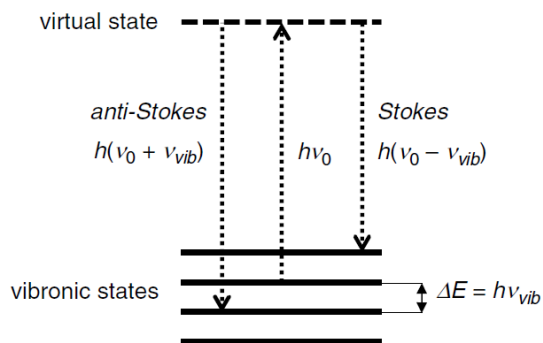
Figure 13 Schematic illustrating the quantum mechanical description of Raman scattering [90].

AuNPs demonstrate high absorption and generate heat upon stimulation by light. This phenomenon can be enhanced when the frequency of incident light hits the plasmon resonance of the metal. This effect has been used for photothermal applications in medicine such as imaging and sensing [91, 92], tissue welding [93], and destruction of tumour cells [94]. Thus, different morphologies are important since plasmon resonance frequencies strongly depend on geometry of NPs [95].

3.3 Isotropic and Anisotropic AuNPs

As discussed in previous section, asymmetry results in enhanced properties when compared to isotropic spherical particles. In this section, nucleation and growth of spherical NPs is first discussed. Thereafter, different methods that can be used to synthesize anisotropic gold are outlined. Finally, various operating mechanisms that underlie the transition of spherical seed NPs into anisotropic structures are discussed.

3. Gold Nanoparticles

3.3.1 Nucleation and Growth of NPs

More than one molecule exists in a metallic crystal lattice. The molecules in the bulk have saturated bonds as they are well surrounded by neighboring atoms. While on the surface, there exist some dangling bonds which increase the overall surface energy of the system. The growth of a particle happens in such a way that it acquires a morphology with the least surface energy. As Wulff describes it, the rate of growth of crystal facets is proportional to their respective surface energies [96]. Synthesis of NPs starts from generation of supersaturation- driving force for nucleation. Once the nuclei are formed then crystal growth happens resulting in the formation of the final NPs.

3.3.1.1 Nucleation

There are two kinds of nucleation namely, homogeneous and heterogeneous. In homogeneous nucleation, there is no solid interphase which assists nucleation. Nucleation occurs when the concentration of the metal precursor in the solvent reaches supersaturation. This supersaturated solution is energetically unstable and tend to separate out into atoms. Upon reaching a critical value, the metal atoms in the solution start to form clusters thereby releasing energy in the process. The Gibb's free energy associated with the critical radius of the NP is as follows:

$$\Delta G_{crit} = \frac{16\pi\gamma^3}{3(\Delta G_v)^2} = \frac{4\pi\gamma r_{crit}^2}{3}$$

Where,

ΔG_v = free energy change of the transformation per unit volume

γ = interfacial tension

r_{crit} = minimum size of a stable nucleus

The rate of nucleation is defined by the Arrhenius equation as follows:

$$J = A\exp\left(\frac{-\Delta G}{k_B T}\right)$$

Where,

J = rate of nucleation, number of nuclei formed per unit time per unit volume

k_B = Boltzmann constant

Homogeneous growth is depicted by LaMer plot in Figure 14 describing the three stages- stage I: induction period, stage II: nucleation period, stage III: growth period. The region below S is known as the stable zone where nucleation is impossible. The region between S_c and S represents the metastable zone. Here, spontaneous nucleation is improbable, but seed mediated growth is possible. In the region above S_c, uncontrollable nucleation takes place and is known as the liable zone [96].
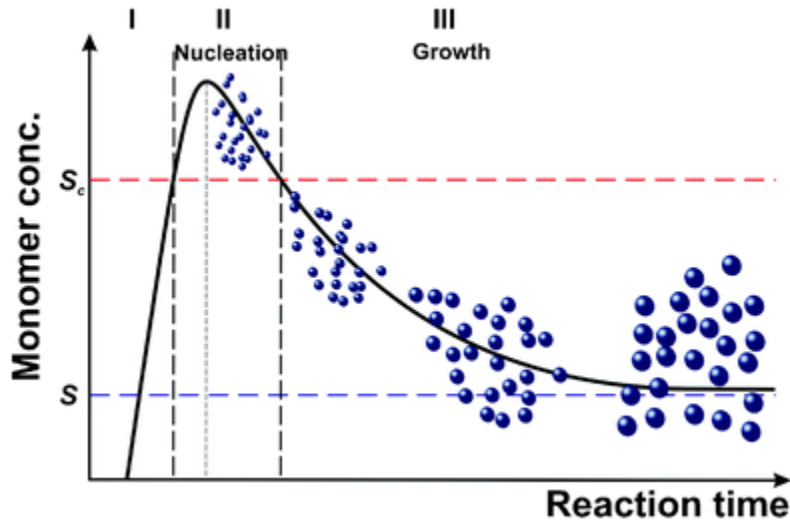
Figure 14 LaMer plot describing nucleation and growth of colloidal particles [97].

While in the case of heterogeneous nucleation, nucleation takes place at preferential sites such as edges, corners or grain boundaries, preexisting foreign bodies or solid structures. By nucleating on these surfaces, energy is released due to the elimination of preexisting interfaces. Moreover, heterogeneous nucleation occurs at lower supersaturations as compared with homogeneous nucleation [98].

3.3.1.2 Growth of NPs

As soon as a stable nucleus is formed under supersaturation conditions, it starts to grow. There are many theories explaining the possibilities of NP growth. In the diffusion-reaction theory, the growth is considered to be a two-step process. First is the diffusion step, in which the particles are transported from the bulk phase to the solid surface. Second is the reaction step, in which the

3. Gold Nanoparticles

particles arrange themselves into a crystal lattice by first order reaction. The diffusion and reaction terms are defined as [99]:

$$\frac{dm}{dt} = k_d A(c_s - c_i) \qquad \text{(diffusion)}$$

$$\frac{dm}{dt} = k_r A(c_i - c^*) \qquad \text{(reaction)}$$

Where,

m = mass of the solid deposited in time t

k_d = diffusion mass transfer coefficient

k_r = surface reaction rate constant

c_s = solute concentration in solution at supersaturation

c_i = solute concentration in solution at crystal-solution interface

c^* = equilibrium saturation concentration

A generalized equation based on the overall driving force can be written as:

$$\frac{dm}{dt} = K_G A(c_s - c^*)^g$$

Where,

K_G = overall crystal growth coefficient

g = order of crystal growth process

      g = 1, transport (diffusion)/surface adsorption

      g = 2, surface integration

      g > 2, surface nucleation [100]

Another growth theory describes crystal growth by screw dislocations. The surface of most crystals contains dislocations which results in step formation and promotes growth. Growth by screw dislocations obviates the necessity of surface nucleation. The curvature of the spiral is governed by the critical radius for a two-dimensional nucleus under supersaturation conditions [99]. Growth by screw dislocations is shown by Figure 15.
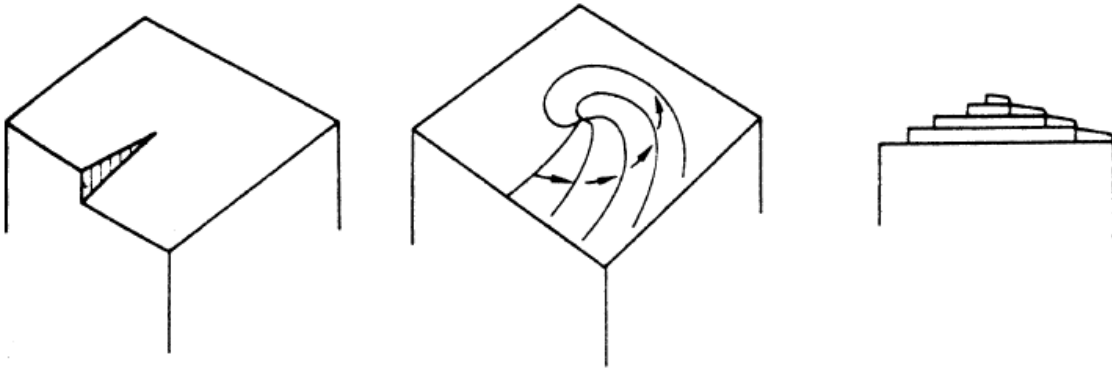
Figure 15 Crystal growth by screw dislocation [99].

At high values of supersaturations, the crystal grows by the mechanism of 2-D nucleation. The addition of new moieties occurs at regions of greatest attraction. This results in a stepwise build-up of the surface until the whole face is completed. In order for further growth, additional centre of crystallization should appear on the surface. It was suggested a step edge is created rather than the creation of a new surface [101]. The growth then proceeds from this two-dimensional nucleus as depicted by Figure 16.
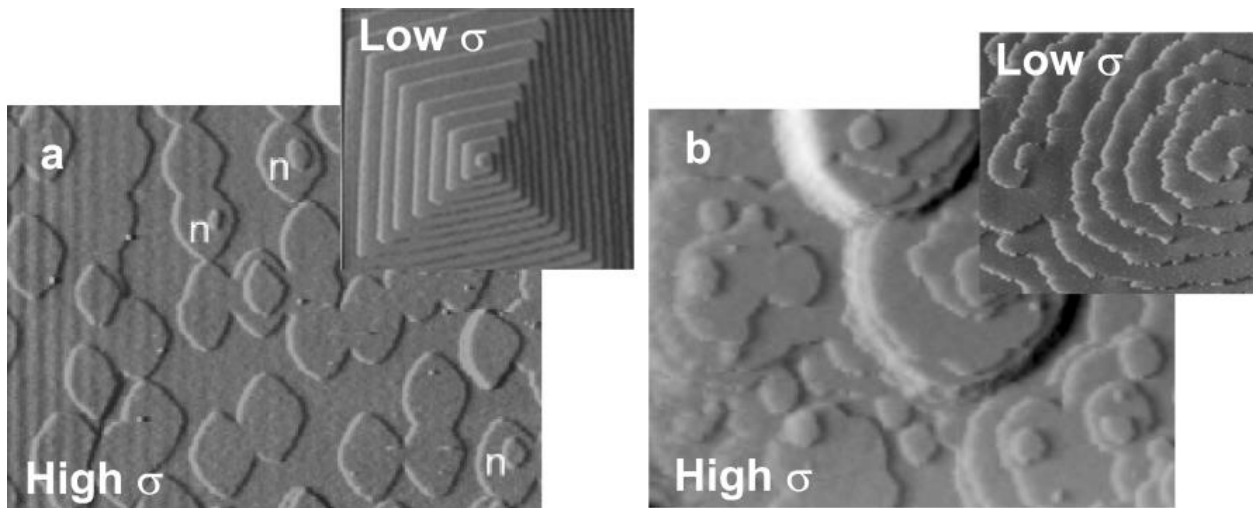
Figure 16 Crystal growth by 2-D nucleation at high supersaturation [101].

3.4 Methods of Synthesis

Numerous methods have been used for the synthesis of AuNPs. Some of these have been discussed in the following sub-sections.

3.4.1 Template-based Approach

The template-based approach allows synthesis of NPs within the pores of a nanoporous membrane. The electro-templating approach relies on the reduction of the metal at the cathode. The electrolyte solution contains the ions of the desired metal and a potential is applied across the solution. The cathode comprises of a preformed template where the nucleation and growth of the NPs takes place. The reduction process eventually leads to the bottom-up growth of 1-D NPs in the pores of the membrane templates. This method provides efficient length and composition control [102]. Gold nanowires can be synthesized using this technique as shown in Figure 17.
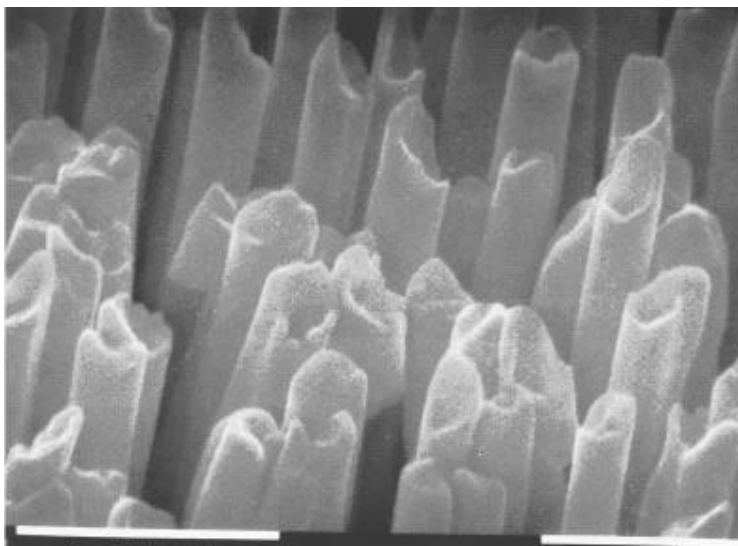
Figure 17 Template-based synthesis of gold nanowires [102].

3.4.2 Seed-mediated Approach

The seed-mediated process involves addition of preformed fine metal particles (seeds) to the growth solution allowing crystal growth. The seed particles are usually formed by reduction of the metal ions by a suitable reducing agent. Different shapes and sizes can be obtained by varying the

quantity of the seed. The seeds can be same or different than the metal in the solution. As the nucleation and growth processes are discrete in seed-mediated process, flexibility over control of final particle morphology is achieved. Ag has been successfully shown to assist growth of AuNPs. Although, the effect caused by Ag is not clear, other nitrates have not been able to cause growth in AuNPs [103]. AuNPs have been synthesized without the assistance of Ag as well. But, in the latter approach even though the yield is low, nanorods with higher aspect ratios can be achieved [104].

3.4.3 Seedless-based Approach

Seedless synthesis approach has also gained popularity. This method is based on surfactant-templated process. The surfactant guides the shape of the growing crystal. Small NPs having tetrahedral and octahedral shapes are formed on using high surfactant concentrations [105]. Although several methods exist for synthesis of anisotropic AuNPs, it is not clear how these grow from seeds. In the next section, different medium of growth in case of seeded approach will be discussed. CTAB has been successfully used as a potential surfactant for synthesizing Au nanorods.

3.5 Growth Mechanisms

Some of the proposed growth mechanisms taking place in the growth of NPs have been discussed in this section. AuNRs synthesized by template assisted synthesis process follow a relatively easier methodology. However, the process becomes complex when there is no template or inherent crystallography anisotropy. Seed-mediated method using citrate stabilization has been used successfully for the synthesis of AuNRs. The newly developed side surfaces can be stabilized using an additive such as hexadecyltrimethylammonium bromide (CTAB) [106]. Murphy and coworkers proposed that steric as well as chemical factors determine the preferential interactions between cationic quaternary ammonium head groups of CTAB and the growth sites on the lateral edges and faces of AuNRs. The Au atoms get attached to the {111} face ends while the surfactant molecules glue themselves to the {100} ends. The CTAB molecules attach themselves as a bilayer on the surface of the NRs and grow along with the rods, thus giving rise to a zipping like mechanism providing additional stability as shown in Figure 18 [107].
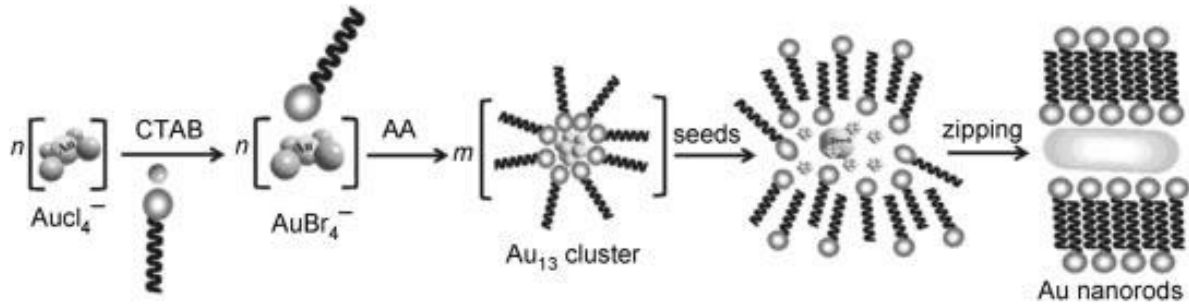
Figure 18 Possible mechanism of AuNRs formation [108].

Small quantity of $AgNO_3$ is also needed for AuNR synthesis using seed-mediated stabilized by CTAB. The yield control as well as the aspect ratio can be drastically improved by this method. Even though the presence of $AgNO_3$ improves the yield and good control over NR length over a small range, its role in the growth is yet not clear. It has been proposed that the structures have slowly growing {110} sides and fast growing {100} ends [109].
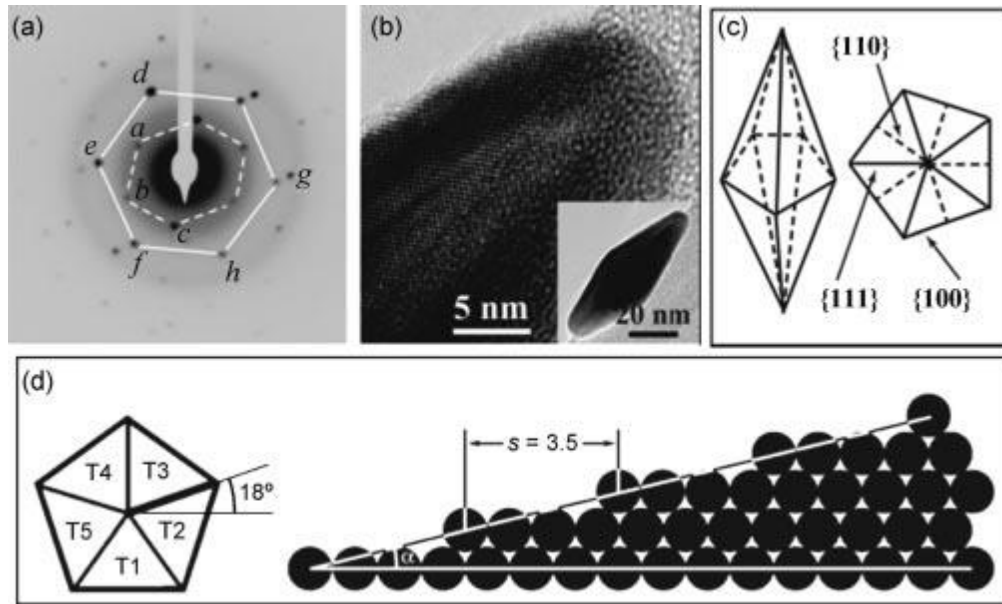
Figure 19 HRTEM of bipyramid AuNPs and the growth process arising from the pentatwinned shape [109].

Similar to AuNRs, bipyramid NPs also have been synthesized by citrate-stabilized seed-mediated process [110]. They have also been synthesized without the use of seeds in the presence of polymer PVP in ethylene glycol [111]. However, in the seed-mediated growth, the yield of these NPs is one-third of the total particles. Characterization studies show that bipyramids form from pentatwinned seeds and are pentatwinned around the long axis [109, 112]. Thus, their formation is quite similar to pentatwinned AuNRs. The primary difference arises due to the presence of steps on the {100} Au side facets along the growth direction. Due to these steps, the {100} side facets tilt towards the {111} facets thereby producing bipyramid structures as shown in Figure 19.

4. Hydrogels

In this section, the various types of hydrogels have been discussed. Different examples of natural and synthetic hydrogels have been cited with emphasis on their applications. Finally, their physical and chemical properties have been discussed with major emphasis on gelling properties.

4.1 Natural Hydrogels

These hydrogels are naturally occurring materials derived from plants and animals. The commonly used natural or biological hydrogels have been discussed below.

4.1.1 Hyaluronate

Found in the natural extracellular matrix (ECM), hyaluronate (HA) is one of the non-sulphated glycosaminoglycan components [113]. It differs from its synthetic counterparts in that it is biologically active. It is capable of absorbing enormous quantities of water due to the presence of negative charge and thus, swelling to 1000 times in volume. This hydrated network acts as a sieving barrier controlling the movement of water as well as preventing pathogen, plasma proteins and proteases movement [114]. Due to higher affinity towards oxygen derived free radicals, HA acts as an antioxidant.

In order to improve the structural stability of HA, it has to be covalently crosslinked. Crosslinking can be achieved by using various components such as bisepoxide [115] or divinyl sulfone [116] derivatives in alkaline medium and glutaraldehyde, 1-ethyl-3-(3- dimethylaminopropyl) carbodiimide hydrochloride (EDC), biscarbodiimide and multifunctional hydrazides in acidic medium (Figure 20). EDC crosslinked HA has been used in tissue engineering [117]. HA hydrogel based Restylane®, is being successfully finding applications in tissue augmentation [118]. In another study, HA along with fibroblast growth factor-2 and a potent mitogen were combined to achieve bone/fracture healing properties [118].
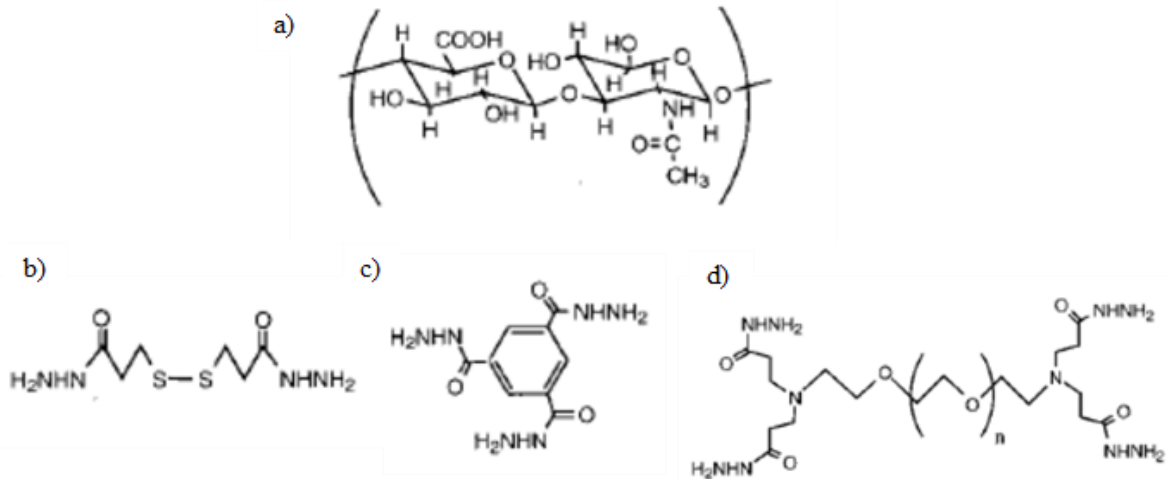
Figure 20 (a) Structure of hyaluronic acid. Various crosslinking molecule for hydrogel (b) 3,3¢-dithiobis(propanoic dihydrazide) (c) 1,3,5-benzene(tricarboxylic trihydrazide) (d) poly(ethylene glycol)-diamine tetrapropanoic tetrahydrazide [119].

4.1.2 Fibrin

The advantage of fibrin is that it can be synthesized from the patient's own blood. Thus, it rules out any toxicity as well as inflammatory reactions. It is used as a sealant and an adhesive playing a crucial role in wound healing [119]. Alginate modified fibrin hydrogels have been used for chondrocyte culture which is further used in cartilage transplants [120]. Chondrocyte culture has been done both, *in vitro* and *in vivo* [121]. In another culture study conducted related to cardiovascular tissue, human myofibroblasts were harvested in fibrin aided by a protein drug, aprotinin [122]. Figure 21 depicts a structure of fibrin.
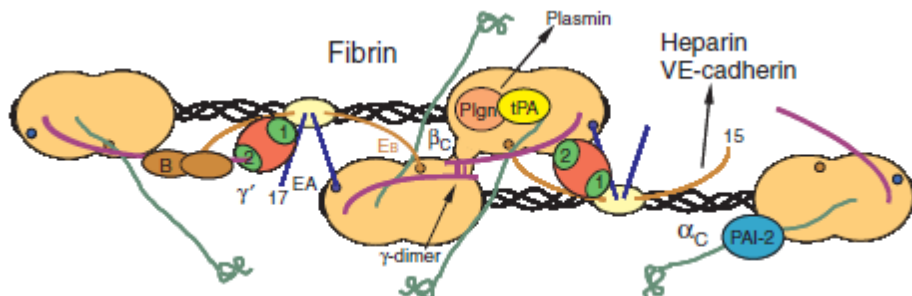
Figure 21 Fibrin structure [123].

4. Hydrogels

4.1.3 Agarose

A marine algal polysaccharide, agarose, forms thermally reversible hydrogels. Successful neuron growth was achieved by a modified agarose-chitosan hydrogel [124]. Agarose, alone has poor cell adhesion. This limitation is overcome by the chitosan molecule. Thus, agarose based hydrogels can be utilized for neural tissue repair. Cell migration and proliferation is supported by the large pores and low mechanical strength of the agarose hydrogel. In another neural study, oligopeptide domain, CDPGYIGSR, was covalently bonded to the agarose hydrogel showing neurite outgrowth from dorsal root ganglia [125]. Figure 22 shows a structure of agarose.
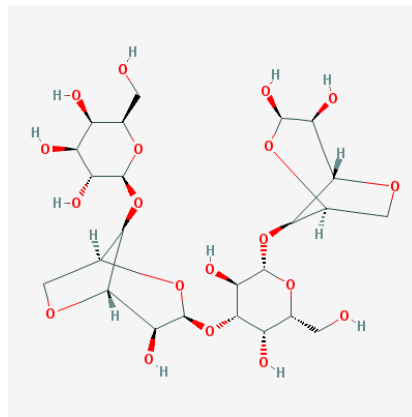
Figure 22 Structure of agarose.

4.1.4 Alginates

Obtained from brown algae such as *Laminaria-digitata* [126], *Ascophyllum-nodosum*, and *Macrocystis pyrifera*, it is a widely known biomaterial. It finds application in biomedical field due to its features as biocompatibility, low toxicity, lower cost and simple gelation. Divalent crosslinking solutions containing either Ca^{2+}, Sr^{2+}, or Ba^{2+} can be used to extrude a solution of sodium alginate having the desired protein. Monovalent ions and Mg_{2+} are unable to induce gelation in alginates. Other divalent cations such as Pb^{2+}, Cu^{2+}, Cd^{2+}, Co^{2+}, Ni^{2+}, Zn^{2+} and Mn^{2+}, are limited in use due to higher toxicity [127]. Alginate/chitosan hydrogels, crosslinked with N,N′-dicyclohexylcarbodiimide (DCC), have been shown to enhance cell attachment [128]. Alginates,

being a negatively charged polysaccharide, enables scaffolding for cell growth on a positively charged chitosan system. In another tissue engineering study, nano-/microfibers of titanium dioxide (nfTD) and hydroxyapatite (nfHY) modified with alginates successfully showed enhanced cell adhesion [129].

D-Mannuronic Acid Residues   L-Guluronic Acid Residues
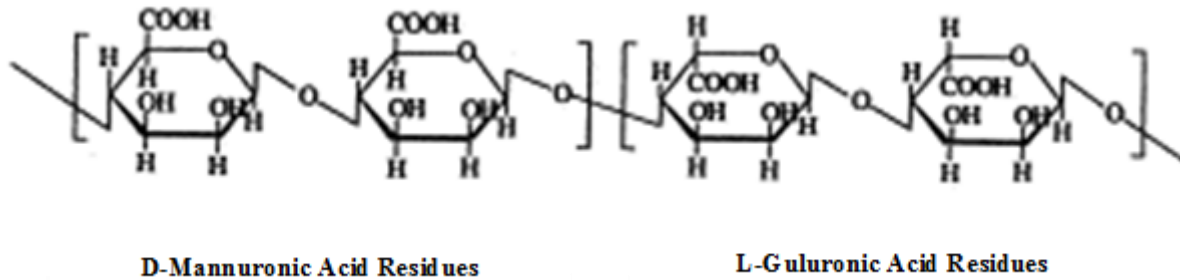
Figure 23 Structure of alginic acid copolymer [130].

4.1.5 Collagen and gelatin

Being the primary component of the extracellular matrix of the mammalian tissue such as skin, bone, cartilage, tendon, and ligament, collagen is the most widely used tissue derived natural polymer. However, collagen has a few shortcomings such as poor physical strength, potentially immunogenic, expensive and inconsistent when produced in batches. Some of these limitations can be overcome by modifying the collagen structure using fibronectin, chondroitin sulphate and hyaluronic acid. Successful attachment and growth of cell fibroblasts was achieved with these modified systems [131]. This approach can be extended for use in tissue engineering as therapeutic option for the treatment of burn patients or chronic wounds [132]. Dynamic mechanical modification can be done by glycation and the system used for improving the mechanical properties of the collagen-gel blood vessel constructs [133].

Another derivative of collagen, gelatin, also finds medical applicability. There are two modes of gelatin preparation. The acid treatment gives gelatin A whereas alkaline treatment results in gelatin B [134]. Gelatin B has a higher percentage of carboxylic group due to the conversion of amide residues of glutamine and asparagine into glutamic and aspartic acid respectively [135]. Gelatin-

alginate sponge, crosslinked with 1-ethyl-3-(3- dimethylaminopropyl) carbodiimide (EDC), has been shown to be a good material for skin replacements [136].

4.1.6 Chitosan

Chitosan is a linear polysaccharide that comprises randomly arranged β-(1-4)-linked Dglucosamine and N-acetyl-D-glucosamine units (Figure 24). It is widely produced by progressive deacetylation of chitin [137]. Chitin, being the second most abundant natural biopolymer after cellulose, is a structural element in the exoskeleton of crustaceans and insects. The nitrogen content in a chitosan molecule is greater than 7% [138]. Due to the presence of amino groups, it can be protonated by selected acids. A chitosan/glycerophosphate solution showed thermally reversible gelling property, gelling at a temperature of 37^OC [139]. This can be used as a potential drug delivery vehicle. Chitosan hydrogels were synthesized by crosslinking using genipin and release study were carried out with albumin [140]. It was seen that with increasing crosslinking density, the drug delivery time can be extended significantly, thus, finding application in drug delivery. Azide and lactose moieties crosslinked chitosan has been synthesized by UV irradiation [141]. This resulted in a higher biologically adhesive hydrogel and lactose improved its water solubility.
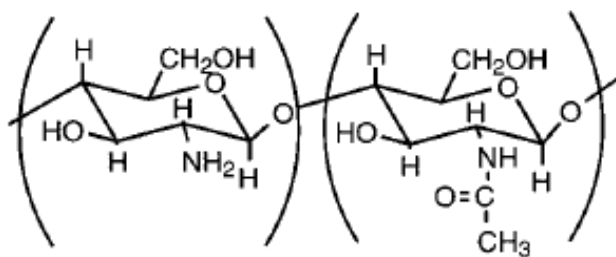
Figure 24 Structure of chitosan [119].

4.2 Synthetic Hydrogels

Synthetic hydrogels are progressively replacing natural hydrogels due to their higher water absorption capacity, long service life, and wide varieties of raw chemical resources. Some of the most common synthetic hydrogels have been discussed below.

4.2.1 Poly-hydroxyethyl methacrylate (PHEMA).

PHEMA finds usage in biomedical application as contact lenses [142] and in drug delivery [143]. The latter utilized UV light and photo-initiators for the solution polymerization PHEMA and diethylene glycol dimethacrylate (DEGDMA). Features like optical transparency, stability in water and mechanical properties make it a contender for application in medical field. It has been shown through radical polymerization, HEMA modified with dextran can be used for designing hydrogels for pulsed drug delivery [144]. PHEMA has also been used for applications in tissue engineering. Microcapsules of HEMA with methyl methacrylate (MMA) were synthesized using submerged nozzle–liquid jet extrusion technique [145].

4.2.2 Poly-vinyl alcohol (PVA)

PVA is another widely used synthetic polymer. Semi-crystalline PVA hydrogels have been synthesized by electron beam irradiation [146]. PEG, along with PVA, have been photopolymerized using UV light for cartilage tissue engineering applications [147]. Cyclic freezing and thawing process has been used to synthesize PVA hydrogel [148]. In order to find applicability, PVA must be crosslinked, which can be achieved by chemical, irradiative or physical mechanisms. Some of the common cross-linkers used are glutaraldehyde, acetaldehyde, formaldehyde, and other monoaldehydes. Acetal bridges form between the pendent hydroxyl groups of the PVA chains in the presence of sulfuric acid, acetic acid or methanol. However, getting rid of the residual cross-linker is extremely important and tedious as it might have undesirable side effects. Irradiation methods prove to be of advantage in such cases as they do not leave any potentially toxic residue. In addition to that, photopolymerized hydrogels have been synthesized for tissue engineering applications [149].
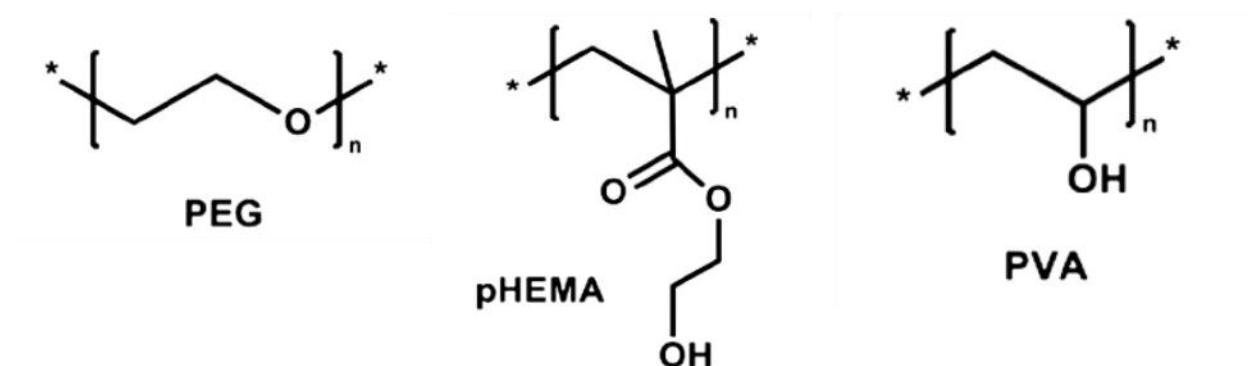
Figure 25 Some commonly used substances for synthetic hydrogels [150].

4.2.3 PEG based Hydrogels

Also known as a stealth material, due to its inertness towards most biological molecules, PEG helps in preventing detection. This property was studied by E. W. Merrill, as early as 1982. He showed that PEG adsorbed on a glass substrate repels protein molecules [151]. West presented a photo polymerization method to synthesize crosslinked PEG hydrogel, copolymerized with α-hydroxy acid, with acrylate at the terminal ends [152]. More common synthesis routes involve covalent bonding via silanes, acrylate and thiol, ionic and hydrogen bonding [153, 154]. PEG offers immense flexibility when it comes to modifying the hydrogel for the desired applications. It can be modified to induce degradation or cell adhesion. When derivitized with peptide containing arginylglycylaspartic acid (RGD), photo-polymerized crosslinked poly-(PEG)diacrylate have been shown an adhesion of up to 50% [155]. In contrasting studies, peptide Ala-Pro-Gly-Leu was co-polymerized with PEG to achieve biodegradable polymeric biomaterials [156].

4. Hydrogels

4.2.4 Poly-N-isopropylacrylamide (pNIPAM)

pNIPAM based systems are the most widely studied systems for temperature responsive hydrogels. These systems undergo reversible volume phase transition with a variation in temperature, known as volume phase transition temperature (VPTT). This behaviour is analogous to the polymer's phase separation temperature, called as lower critical solution temperature (LCST). pNIPAM exhibits a VPTT of around 32-33°C [157]. Table 1 shows the LCSTs of a few other compounds.

Table 1 LCST of different polymers in water [157].

Polymer	LCST ($^\circ$C)
Poly(N-isopropylacrylamide), PNIPAM	~32
Poly(vinyl methyl ether), PVME	~40
Poly(ethylene glycol), PEG	~120
Poly(propylene glycol), PPG	~50
Poly(methacrylic acid), PMAA	~75
Poly(vinyl alcohol), PVA	~125
Poly(vinyl methyl oxazolidone), PVMO	~65
Poly(vinyl pyrrolidone), PVP	~160
Poly(silamine)	~37
Methylcellulose, MC	~80
Hydroxypropylcellulose, HPC	~55
Polyphosphazene derivatives	33–100
Poly(N-vinylcaprolactam)	~30
Poly(siloxyethylene glycol)	10–60

Stimuli responsive feature depends primarily on the side chain functional groups, branches and crosslinks. Networks containing weekly acidic or basic pendent groups can be ionized by altering the solution's pH or ionic concentration. Acrylic acid is one such pendent group. Indomethacin release was studied in vitro conditions using pNIPAM monomer along with vinyl terminated polydimethylsiloxane (VTPDMS) macromers [158]. The study showed that the release was negligible at pH of 1.4 over 24 hours and over 90% at pH 7.4 when studied for over 5 hours. Methylene-bis-acrylamide (MBAAm) was used as a crosslinker.

pNIPAM based systems are the most widely studied systems for temperature responsive hydrogels. These systems undergo reversible volume phase transition with a variation in temperature, known as volume phase transition temperature (VPTT). This behaviour is analogous to the polymer's phase separation temperature, called as lower critical solution temperature (LCST). pNIPAM exhibits a VPTT of around 32-33°C [157]. Table 1 shows the LCSTs of a few other compounds.

4.3 Physico-chemical Properties of Hydrogels

Various physical and chemical properties of hydrogels make them a strong contender for biomedical applications. These properties can be tuned in ways depending on the application for which the hydrogel would be used. Some of these properties have been discussed in the following section and how they contribute to the application of hydrogel systems in the medical and pharmaceutical industry.

4.3.1 Refractive Index

Refractive index (RI), described as the ratio of the speed of light in vacuum to the speed in the material, is an important parameter when dealing with optics. For ophthalmological applications, hydrogels need to have a high refractive index. Also, high water content (~65%) is required to mimic the natural lens [159]. As stated earlier, hydrogels possess high affinity towards water, but huge amounts of water could compromise the mechanical stability and strength of the hydrogel. Thus, they need to be modified for this purpose. Water has a low RI, and a RI of 1.35 has been reported for a porcine collagen hydrogel system containing 90% water [160].

Low RI is undesirable as it requires thicker optical lens to account for the proper refractive power. High RI Inorganic nanoparticles have been successfully incorporated in the polymer network to increase the RI of the system. ZnS:Mn/PMMA nanocomposites have been used to make highly transparent acrylic glasses with a transmittance of 87% [161]. Interpenetrating polymer network (IPN) hydrogels have been synthesized with improved RI and high water content. Covalently linked ZnS nanoparticles/PHEMA and poly-acrylic acid (PAA) based polymer networks were synthesized into an IPN yielding RIs of 1.65 (dry) and 1.49 (hydrated), with a water content as high as 60.2% [161].

4.3.2 Turbidity

Another interesting feature shown by hydrogels is turbidity. These systems tend to swell or collapse in response to various stimuli changes, as reported later. pNIPAM, for example, undergoes collapse at a temperature of 32^OC [162]. They aggregate on collapsing resulting in macroscopic phase transition. This further results in an opaque system, the degree of which can be measured as the transmittance of light. They also undergo sol-gel transition which too can be measured in terms of turbidity [163].

4.3.3 Stimuli Response

Perhaps one of the most important properties of the hydrogels is their ability to swell and collapse when exposed to various stimuli changes like temperature, pH, light, etc. This feature has been widely exploited for targeted drug delivery applications. Also, the hydrogels showing response to specific entities such as glucose, can be used as biosensors. One of the key hurdles faced is the slow response time, which can be improved by synthesizing thinner and smaller hydrogels. But, this could lead to a compromise in the structural strength of the hydrogels. Thus, efficient design and novel polymers and cross-linkers are needed to achieve biocompatibility and desired biodegradability [164]. The swelling-collapse behaviour is defined in terms of swelling ratio. People have defined this parameter in many ways such as the ratio of volume of swollen gel in water to the volume of dry gel [165], or the weight of hydrated hydrogel to the weight of the dry hydrogel [166]. In the scope of this thesis, the swelling ratio is used to determine the VPTT of the hydrogel. This is crucial in order to determine the drug release conditions.

4.3.3.1 Temperature Sensitivity

As most of the application of hydrogels is in vivo, it is crucial to design their response properties close to the human body temperature. pNIPAM is one of the widely used thermosensitive polymers as stated in the previous section. Due to its lower critical solution temperature (LCST), which is the temperature at which the polymer shows solubility in the solvent, in the range of 25-32°C, Poly-N,N-diethylacrylamide (PDEAAM), is also widely used. This change in phase is known as volume phase transition (VPT), and the temperature at which it occurs is known as volume phase

transition temperature (VPTT). LCST is characteristic property of a monomer while VPTT is determined for cross-linked polymer chains.

The collapse at higher temperature is due to the presence of hydrophobic groups, whose interactions increase with increasing temperature while hydrophilic interactions decrease resulting in a shrunk hydrogel system. The LCST of the system can be changed by playing with the hydrophilic/lyophilic balance (HLB) of the groups. Usually, a decrease in LCST is seen with increasing hydrophobic groups [167]. Few systems undergo a sol-gel phase transition instead of a swelling-collapse behavior, for instance, poly-ethylene oxide (PEO) and poly-propylene oxide (PPO).

4.3.3.2 pH Sensitivity

Hydrogel systems containing acidic or basic groups are the ones which trigger a pH related response. The swelling is caused by electrostatic repulsion due to the ionization of these groups. The groups ionize at high pH thus increasing the size, whereas the basic groups undergo the opposite effect. By using different basic hydrogels such as methyl methacrylate (MMA), ethyl methacrylate (EMA), butyl methacrylate (BMA), and N,N-dimethylaminoethyl methacrylate (DMA), it was shown that by either increasing the pendent side chain length or the crosslinking density, there is a reduction in the pH sensitivity as well as the swelling capability [168]. In another contrasting study, the effect of the covalent cross-linker, tetraethylene glycol dimethacrylate (TEGDMA), was found to be insignificant, but depended upon the amount of MAAc in the poly-HEMA-co-MAAc hydrogel [169].

4.3.4 Cross-linking

Polymers can be crosslinked by physical or chemical means. They can also be crosslinked using UV radiation or other chemical means but are advisable only if there is a possibility to remove the toxic reagents before hydrogel administration into the body. *In vitro* gelation may result in hindrance to various routes of injection due to increase in viscosity. Thus, it is preferred that the liner polymer chains gel after administration into the body thereby prolonging drug release [170].

4.3.4.1 Physical Cross-linking

Physical crosslinking can be achieved by many ways such as hydrophobic interactions, hydrogen bonding or charge interactions. In hydrophobically attained linking, an amphiphilic polymer is used containing both, a hydrophilic as well as a hydrophobic part. Hydrophilic interactions dominate at low temperatures, but their effect is reduced as the temperature increases. At higher temperatures, the hydrophobic chains start arranging themselves so as to reduce water contact increasing the solvent entropy.
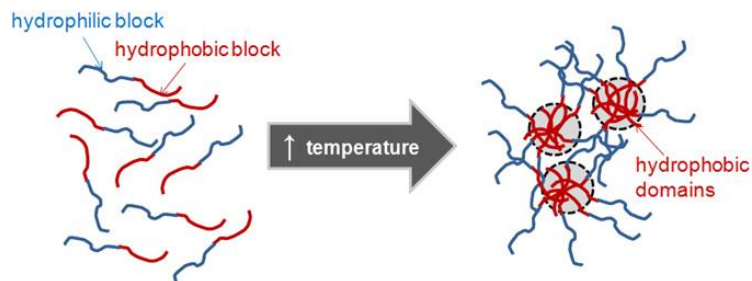
Figure 26 Gelation caused by hydrophobic interactions [170]).

The advantage of crosslinking by charged interactions is the biodegradation of the hydrogel as the ionic species in the extracellular matrix break down the hydrogel's cross linking. The crosslinking can also be caused by varying the pH as the ionic functional groups would ionize or protonate. Polymer chains can be crosslinked by a small molecule as achieved by elastin like polypeptide containing lysine, crosslinked by an organophosphorous cross-linker, β-[tris(hydroxymethyl)phosphino]propionic acid (THPP) [171]. These were successfully loaded with fibroblasts and showed the same encapsulation even after 3 days. In a polymer-polymer chemical crosslinking, ionic peptides with alternating positive and negative charges self-assemble to form gels [172].
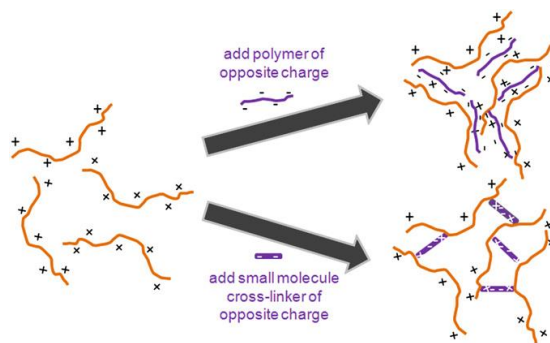
Figure 27 Gelation by charged interactions [170].

Ionic crosslinking was achieved for quaternized chitosan and glycerophosphate with a successful release of doxorubicin hydrochloride as a function of pH [173]. The third type of physical cross linking is by hydrogen bonding. Agar-gelatin were crosslinked in this fashion and release study was carried out for theophylline (TPH). HA and methylcellulose (HAMC) based hydrogel showed possibility as a promising drug delivery system to the spinal cord [174]. The only limitation of hydrogen bonding is that it can be disrupted in vivo due to the influx of water, thus restricting their use for short-acting drug carriers.
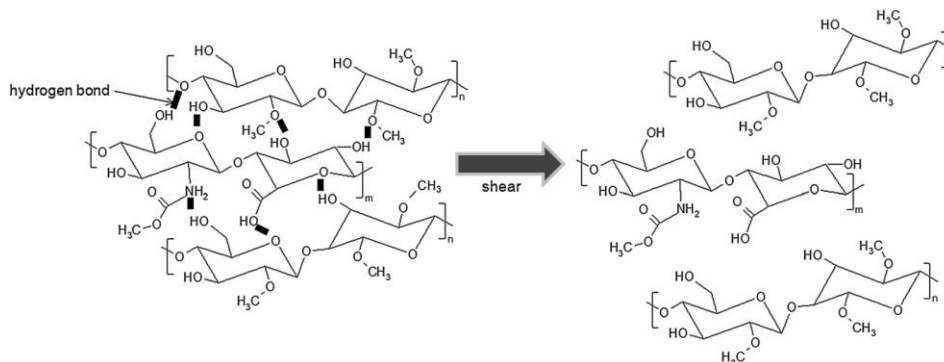
Figure 28 Gelation through hydrogen bonding [170].

4.3.4.2 Chemical Cross-linking

Even though physically crosslinked hydrogel systems have an advantage of not utilizing the chemical moieties, they pose some limitations. They undergo dilution and dissipation thereby reducing the tissue dwelling times. These defects are overcome by chemically crosslinked systems. Dextran hydrogels were crosslinked using urethane bond and ester-containing diglycolic group

4. Hydrogels

were synthesized in the presence of hydrogen peroxide (H_2O_2) and horseradish peroxidase (HRP) [175]. The gelling times varied between 5 seconds to 9 minutes for different concentrations of the polymer as well as the solvents. H_2O_2 and HRP were used in another study to crosslink HA–tyramine (HA-Tyr) conjugates [176]. Human serum albumin (HSA) was crosslinked by tartaric acid derivative (TAD) and release of doxorubicin hydrochloride (DOX) was carried out [177]. The release was sustained for nearly 100 hours in vitro. Genipin has been used to crosslink systems based on chitosan, gelatin and bovine serum albumin (BSA), making it possible to alter the dissolution times from 3 to 100 days [178].

The drug itself may at times be used as a cross-linker. Primaquine, a di-amino drug, was used to cross-link periodate-oxidized gum arabic into a hydrogel by rapidly forming Schiff bases between the drug's amide groups and the polymer's aldehyde groups [179]. The polymer can also be modified in a way so as to provide polymer-polymer crosslinking. Addition of an amine or thiol group and a vinyl group, known as Michael addition, has been an interesting area for research. Gelation times of 0.5-0.7 min were achieved on crosslinking vinyl sulfone-functionalized dextrans with thiolated PEG [180]. Diacrylate PEG can be used to crosslink dithiolated PEG [181] or other thiolated polymers such as HA, chondroitin sulphate and gelatin [182]. *In vivo* release of fibroblast growth factor was prolonged using diacrylate PEG gelled with thiol-modified heparin and HA [183].

Extensive research is being carried out to exploit the effects of nanogels and NPs in one nano-structure. The physico-chemical properties of the hydrogels can be combined with the magneto-optical properties of inorganic NPs to form hybrid NPs suited towards various biomedical applications. These smart NPs are discussed in the following section.

5. Hybrid NPs

As the name suggests, hybrid NPs are an assembly of more than one distinct NPs having nanoscale dimensions. Due to characteristics like biocompatibility, surface functionalization and physiochemical properties, AuNPs have become major candidates in biomedical applications. However, they are associated with a limitation. The plasma proteins in the blood tend to adsorb on the surface of these NPs thereby producing large aggregates [184]. This results in altered pharmacokinetics and biodistribution of AuNPs. To deal with this, PEG was coated on AuNPs. It was seen that PEG reduces the adsorption of proteins and minimizes uptake by the liver [185].

As already discussed, distinct nanomaterials having diagnostic and therapeutic functions can be incorporated in a single entity for the use of theranostics applications. In one such attempt to synthesize smart NPs, a core-shell hybrid nanogel system was designed (Figure 29). The nanogel comprised an Ag-Au bimetallic core. The core provided fluorescence, cellular imaging as well as photothermal effect by absorbing near infrared (NIR) light. The core was coated with a thermos-responsive polymer, PEG. In addition to this, a targeting ligand was attached. HA targets a cluster determinant 44(CD44), overexpressed in numerous tumors. Finally, an anticancer drug, temozolomide was loaded in the nanogel. Loading, as high as 46% was achieved with the hybrid NP [186].
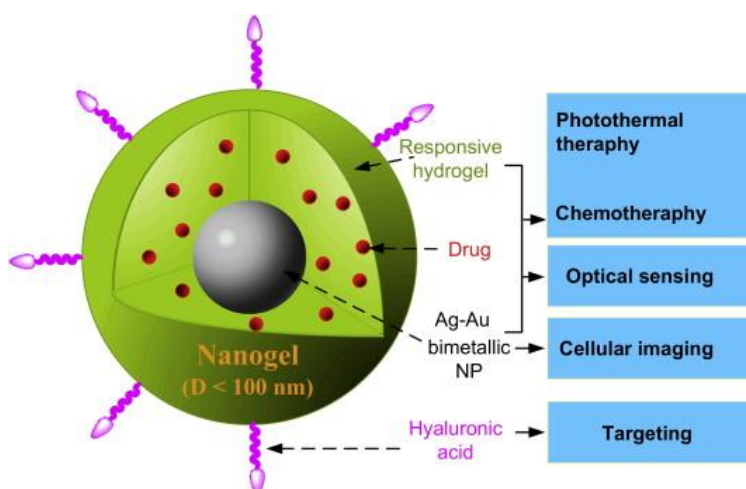
Figure 29 Schematic of the hybrid NP [186].

5. Hybrid NPs

Polypyrrole (PPy) coated Urchin shaped AuNPs have been shown to have enhanced structural stability towards storage, heat, light, pH and laser irradiation. PPy coated AuNPs also exhibited higher photothermal conversion efficiency (η) of 24% as compared to bare AuNPs ($\eta = 11\%$) [187]. Figure 30 depicts PPy coated AuNPs. The coating is evident by the shift in the Au spectra before and after coating.
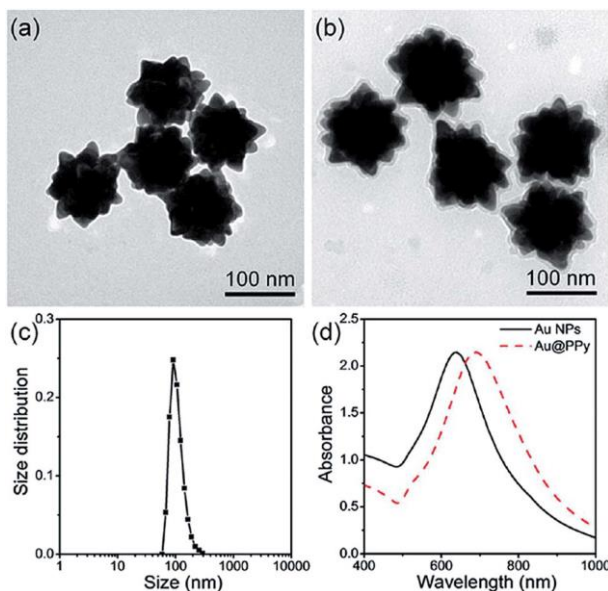
Figure 30 PPy coated urchin AuNPs [187].

In a drug targeting study, Au-Fe hybrid NPs (HNPs) were functionalized by a single chain antibody, scFv, which binds to A33 antigen overexpressed in colorectal cancer cells. The rate of uptake of scFv functionalized HNPs in cancer cells was five time higher than in cells not overexpressing A33. Up on six minutes of laser treatment revealed 53% cancer cells dead and <5% non-cancer cells dead [188].

6. Materials and Method

Poly-ethylene glycol (PEG), N-isopropylacrylamide (NIPAM), N-N'-Methylene-bisacrylamide (BIS), acrylic acid (AAc), potassium persulfate (KPS), didecyldimethylammonium bromide (DDAB), Oleic acid (OA), Gold(III) chloride hydrate (HAuCl₄), sodium borohydride (NaBH₄), silver nitrate (AgNO₃), ascorbic Acid (AsA), and Cytochrome-C (Cyt-C) samples were purchased from Sigma-Aldrich®. Hexadecyltrimethylammonium bromide (CTAB) and sodium citrate were obtained from Acros Organics® and Merck® respectively. Milli-Q (MQ) water (18.2MΩ/cm at 25°C) was taken from MilliQ® Reference Water Purification System installed in the Ugelstad laboratory.

6.1 Synthesis of hydrogel and Fe@Au incorporated hydrogels

Precipitation polymerization is used for synthesizing the hydrogel. It starts as a homogeneous polymerization process but shifts to a heterogeneous process. The polymerization is carried out at high temperatures. The polymer chain grows by free radical chain propagation after the polymer is attacked by the initiator radical. As the temperature is much above the LCST of the polymer, the chain collapses upon itself on reaching a critical length. These collapsed chains act as precursor particles which grow as a result of aggregation, or being captured by existing particles or oligoradicals, and by monomer addition. The nanogel is stabilized by the charge imparted by the initiator [189].

In a typical synthesis, 181 mg (1.6 mmol) of pNIPAM was added along with 14.8 mg (0.07 mmol) of BIS in a round bottom flask, maintained at 70°C. The monomer, co-monomer and cross-linker molar ratio is 1.6: 0.1: 0.2. Thereafter, 10ml of 4.2 mM of SDS was added to the mixture. The solution was degassed under nitrogen atmosphere for one hour following which, 126 µl of 1.46 M AAc was added. 400 µl of 103.6 mM KPS initiator was finally added to initiate the precipitation polymerization reaction. The reaction was allowed to continue at 70°C under nitrogen atmosphere for further 2 hours. A typical reaction scheme is shown in Figure 31 and a set up assembly is shown in Figure 32.

6. Materials and Method
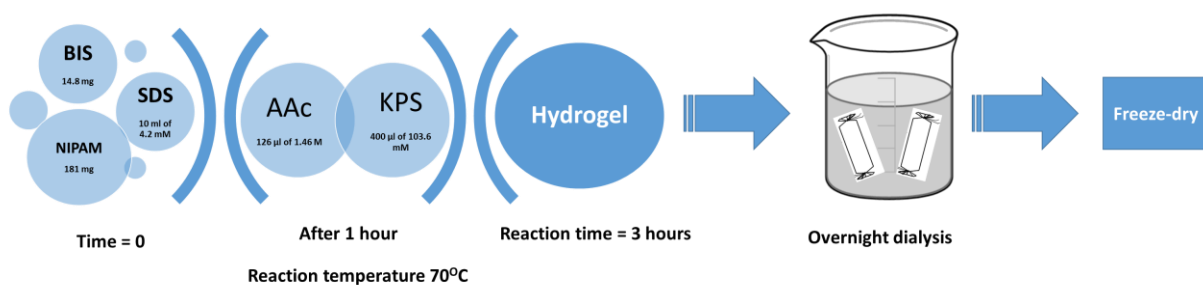
Figure 31 Schematic showing the sequences involved in hydrogel synthesis.
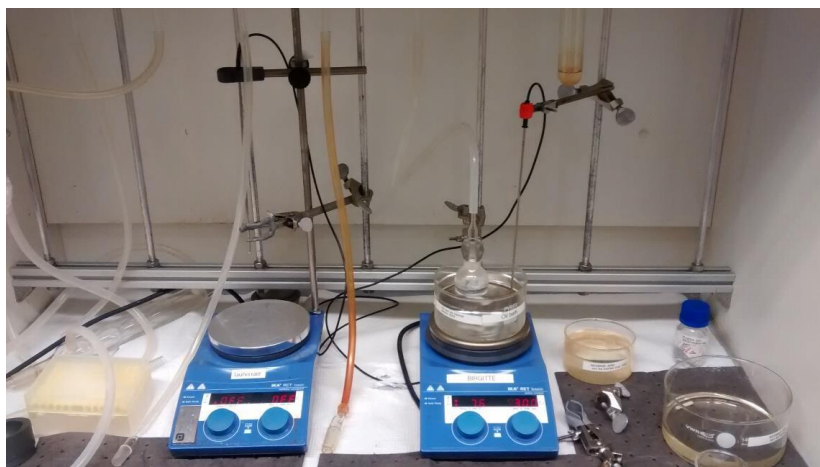
Figure 32 Schlenk line assembly for hydrogel synthesis.

The hydrogel sample was dialyzed in MQ water, overnight, followed by freeze-drying by cryodesiccation before starting the measurements.

Fe@Au_insitu NPs were synthesized in the following manner. NIPAM (0.7 mmol) and BIS (40.2 μmol) were introduced directly into the reactor under nitrogen conditions. The molar composition of pNIPAM, AAc and BIS was 8.5: 1: 0.5. Subsequently, 1mg of PEG coated Fe@Au NPs and 5mL of 4mM SDS-solution were added and the solution left to stir under nitrogen flow for 30 minutes. AAc (54 μL of 1.39 M) is added to the solution prior to the addition of KPS (200 μL of 210.7 mM). The reaction was allowed to run for 3 hours. The NG solution was poured into a pre-

washed dialysis tube (MWCO 14kDa) and dialyzed overnight to remove unreacted monomers and residual reactants.

6.2 AuNPs Synthesis

For this study, 5 different shapes of AuNPs were used namely; spherical (AuNS), nanorods (AuNR), tetrahexahedral (AuHex), bipyramids (AuBP) and nanomakura (AuNM). AuNS were synthesized using Turkevich method. For the other shapes, seed mediated growth was preferred. Their synthesis protocols are discussed in the following sub-sections.

6.2.1 Spherical AuNPs

A modified Turkevich method was used for AuNS synthesis. 10 ml of 1.74 µM $HAuCl_4$ was added to 10 ml of 10mM sodium citrate in a round bottom flask. The reaction was maintained at a temperature of 75^OC and was allowed to continue for 20 minutes. The solution was then cooled to room temperature and centrifuged for 20 min @14500 rpm using Eppendorf mini-spin centrifuge as shown in Figure 34. The supernatant was removed and the particles were re-dispersed in 5 ml water. Characterization studies were conducted using DLS, Uv-vis and S(T)EM.
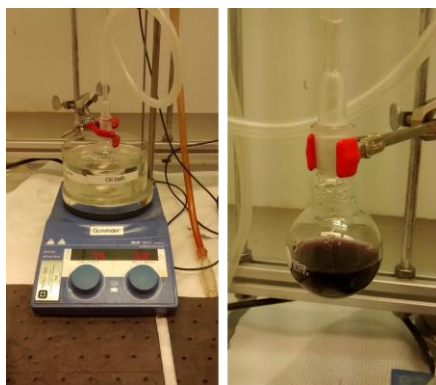
Figure 33 Apparatus set up for the synthesis of AuNS.

Figure 34 Centrifuge used for AuNS.

6.2.2 Au Seed Synthesis

5 ml of 0.5 mM $HAuCl_4$ was added to 5 ml of 0.2 M CTAB and the solution was kept under stirring for 7 minutes in a round bottom flask. 1.6 ml of freshly prepared 3.75 mM $NaBH_4$ solution was added to the reacting mixture in the round bottom flask. the stirring was stopped after 2 minutes and the reaction was allowed to continue for 30 minutes.

Figure 35 Apparatus set up for AuNP seeds.

6. Materials and Method

6.2.3 Anisotropic AuNP Synthesis

Seed mediated growth was used for anisotropic AuNP synthesis. To start with, 1.2 gm (3.3 mmol) of CTAB was dissolved in 15 ml water along with OA or DDAB as shown in Table 2, and the solution is maintained at $110^{O}C$ with constant stirring at 500 rpm. When the entire CTAB dissolved, the solution was allowed to cool down to $35^{O}C$. This was followed by the addition of 750 µl of 4mM $AgNO_3$. After 15 min, 15 ml of 1mM $HAuCl_4$ is added. The stirring speed was increased to 1000 rpm after 15 minutes. AsA was added followed by the seed solution and stirring was stopped. The reaction was allowed to be carried out overnight.

Table 2 Ingredients for the synthesis of anisotropic NPs.

	AuNR	AuHex	AuBP	A*	AuNM
CTAB (gm)	1.2	1.2	1.2	1.2	1.2
OA (µl)	20	300	0	30	30
DDAB (mg)	0	0	200	0	0
4mM of AgNO₃ (µl)	750	750	750	750	750
1mM of HAuCl₄ (ml)	15	15	15	15	15
128mM of AsA (µl)	135	135	135	135	135
Seed solution	96 µl	96 µl	96 µl	96 µl	300 µl of A*
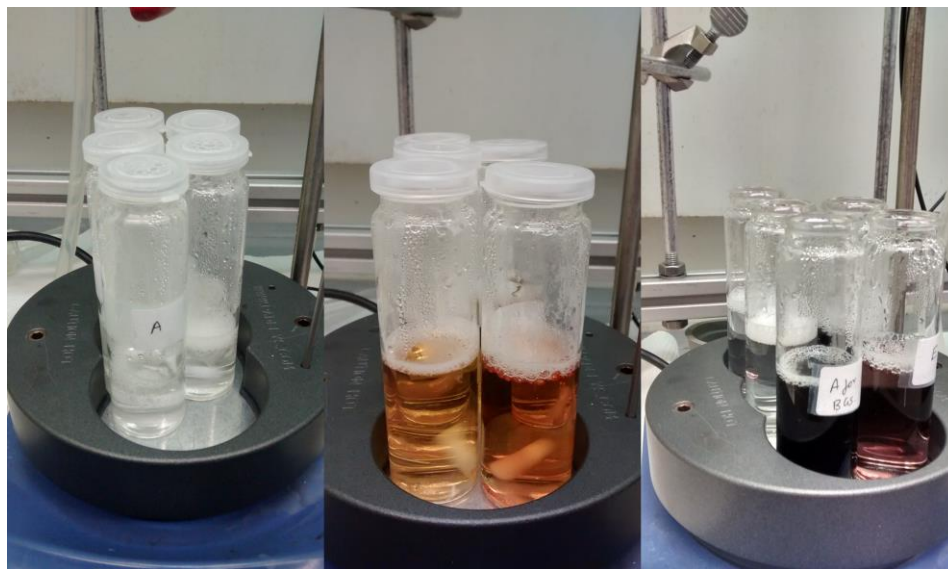
Figure 36 Anisotropic NPs' synthesis in progress.

The final coloured solutions were then centrifuged for 20 minutes @11000 rpm using the Eppendorf centrifuge 5810 as shown in Figure 37. The NPs were then re-dispersed in 5 ml water. Characterization studies were conducted using DLS, Uv-vis and S(T)EM.

Figure 37 Centrifuge @ NTNU PFI Lab, used for anisotropic NPs.

6. Materials and Method
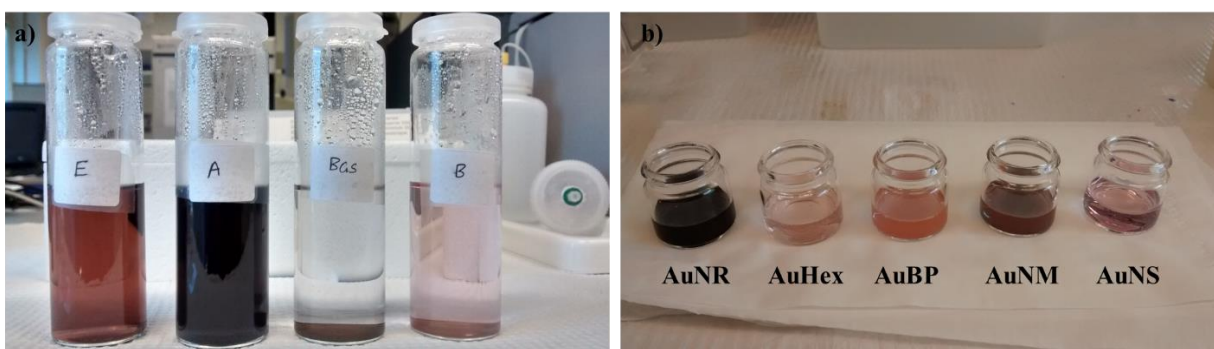
Figure 38a) Anisotropic NPs showing colour variation. b) From left: Nanorods, Tetrahexahedral, Bipyramids, Nanomakura, Spherical.

6.2.4 PEG Coating

By coating with PEG, the positively charged CTAB layer was replaced by the negatively charged PEG. The efficacy of replacement of CTAB by PEG was studied by selecting 3 different concentrations of PEG (0.5 mg/ml, 1 mg/ml, 2 mg/ml). Three samples of 400 µl NPs solution were taken and additional 600µl water was added to each of the samples. 1 ml of three different concentrations of PEG (0.5 mg/ml, 1 mg/ml, 2 mg/ml) was added separately to the 1 ml NPs solutions and the mixtures were placed under stirring @500 rpm for 2 hours. The reaction was stopped after two hours and the solutions were centrifuged @14000 rpm for 20 minutes. The PEG-coated NPs were re-dispersed in 3 ml of water. Characterization studies were performed on the samples using DLS and Uv-vis.

6.2.5 Hydrogel Coating

In order to remove the CTAB layer further, a layer of hydrogel was coated. An effect, similar to the PEG coating was studied using three different hydrogel weights (1.67 mg, 3.3 mg, 6.6 mg) and its effect on the zeta potential of the AuNPs was observed. Three different weights (1.67 mg, 3.3 mg, 6.6 mg) of hydrogel were measured. 3 ml solutions of NPs coated with 0.5 mg/ml PEG were added to the different weighted hydrogels and the system was put under stirring @500 rpm, for 2 hours. The mixture was removed after 2 hours and centrifuged @14000 rpm for 20 min. The

hydrogel-PEG coated NPs were re-dispersed in 3 ml water. Characterization studies were performed afterwards on these samples using DLS and Uv-vis and S(T)EM.

6.3 Characterization Techniques

6.3.1 Dynamic Light Scattering (DLS)

DLS works on the principle of measuring the rate of particle diffusion via Brownian motion by analysing the rate of fluctuation in the intensity of scattered light. It measures the hydrodynamic radius of the particle by calculating the translational diffusion coefficient. It uses the principle of Rayleigh scattering in which the intensity of light is proportional to sixth power of diameter (d^6). The hydrodynamic diameter is calculated using the diffusion coefficient by the Stokes-Einstein equation [190].

$$d(H) = \frac{k_B T}{3\pi\eta D}$$

Where, d(H) = hydrodynamic radius of the particle,

k_B = Boltzmann's constant,

T = absolute temperature,

η = viscosity,

D = translational diffusion coefficient
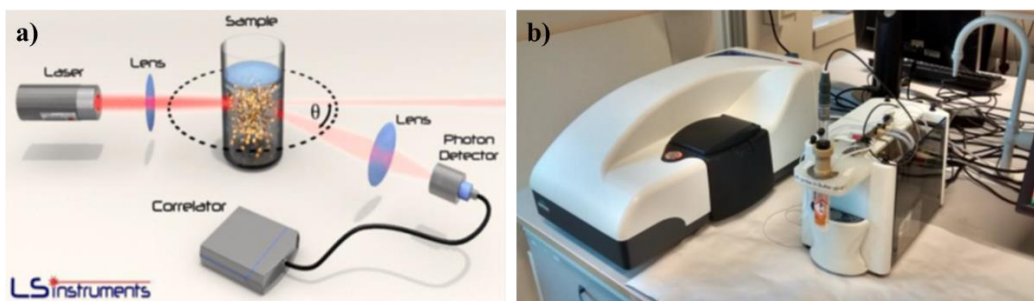
Figure 39 a) DLS working principle[191]. b) Zetasizer in Ugelstad Lab @ NTNU

6. Materials and Method

DLS measures the Z-average particle size. It analyses data based on the technique of cumulants which uses the distribution correlation function [192]. The z-average is a function of the intensity of scattered light (S_i) and the particle diameters (D_i) as a harmonic based mean.

$$D_z = \frac{\sum S_i}{\sum \left(\frac{S_i}{D_i}\right)}$$

For extremely small particles, known as Rayleigh scatterers, $S_i \approx D_i^6$. Therefore,

$$D_z = \frac{\sum D_i^6}{\sum (D_i^5)}$$

Malvern Zetasizer Nano ZS$^©$ (shown in Figure 39 (b)) was used to measure the particle size and zeta potential at different conditions. The variation of these properties was studied by changing the temperature and pH of the system. For the hydrogel, the temperature was varied from 25^OC to 60^OC and its effect on sample size as well as zeta was observed. While for the AuNPs, the size and zeta values were noted at temperatures 25^OC and 45^OC. The influence of change in pH was measured by varying the solution pH from 3 to 9 at a constant temperature of 25^OC. A simultaneous effect of both the parameters was studied at temperatures 25^OC and 45^OC, and pH 3 and 9 respectively.

6.3.2 UV-Vis Spectroscopy (Uv-vis)

Beer Lambert's law guides the underlying principle of Uv-vis. A change in the intensity of transmitted light is observed when the incident light passes through a solution due to absorption and scattering. The 10th log of the intensity change or absorbance is directly related to the concentration of the solution as well as the path length.

$$log_{10}\frac{I_o}{I} = A = \epsilon lc$$

Where, I_o = intensity of incident light

I = intensity of transmitted light,

A = absorbance,

ε = extinction coefficient,

l = path length,

c = solution concentration
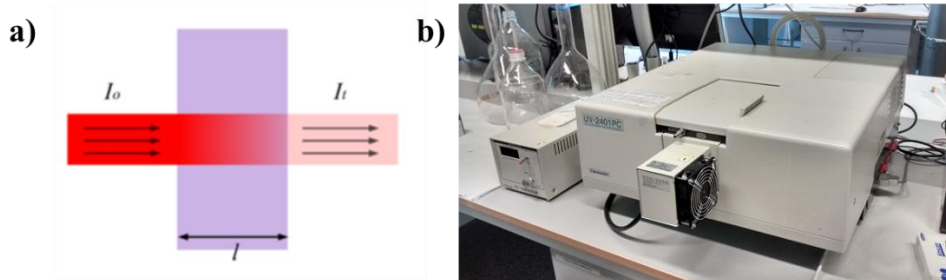
Figure 40 a) Transmittance through a sample[193]. b) Uv-vis instrument in Ugelstad lab @ NTNU.

Uv-vis was also used for the characterization of the samples. Analysis of the loading and release studies were carried out using Shimadu$^©$ Uv-vis recording spectrophotometer (Figure 40 (b)), model no. UV-2401PC. All the spectra were recorded at temperatures of 25^OC. The primary aim of performing Uv-vis was to understand LSPR characteristics before and after coating of AuNPs. For the loading and release studies, the Cyt-C absorbance peak at a wavelength of 409 nm was observed with time.

6.3.3 Scanning (Transmission) Electron Microscopy S(T)EM

It is a microscopy technique which passes a beam of electrons through a thin sample and focuses the beam over a narrow region which is scanned over the specimen in a raster. A magnified image

can be obtained by selecting from a variety of scattered signals. The S(T)EM can be operated in various modes as listed below [194].

i)   Bright field (BF): This mode is based on the transmitted electrons which leave the specimen at relatively lower angles with respect to the optical axis.

ii)   Annular dark field (ADF): It is based on the transmitted electrons with greater angles with respect to the optical axis.

iii)   Electron energy loss spectroscopy (EELS): A spectrum of transmitted electrons, that have lost quite a measurable amount of energy, as a function of energy loss can be formed.

iv)   Energy-dispersive X-ray spectroscopy (EDX): It relies on the x-ray generated from the electron excitations in the specimen.
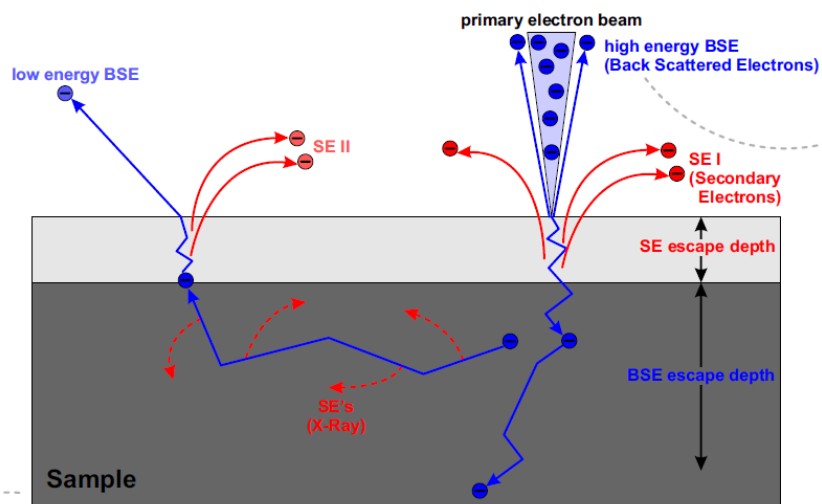
Figure 41 Schematic depicting different scattering electrons off a sample.

The electrons are scattered both, elastically and inelastically. The elastic scattering is caused due to electrostatic repulsion from the atomic nuclei, while the inelastic one is caused due to interaction from the atomic electrons. Mostly the inelastic scattering, also known as emission of secondary electrons, dominates. It has a scattering angle of less than 90°. The elastic scattering or the emission of backscattered electrons is greater than 90° [195]. Figure 41 shows the different scattered electrons off a specimen during S(T)EM imaging.

6. Materials and Method

S(T)EM was used to determine the shape and size of the different AuNPs. Another characterization was performed after PEG-hydrogel coating to observe the AuNP-hydrogel interactions.

6.3.4 VPTT Calculations

An approach to calculate the LCST was formulated based on the swelling collapse behavior of the hydrogels. Variation in any spectroscopy parameter, here optical density, was measured against temperature [196]. The system comprised of N-isopropylacrylamide (NIPAM) with acrylic acid (AAc) as the co-monomer. As a real hydrogel system is not completely monodispersed, differently sized particle will collapse at a unique LCST. This results in a range of temperature along the collapsing or swelling curve, thus making it difficult to comment on a single temperature defining the LCST of the entire system. Hence, LCST of the system could be defined as the temperature at which the ratio of the collapsed and swelled hydrogels is equal as shown in Figure 42.
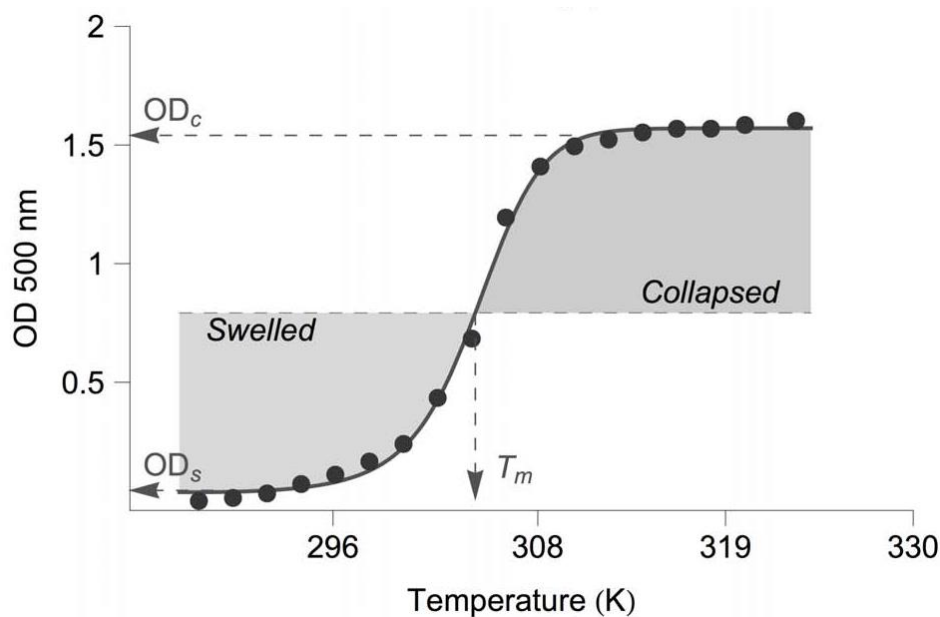
Figure 42 Variation of optical density with temperature for the determination of LCST [196].

The method devised to calculate the VPTT is based on the swelling collapse behaviour of the hydrogel (139). The variation of particle size is measured as a function of change in any

6. Materials and Method

spectroscopic parameter (here, temperature). The parameter 'α' is then plotted against the spectroscopic parameter. α is defined as,

$$\alpha = \left(\frac{D}{D_o}\right)^3$$

Where,

D = diameter at the measured temperature

D_o = diameter at room temperature

Any hydrogel system is not completely monodispersed. Hence, particles of different sizes show phase transitions at different temperatures. Further, the polymers possess different chain lengths owing to different degrees of polymerization. Thus, we get a range of temperatures instead of a single value. As temperature is varied, the hydrogel is present in a partially collapsed state.

This concept is used to determine the ratio of the swelled and the collapsed states at any particular instance. Therefore, at VPTT, the fraction of collapsed states should be equal to the fraction of swelled states. To start with, the spectroscopic parameter is plotted against temperature using SigmaPlot®. A Gaussian 5 parameter curve is fitted to the data. By using the parameters obtained from the curve, a MATLAB® code generates another curve between 25^OC and 55^OC as shown by Figure 43.
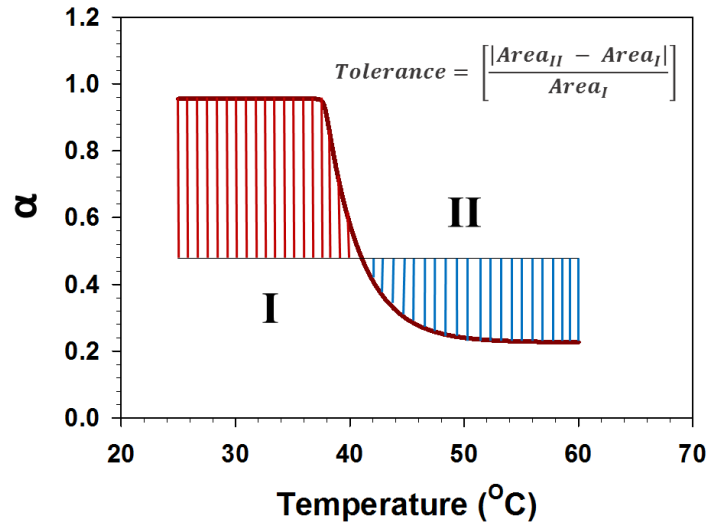
Figure 43 Schematic depicting area equalization for VPTT calculations.

Gaussian 5 parameter curve equation:

$$y = y_o + \frac{a}{\left(1 + e^{-\left[\frac{x - x_0}{b}\right]}\right)^c}$$

The code divides the curve into two parts and calculates the area under the curve using Simpson's 1/3rd rule. A mean temperature is taken to start the calculation. A tolerance value is set defining required preciseness of VPTT. The number of iterations define the amount of divisions the code makes on the curve. If the relative difference of the areas of the collapsed and swelled states do not fall under the mentioned tolerance, the code refigures the iterations until the value of relative area difference is below it. The point of division of the curves of the swelled and collapsed states adjusts itself so as to minimize the tolerance value.

$$\int_a^b f(x)dx \approx \frac{h}{3}\left[f(x_o) + 2\sum_{i=1}^{\frac{n}{2}-1} f(x_{2i}) + 4\sum_{i=1}^{\frac{n}{2}} f(x_{2i-1}) + f(x_n)\right]$$

$$Tolerance = \left[\frac{|Area_c - Area_s|}{Area_s}\right]$$

Where,
Area$_c$ = Area of collapsed states
Area$_s$ = Area of swelled states
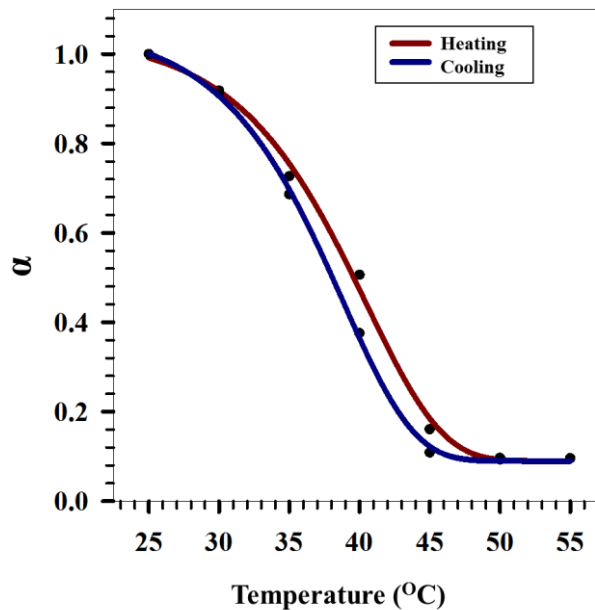
Figure 44 Heating and cooling curves for VPTT calculations for hydrogel.

The number of iterations defines the number of state points the system will go through between the highest and the lowest temperature values. The number of iterations and toleranve have been fixed at 1000 and 0.001 respectively for all calculations of VPTT.

6.4 Loading

Loading can be achieved by various ways. By using the incorporation technique, the drug is added at the time of hydrogel synthesis. Another procedure could be to add the drug post synthesis. The drug can either adsorb on the surface or get absorbed in the hydrogel matrix. Incubation of drug particles in the solution is carried out for absorption. The absorption of the drug in the hydrogel matrix is known as the breathing in technique [197] as shown in Figure 45. Dry hydrogel is placed in a hydrogel loving solvent containing dissolved drug. As the hydrogel swells up, it imbibes the

drug and loading is achieved. This technique has been successfully implemented for loading of siRNA in nanogels [198]. In this work, breathing-in method has been chosen for loading studies.
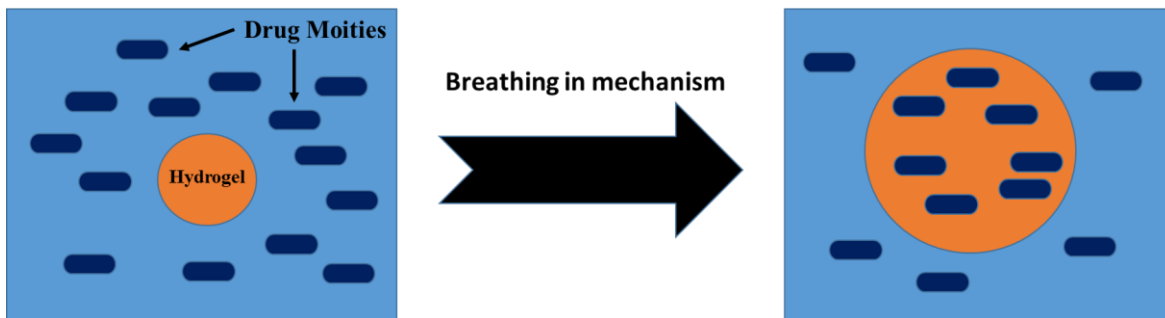
Figure 45 Schematic showing the breathing in loading technique.

6.4.1 Cytochrome C

Found loosely associated in the inner membrane of the mitochondria, Cyt C is a small hemeprotein. It has high water solubility. It has been shown to have therapeutic attributes, being used as antiobesity drug for the prevention of diet-induced obesity. Cyt C was encapsulated in prohibitin targeted NPs [199].

Figure 46 AuNPs on shaking for the loading of cytc.

For this study, 2 samples each of hydrogel-PEG coated NPs were taken in separate 1.5 ml Eppendorf tubes for centrifugation @14000 rpm for 20 minutes. The supernatant was removed and 1 ml of 0.5 mg/ml Cyt C was added to each sample. The samples were then put on shaking for 2 hours. Figure 46 shows a typical shaker used for the loading of Cyt C. The reaction was stopped and the 2 samples of each NPs were mixed together to form 2 ml loaded solution. The loaded solution was put overnight on dialysis. After the dialysis, the samples were removed and taken further for release studies.

6.5 Release

For this study, 2 ml of the loaded NP samples were taken. 2 ml water was additionally added and Uv-vis was conducted. The release was carried out over dialysis and the decrease in the absorbance peak of Cyt C with time was observed over a period of 2 days. The release was carried out at 45^OC and 3.5 pH. Figure 47 depicts a typical setup of dialysis for drug release studies.
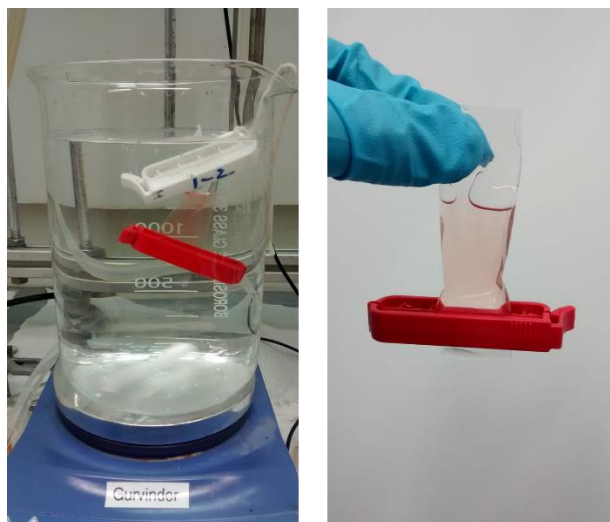
Figure 47 Samples put on dialysis for performing drug release studies.

7. Results and Discussion

The results and discussion section is further subdivided as outlined below. Firstly, characterization results of hydrogel are discussed. Different combinations of hydrogel with Fe@Au NPs are presented in this sub-section- namely coating and *in-situ* methods. Their properties and applications are further explained using drug loading and release studies. Thereafter, the physico-chemical properties of different shapes of AuNPs, synthesized using seed-mediated approach, are discussed. The changes in their properties are mapped upon PEG coating followed by hydrogel coating on these AuNPs using Dynamic Light Scattering, zeta potential measurements S(T)EM and Uv-vis. Finally, the combined effect of PEG and hydrogel coatings are analysed estimated on drug loading and release of Cyt C under the influence of elevated temperature and acidic pH.

7.1 Hydrogel

The pNIPAM-AAc hydrogels cross-linked with BIS were synthesized using precipitation polymerization as outlined in <u>section 6.1</u>. In order to check the repeatability of the synthesis process, several experiments were performed. Size, zeta potential measurements for the two hydrogels C1 and C are outlined below for sake of comparison. Hydrogels C1 and C were synthesized using the same procedure but at different time points during the study.

7.1.1 Size and Zeta Potential Measurements

Figure 48 (a) shows the hydrodynamic sizes (nm) at 25^OC and 45^OC for both the hydrogels. The size of C1 at 25^OC is 234 ± 2 nm while that of C is 219 ± 1nm. Both the hydrogels show a volumetric collapse with an increase in temperature and their sizes drop to 127 ± 1 nm and 125 ± 11 nm respectively at 45^OC. The variation in zeta potentials of the two hydrogels show the same trend (Figure 48 (b)). Zeta potentials for C1 and C varied upon increase of temperature (25^OC to 45^OC) from -15.1 ± 0.2 mV to -22.4 ± 0.3 mV and -18.0 ± 0.2 mV to -23.9 ± 0.2 mV respectively.

7. Results and Discussion
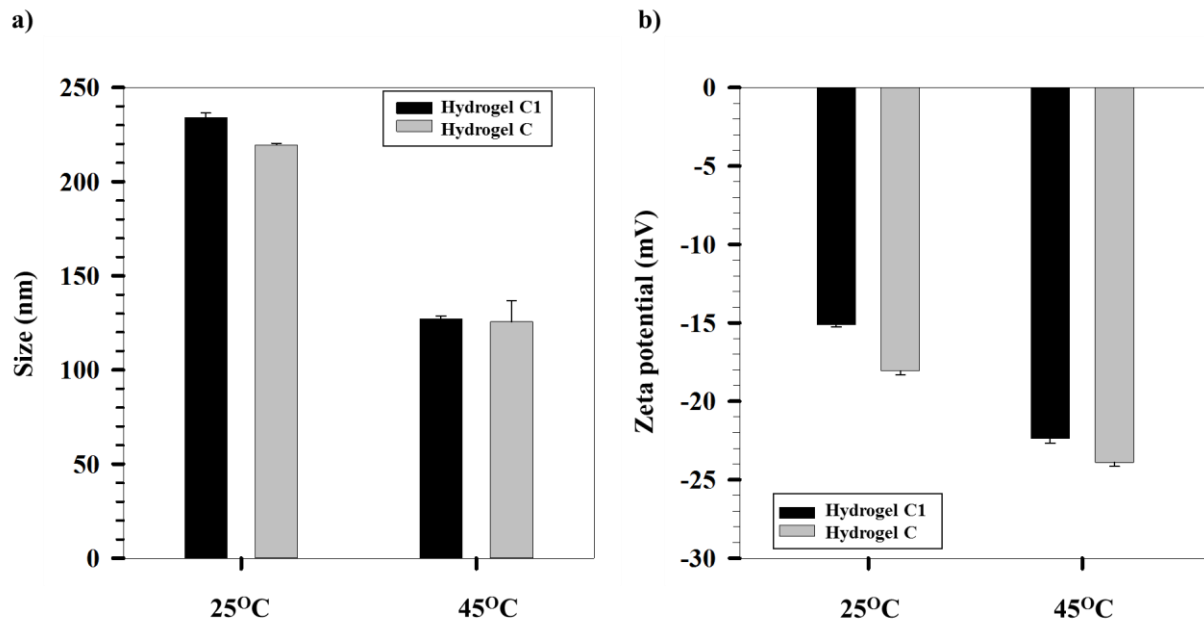
Figure 48 a) Size variation of C1 and C at 25°C and 45°C. b) Zeta potential variation of C1 and C at 25°C and 45°C.

The volumetric collapse efficiency (V.C.E.$_T$) was also calculated for the two hydrogels based on the following formula:

$$V.C.E._T = \left(\frac{\alpha_{25} - \alpha_{45}}{\alpha_{25}}\right) X\ 100\%$$

Where, α_{25} and α_{45} are the swelling ratios determined at 25°C and 45°C respectively.

C1 had a V.C.E.$_T$ of 83.9% and C had a V.C.E.$_T$ of 81.2% as shown by Figure 49. As the two hydrogels collapsed approximately by the same volume, and show similar sizes at 25°C and 45°C, the hydrogels C and C1 have been used interchangeably. This further illustrates that the synthesis method is quite robust and repeatable. In the next subsection, detailed size and zeta potential measurements of Hydrogel C1 are reported as it has been shown that C1 and C have the same physico-chemical properties.

7. Results and Discussion
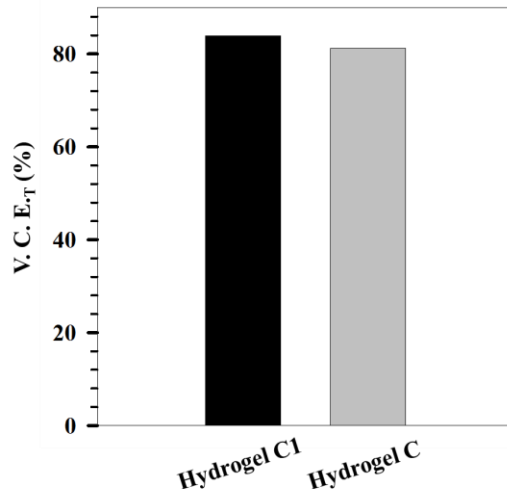
Figure 49 Volumetric collapse efficiency of C1 and C.

7.1.1.1 Temperature Dependence

The variation of hydrogel size was plotted as a function of temperature as shown in Figure 50 (a). The temperature was varied from 25^OC to 55^OC at intervals of 5^OC using DLS. C1 showed a collapse from 234 ± 2 nm to 107 ± 0 nm at 25^OC and 55^OC respectively. The VPTT of the hydrogel was calculated using an MATLAB$^®$ code mentioned in section 6.3.4 and was found to be 39.3 ± 0.6^OC.

pNIPAM bonds with water molecules through the amide side chains. The hydrophobic effect is caused by the isopropyl groups on the side chains. At elevated temperatures, entropically favoured release of bound water takes place due to breakage of hydrogel bonds. Polymer-polymer interactions grow stronger than polymer-solvent interaction and the polymer attains a globular structure resulting in phase separation. The temperature at which phase separation takes place is known as VPTT [189]. Thus, there is reduction in size beyond VPTT.

The zeta potential shows a reverse relation with the size of the hydrogel Figure 50 (b). As the size decreases, the overall surface charge density increases and thus, the zeta potential shows a negative increase with increase in temperature. The zeta potential values depict that the hydrogels are

colloidally stable, the stability being provided by the electrostatic effect. With high absolute potential at 45°C the particles do not agglomerate due to electrostatic repulsion.
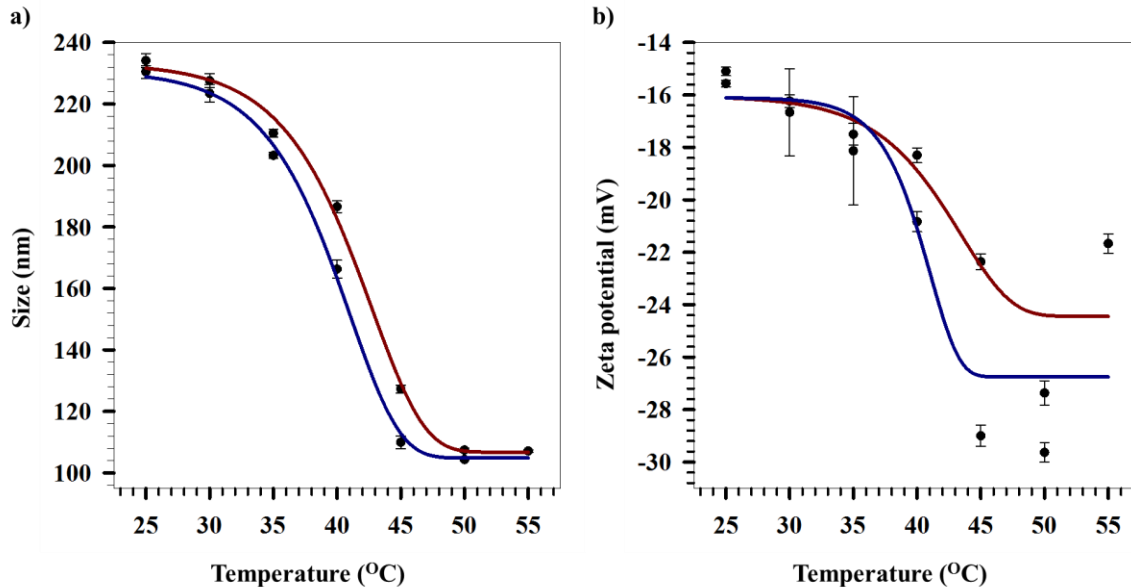
Figure 50 a) Size variation with temperature. b) zeta potential variation with temperature.

7.1.1.2 pH Dependence

Size and zeta potential dependence on pH was investigated for the hydrogel C1. Figure 51 (a) and (b) show the variation in sizes and zeta potentials respectively for three different pH conditions. The pH was varied from basic (pH 9) to acidic (pH 3), using NaOH and HCl respectively. As the pH tends towards basic, the acrylic acid groups come into play and dissociate further by releasing H^{+} ions, thereby increasing the negative zeta potential. A reverse effect is observed in acidic conditions. As HCl is a stronger acid compared to AAc, it hinders its dissociation. As a result, the zeta potential decreases. The effect of varying zeta potential can be seen on the hydrogel's size. In basic conditions, the size increases due to the electrostatic repulsion as a result of high surface charge. While at lower pH, the hydrogel shows a collapse as the surface charge density decreases and with it the electrostatic repulsion, thereby pulling the hydrogel matrix closer.
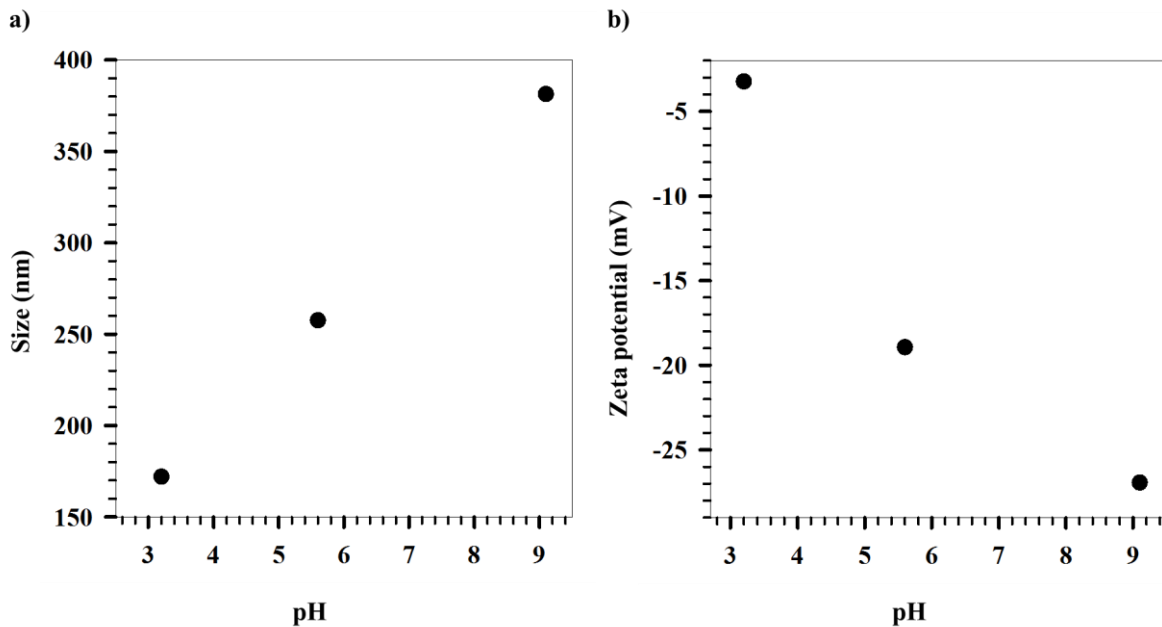
Figure 51 a) Variation of size of hydrogel C1 with pH @25°C. b) Variation of zeta potential of hydrogel C1 with pH @25°C

7.1.1.3 Combined Effect of pH and Temperature

A combined effect of pH and temperature was studied on the hydrogel size and zeta potential. Figure 52 (a) and (b) depict the variation of size and zeta potential with pH of hydrogel C1 respectively. The pH was varied from pH 9 to pH 3 while maintaining the system at a temperature of 45°C. The size decreases as a result of decrease in overall surface charge. The reduction in electrostatic repulsion allows the polymeric chains to come closer thereby reducing the overall matrix size. The zeta potential reduces on moving towards acidic medium due to the hindrance of dissociation of AAc groups by HCl as also seen in previous studies [200].

7. Results and Discussion
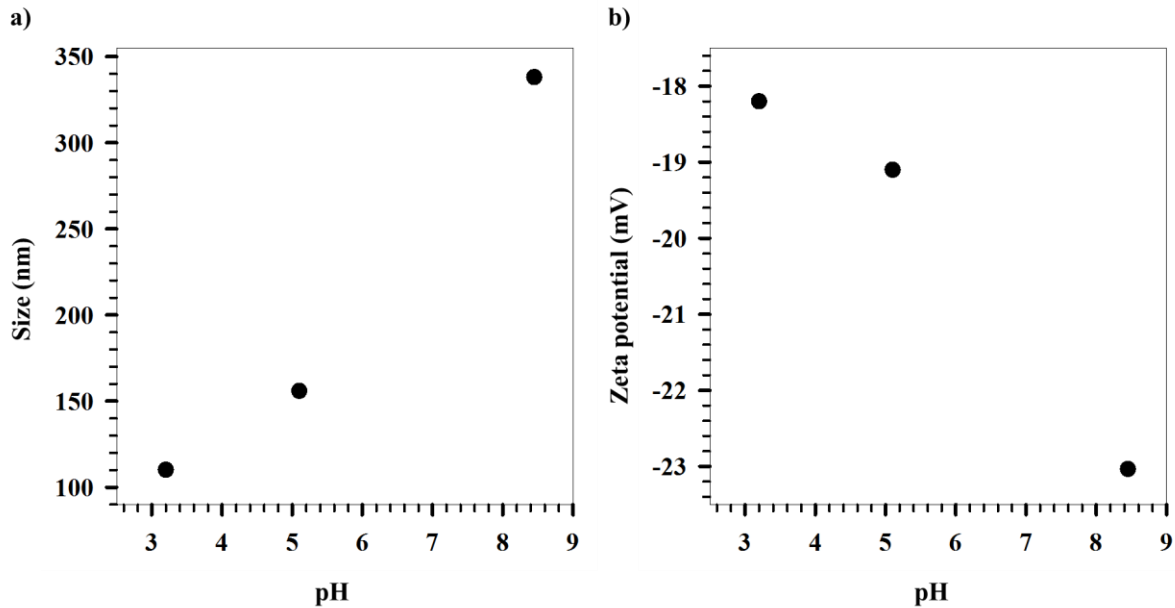
Figure 52 a) Variation of size of hydrogel C1 with pH @45°C. b) Variation of zeta potential of hydrogel C1 with pH @45°C

Figure 53 (a) shows the combined effect of temperature and pH on hydrogel C1's size. It can be seen that the maximum collapse of the hydrogel network is seen at conditions of high temperature (45°C) and low pH (pH 3). From Figure 53 (b), the maximum V.C.E. of 89.6% is achieved at conditions of 45°C and pH 3. To achieve maximum release of the drug from the hydrogel network by the squeezing out mechanism, condition of maximum collapse (45°C and pH 3) was thus selected.
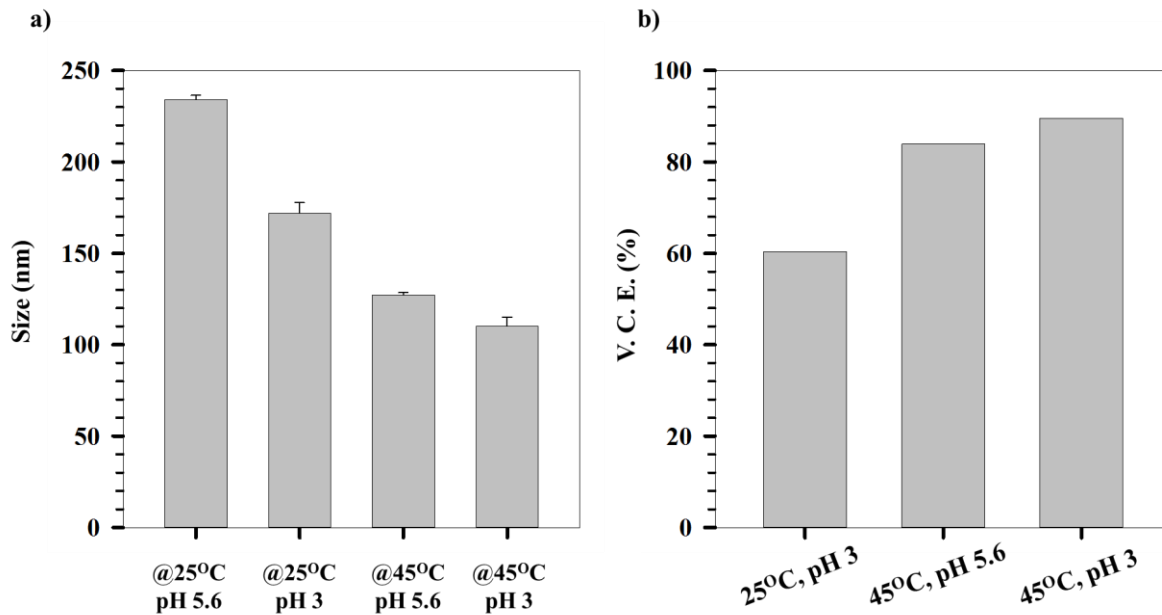
Figure 53 a) Combined effect of temperature and pH on hydrogel's size. b) V.C.E. at different conditions of temperature and pH.

Hydrogel C1 and C have shown similar swelling collapse properties in the temperature and pH range studied. They show a volumetric collapse of ~90% when subjected to elevated temperature (45°C) and acidic pH-3. Further, C1 and C have shown repeatability in regards to their synthesis. In the next section, hydrogel C has been used to coat Fe@Au NPs with an attempt to understand the combinatorial properties of the inorganic core (Fe@Au) and the hydrogel shell.

7. Results and Discussion

7.2 Fe@Au NPs Incorporated in Hydrogels

To exploit the stimuli responsive property of the hydrogel in addition to the magnetic and optical properties of Fe@Au NPs, the NPs were coated with hydrogel C. To investigate the effect of Fe@Au NP incorporation in the hydrogel network, three different systems were studied namely, hydrogel, coated Fe@Au NPs (Fe@Au_coated) and *in-situ* Fe@Au NPs (Fe@Au_insitu).

7.2.1 Coating of Fe@Au with Hydrogels

The Fe@Au were coated with PEG (0.5 mg/ml) followed by a hydrogel coating. The coating procedures were followed as per the past procedures carried out in the Ugelstad laboratory [201]. The coating can be confirmed by the increase in size of the coated NPs as shown in Figure 54 (a). Figure 54 (b) shows the variation of zeta potential of Fe@Au NPs with Peg and hydrogel coating.
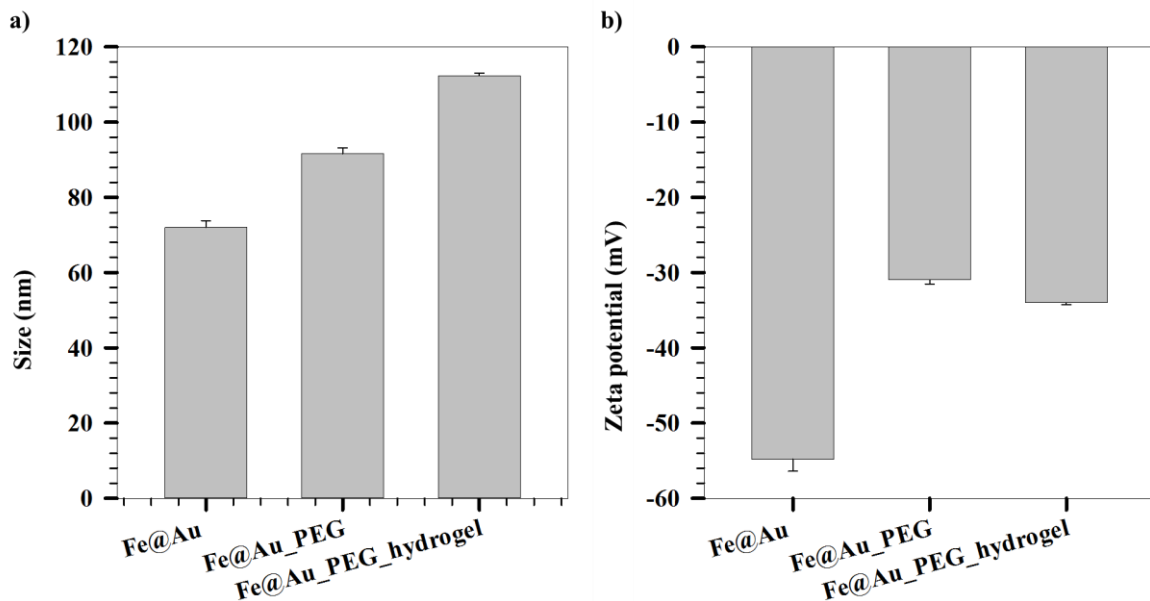
Figure 54 a) Size variation of Fe@Au NPs with PEG and hydrogel coating. b) Variation of zeta potential of Fe@Au NPs with PEG and hydrogel coating.

7. Results and Discussion

7.2.2 Comparison of Different Fe@Au Incorporated Hydrogel Systems

Fe@Au NPs were synthesized using a predefined protocol from the Ugelstad laboratory [72]. Figure 55 (a) shows the variation of size of hydrogel as well as Fe@Au incorporated systems. The bare Fe@Au NPs show an increase in size with temperature from 54 ± 1 nm to 63 ± 1 nm. The size for Fe@Au_insitu NPs varies from 336 ± 9 nm to 130 ± 1 nm at temperatures 25^OC and 45^OC respectively. The NPs in this case form the core of the hydrogel matrix with the hydrogel covering them as shown by Figure 56. As the hydrogels are exposed to the solvent particles, on reaching VPTT, they collapse owing to hydrophobic interactions maintaining minimum contact with water molecules as explained in section 7.1.1.1 (Figure 55 (a)).
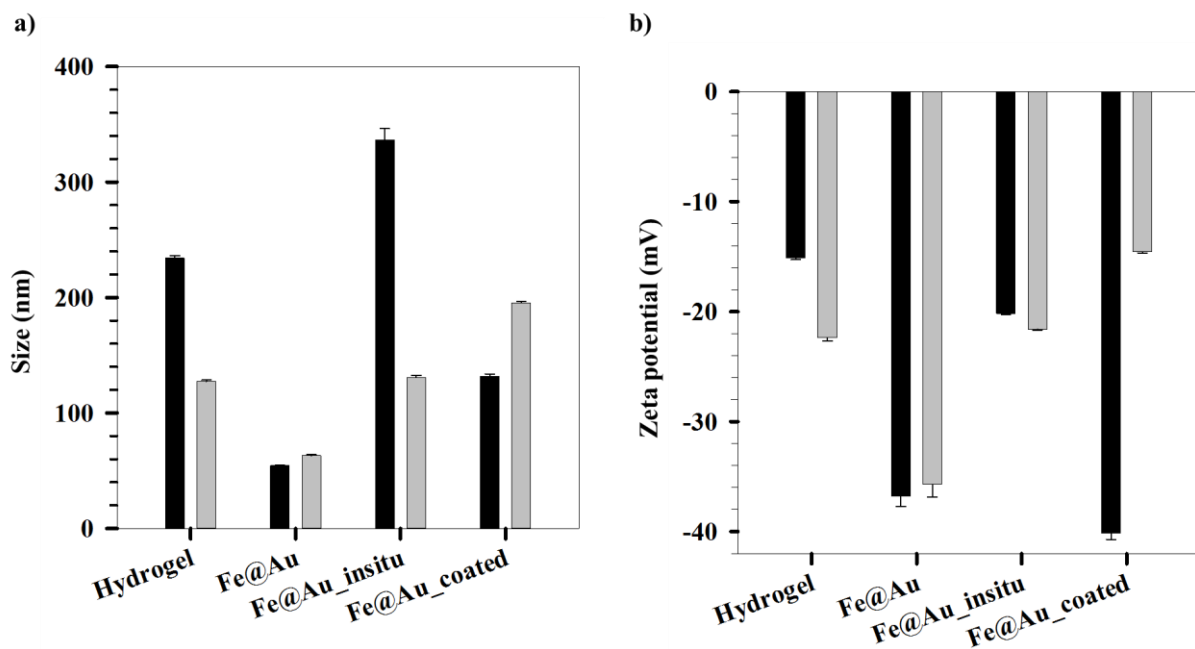
Figure 55 a) Size variation of hydrogel, Fe@Au, Fe@Au_insitu and Fe@Au_coated with temperature. b) a) Zeta potential variation of hydrogel, Fe@Au, Fe@Au_insitu and Fe@Au_coated with temperature.

At elevated temperatures, the distance between the Fe@Au increases due to thermal energy, as evident by the size increase of bare Fe@Au NPs, thereby causing an increase in the size of the hydrogel system. In the case of coating, the NPs are located at the periphery of the hydrogel network as shown in Figure 56. The NPs act as cross-linkers pulling the hydrogel network closer.

7. Results and Discussion

This is indicated by the reduced size of Fe@Au_coated (131 ± 2 nm) at 25°C compared to the bare hydrogel size (234 ± 2 nm). On increasing the temperature of the system, the
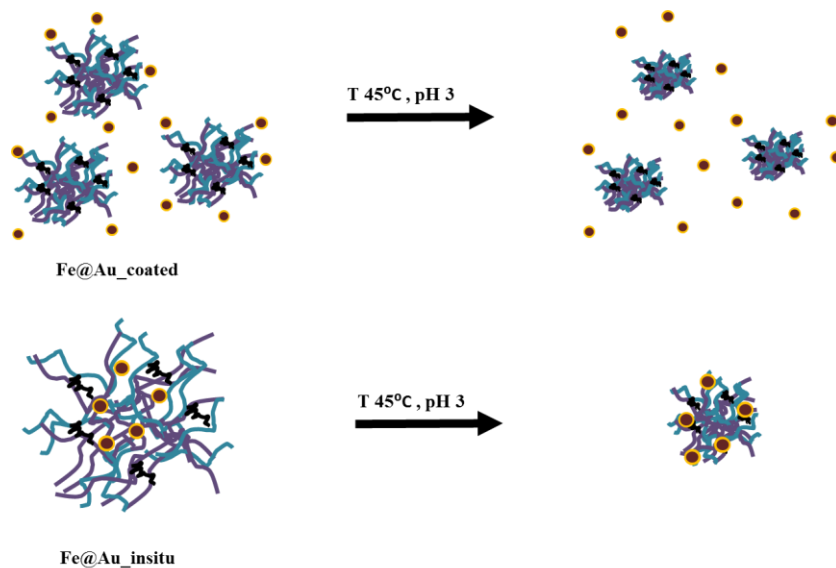
Figure 56 Schematic showing the arrangement of Fe@Au NPs in the hydrogel network and their behavior at 45°C and pH 3.

NPs pull the hydrogel network even closer to each other resulting in an overall larger network. Thus, the size of Fe@Au_coated system increases to 195 ± 1 nm at 45°C.

An evident change can be witnessed in the zeta potential of Fe@Au_coated system. This can be attributed to the fact that as size of the hydrogel network increases, the surface area increases. This results in the decrease of effective surface charge of the hydrogel system as indicted by Figure 55 (b).

It is evident from Figure 55 that the Fe@Au_coated system behaves like bare Fe@Au NPs, showing an increase in their sizes with increase in temperature. On the other hand, the Fe@Au_insitu system resembles that of the hydrogel, showing a high V.C.E. of 93.7% in comparison to the hydrogel (83.9%). The higher collapse in case of the Fe@Au_coated NPs is because of the presence of Fe@Au NPs which act as cross-linkers pulling the gelling units together. This further supports the location of Fe@Au NPs in the hydrogel matrix as depicted by

7. Results and Discussion

Figure 56 above. In order to further investigate the effect of Fe@Au incorporation in the hydrogel network, loading and release studies were conducted with Cyt C.

7.2.3 Loading with Cyt C

The three systems (hydrogel, Fe@Au_insitu and Fe@Au_coated) were loaded with Cyt C using breathing in method, wherein concentrated Cyt C solution was added to dry hydrogel based system, as explained in section 6.4. Loading (L.E.) and encapsulation (E.E.) efficiencies for the three systems were calculated (Appendix A) as shown in Figure 57. The drug solution was added to the dry hydrogel system Hydrogel had the highest L.E. of 96.4%, followed by Fe@Au_insitu, 86.3% and finally Fe@Au_coated with a L.E. of 77.9%. The decrease in the L.E. in the presence of Fe@Au NPs could be due to the fact that the NPs occupy the voids in the hydrogel matrix, thereby lowering the overall void volume of the hydrogel network. Thus, the volume for drug intake reduces as a result the L.E. decreases. The lowering in void volume is greater in the case of coating as the PEG coated NPs are likely located on the periphery of the hydrogel network and act as cross-linkers, thereby, pulling the hydrogel network in a tight arrangement [201]. This causes a reduction in the available void volume for effective loading of the drug molecules. Whereas, in case of the Fe@Au_insitu, the hydrogel network surrounds the NPs. As the NPs are present in the core of the network they do not occupy the void between the polymer chains thus providing space for drug loading. This is further supported by the low E.E of Cyt C in case of Fe@Au_coated (50.8 µg/mg of Fe@Au NPs).

7. Results and Discussion
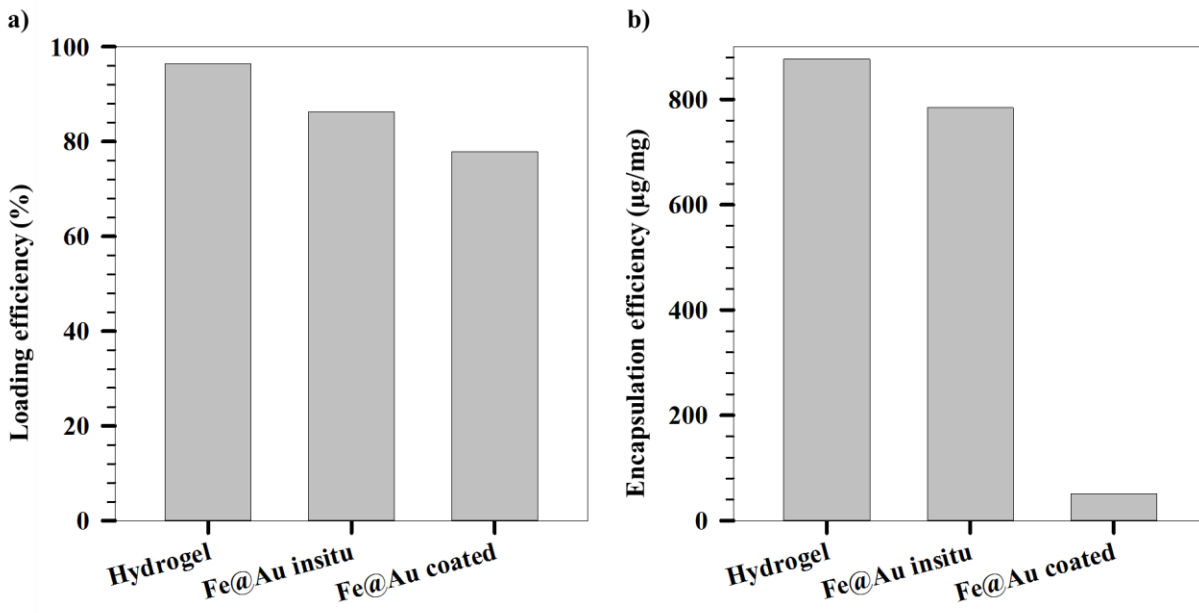
Figure 57 a) Loading efficiencies of hydrogel, Fe@Au-insitu and Fe@Au-coated. b) Encapsulation efficiencies of hydrogel, Fe@Au-insitu and Fe@Au-coated.

7.2.4 Release Study

Cyt C release was carried out at the condition of maximum collapse of the hydrogel (45^OC, pH 3) as discussed in section 6.5 . Fe@Au_coated has a maximum release of 34%, while both the hydrogel and Fe@Au-insitu had a release of around 12% as shown by Figure 58. A jump in the drug release is seen after 6 hours with the release % increasing from 12% to 27% for Fe@Au_coated.
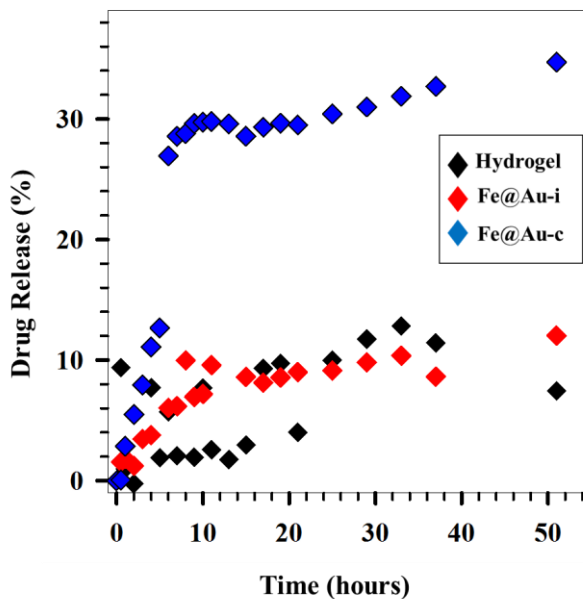
Figure 58 Drug release with time for hydrogel, Fe@Au-coated and Fe@Au-insitu.

Release kinetics

As passive diffusion is the most common mechanism of drug release from hydrogels, molecules would constantly diffuse in and out of the matrix during loading as well as storage periods. Focusing on the rate limiting step of the release phenomenon, the drug release mechanism from the hydrogel can be categorized as diffusion controlled, swelling controlled and chemically controlled [202]. Among these, the diffusion-controlled release is the most common based on Fick's first law of diffusion [203].

The matrix's mesh size primarily governs the diffusion of the drug [204]. The mesh size is dependent on various other parameters such as the degree of crosslinking, chemical structure of the composing monomers, and, the type as well as intensity of the external stimuli, if applicable. It further dictates the mechanical strength, degradability, diffusivity, and other physical properties of a hydrogel network [205]. The release is said to be swelling controlled when in the swelling-controlled mechanism, the diffusion of the drug is comparatively faster than the distention of the hydrogel [206, 207].

7. Results and Discussion

Chemical reactions occurring inside the gel matrix cause chemically-controlled release. These include polymer chain cleavages via the hydrolytic or enzymatic degradation or reversible/irreversible reactions occurring between the polymer network and the releasing drug.

Different models have been used to determine the release kinetics of various systems. Zero order kinetics is defined by the following equation:

$$F = K_o t$$

Where, F is the cumulative fraction of drug dissolved in time t with a zero order release constant K_o. it represents a direct relationship between the fraction of drug released and time. The first order release depicts a linear relation between the logarithm of the fraction of drug in the hydrogel matrix with negative of time as shown below [208].

$$\ln(1 - F) = -K_1 t$$

Where, K_1 is the first order kinetic constant. The Higuchi model describes drug release as a diffusion process based in the Fick's law, square root time dependent, shown below.

$$F = K_H \sqrt{t}$$

Where, K_H is the Higuchi dissolution constant. A general equation was proposed to define the drug transport mechanism described by Peppas' equation:

$$F = a t^n$$

Where, a is defined as a constant incorporating structural and geometric characteristics of the drug dosage form [209]. The release exponent, n, indicates the drug release mechanism as indicated by Table 3.

7. Results and Discussion

Table 3 Values of release exponent indicating different transport mechanisms.

Exponent, n			Drug release mechanism
Thin Film	Cylinder	Sphere	
0.5	0.45	0.43	Fickian diffusion
0.5< n < 1.0	0.45< n < 0.89	0.43 < n <0.85	Anomalous transport
1.0	0.89	0.85	Case-II transport

7. Results and Discussion

Zero order, first order, Higuchi and power law models were fitted to investigate the release kinetics of Cyt C from the three systems (hydrogel, Fe@Au_insitu and Fe@Au_coated). The fitted release models for hydrogel system are shown in Figure 59. Zero order model fits best to the hydrogel system with $R^2 = 0.9428$, giving a value of rate constant as $k = 0.0241$ hour^{-1}.
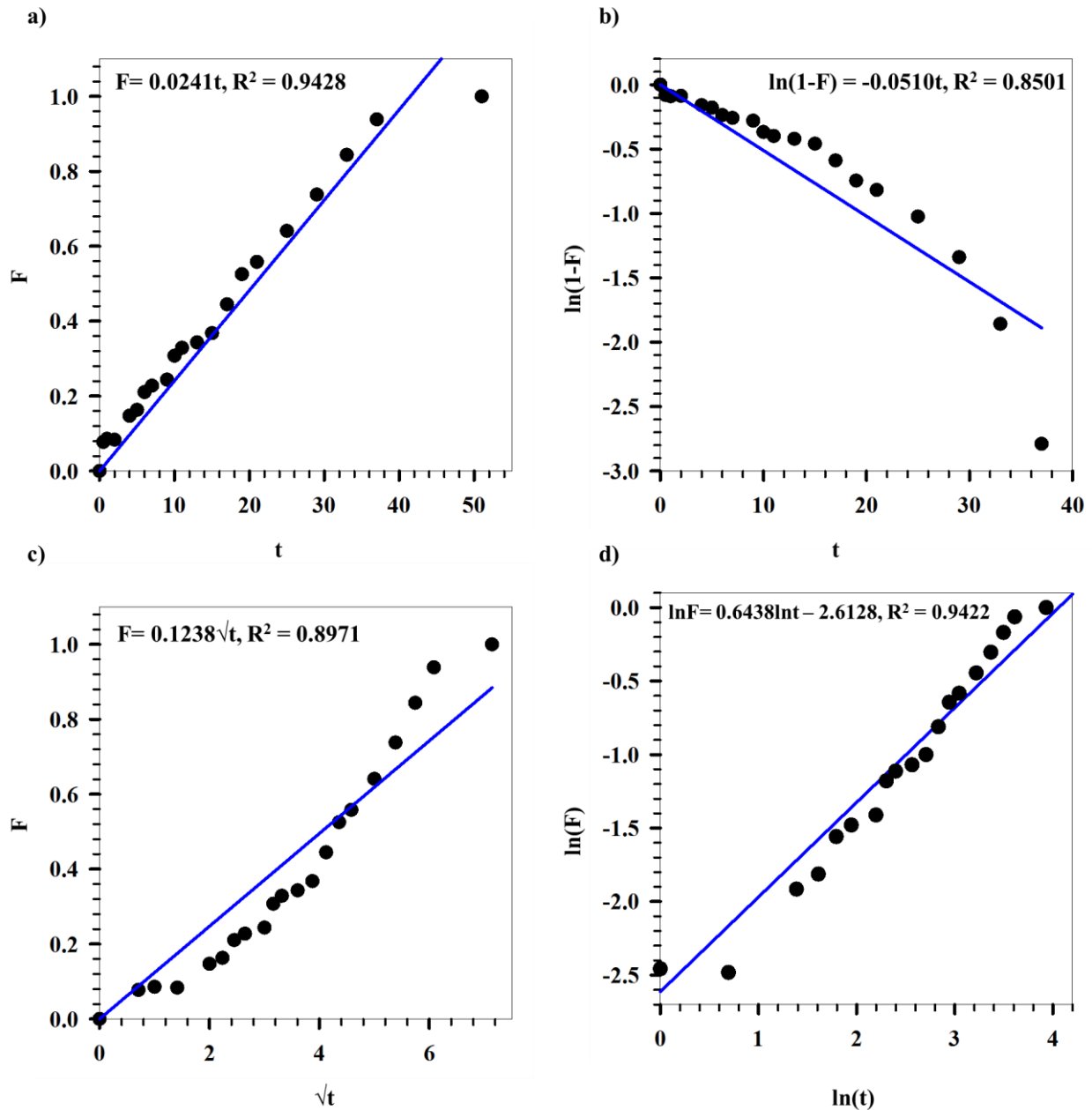
Figure 59 Release models for hydrogel system. a) Zero order model, b) first order model, c) Higuchi model, d) power law model.

7. Results and Discussion

The fitted release models for Fe@Au_insitu have been shown in Figure 60. The best fit for this system is given by the first order model with $R^2 = 0.9441$. The system has a rate constant of 0.0540 hour^{-1}.
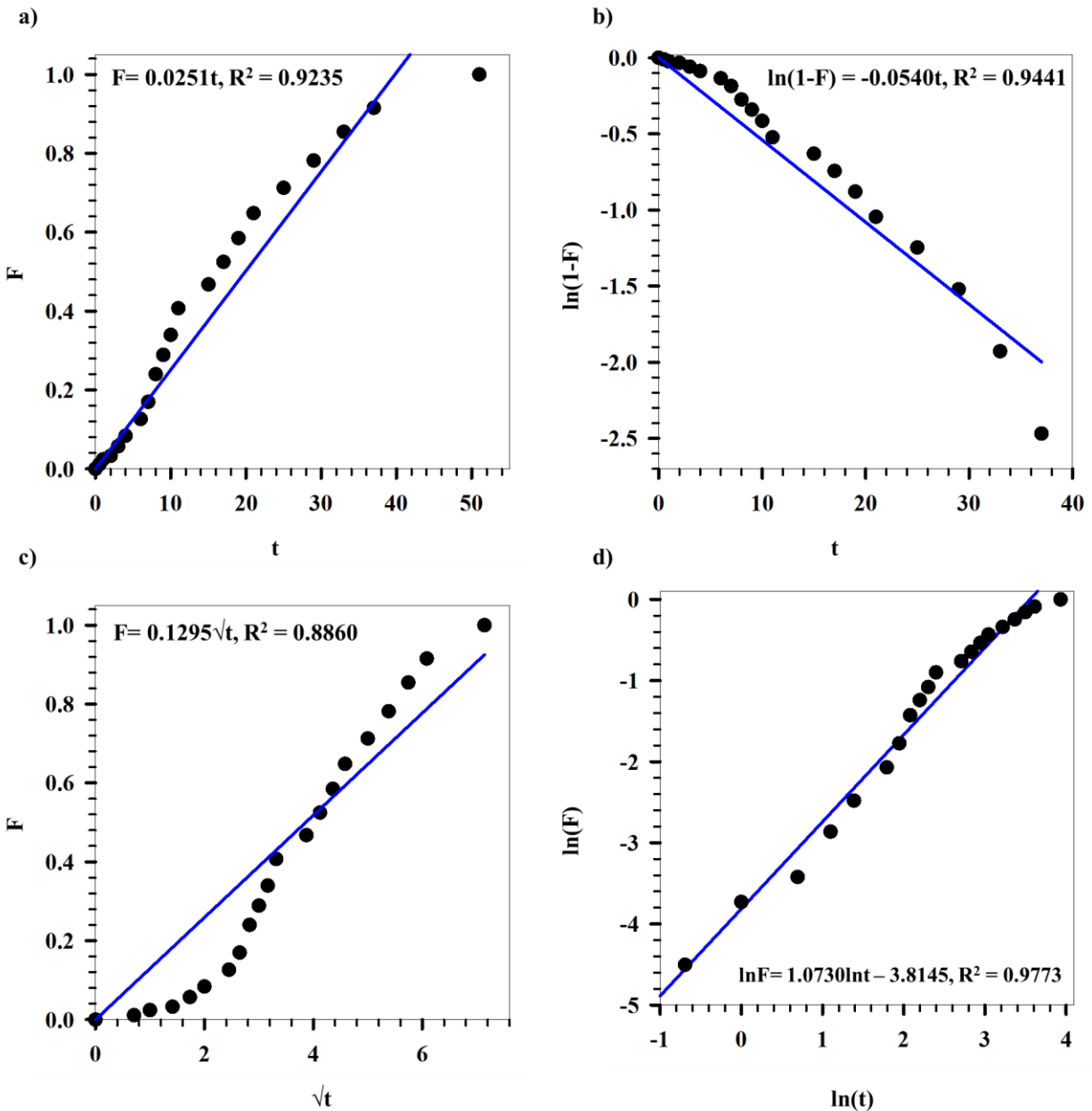
Figure 60 Release models for Fe@Au_insitu system. a) Zero order model, b) first order model, c) Higuchi model, d) power law model

7. Results and Discussion

Figure 61 shows the fitted release models for Fe@Au_coated system. This system also shows the best fit with first order kinetic model with $R^2 = 0.9410$. The value of rate constant for this system is $k = 0.0586$ hour^{-1}.
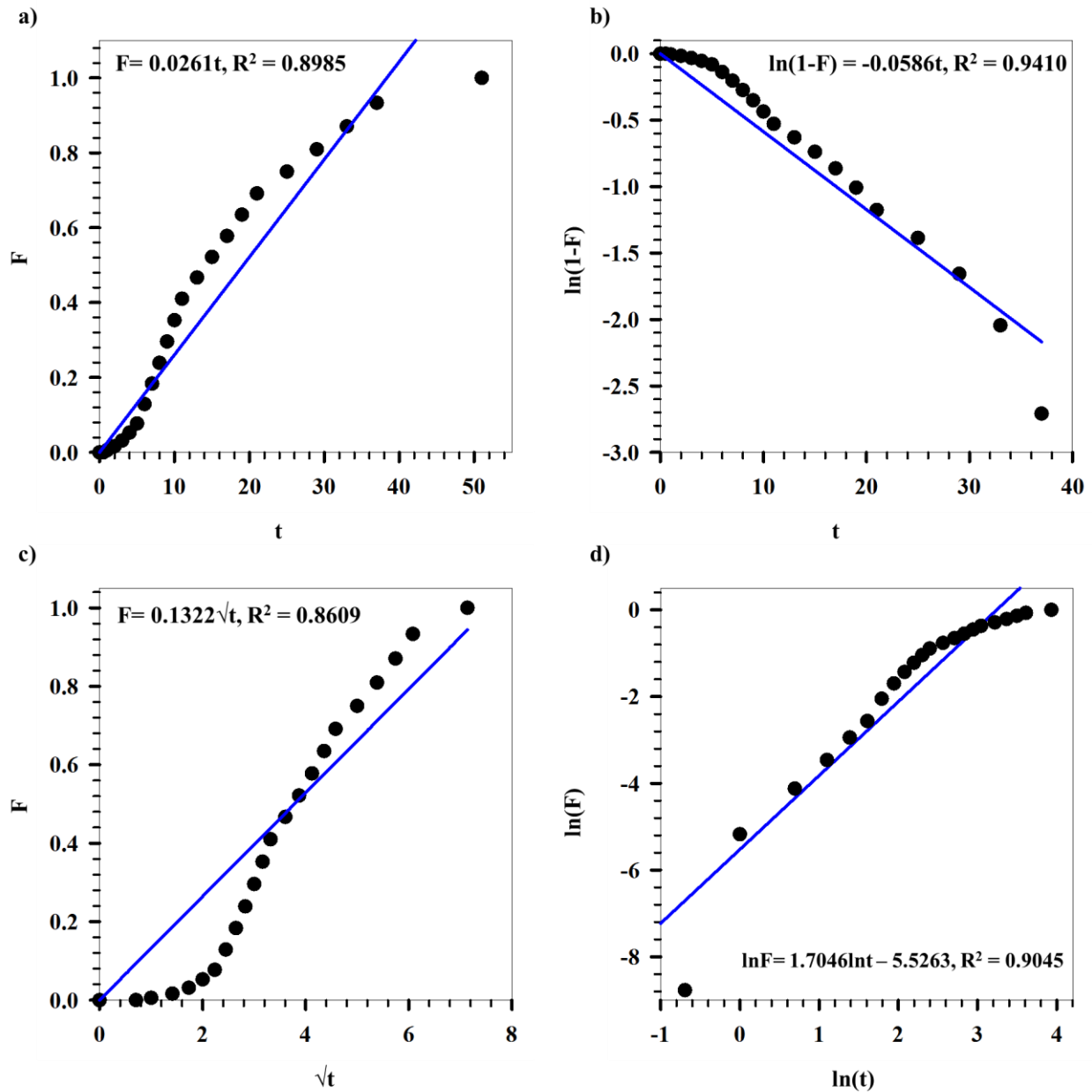
Figure 61 Release models for Fe@Au_coated system. a) Zero order model, b) first order model, c) Higuchi model, d) power law model

7. Results and Discussion

Table 4 summarises the values of release rate constants, release orders and the time for 50% drug release ($t_{1/2}$) for the different hydrogel based systems.

Table 4 Release rate constant, order and $t_{1/2}$ for the hydrogel based systems.

Sample	Rate constant, k (hour^{-1})	Release order	$t_{1/2}$ (hours)
Hydrogel	0.0241	Zero order	20.7
Fe@Au_insitu	0.0540	First order	12.8
Fe@Au_coated	0.0586	First order	11.8

The values of release exponent have been summarised in Table 5.

Table 5 Release exponent and transport mechanisms shown by hydrogel, Fe@Au_insitu and Fe@Au_coated systems.

Samples	Release exponent (n)	Geometry	Transport mechanism
Hydrogel	0.64	Cylinder or Sphere	Anomalous transport
Fe@Au_insitu	1.07	Thin film	Case-II transport
Fe@Au_coated	1.70	Thin film	Case-II transport

It can be concluded that the Fe@Au_coated system has the highest release among the three studied systems (34%). The low value of release exponent, n (0.64) and high $t_{1/2}$ (20.7 hours) for hydrogel suggests that the release is slow and the system follows either a cylindrical or a spherical geometry as shown in Table 5. 50 % of the drug is released in 12.8 hours for Fe@Au_insitu and in 11.8 hours for Fe@Au_coated systems. From Figure 58, a dip is seen in the curve for Fe@Au_coated and Fe@Au_insitu after 11 hours stating a decrease in the release of the drug. The release of the drug decreases with time as the driving force due to the decrease in concentration gradient of the drug inside and outside of the hydrogel network. Slower release of the drug from the hydrogel

network is attributed to the cylindrical or spherical geometry as the drug has to first diffuse from the hydrogel matrix to the hydrogel-solvent interface and second, diffusion through the interface to the solvent. However, for the Fe@Au incorporated hydrogel NPs, thin film geometry suggests fast drug release as the drug has to diffuse only through the film.

The effect of PEG-hydrogel coating on different shaped AuNPs has been further analysed in the following sections. Different shapes of AuNPs exhibit different LSPR peaks and the shift in the peaks for these NPs after coating with hydrogels has been observed using Uv-vis. Changes in the LSPR properties of these NPs, achieved with hydrogel coating can be utilised for various medical applications such as imaging and photothermal destruction of cancer cells. The effect of these shapes have also been investigated on Cyt C loading and release.

7. Results and Discussion

7.3 Characterization of AuNPs

Characterization studies have been performed for five different shaped AuNPs in this section, namely AuNR, AuHex, AuBP, AuNM and AuNS. Characterization of sizes and zeta potentials of bare AuNPs has been carried out using DLS. Uv-vis has been used to analyse the LSPR characteristics of gold. These AuNPs have then been coated with varying amounts of PEG followed by coating with varying amounts of hydrogel to optimise their properties. The variation in physico-chemical properties of the final coated NPs has been investigated by varying the temperature (25^OC to 45^OC) and pH (9 to 3) using DLS as well as via Uv-vis characterization.

7.3.1 Size and Zeta Potential of AuNPs

Figure 62 (a) and (b) show the sizes and zeta potential of different shaped AuNPs respectively. The smallest NPs are AuNR with a hydrodynamic size of 14.4 ± 0.7 nm. DLS results show that the sizes of other anisotropic NPs decrease in the order AuHex > AuBP > AuNM. AuNS have a hydrodynamic size of 22.5 ± 0.4 nm. It can be seen that the zeta potential for anisotropic NPs is positive while for AuNS is negative. The positive surface charge is due to the presence of CTAB coating. On the other hand, AuNS are citrate coated, indicated by negative surface charge. The charge embeds colloidal stability to the systems and prevent them from aggregating.
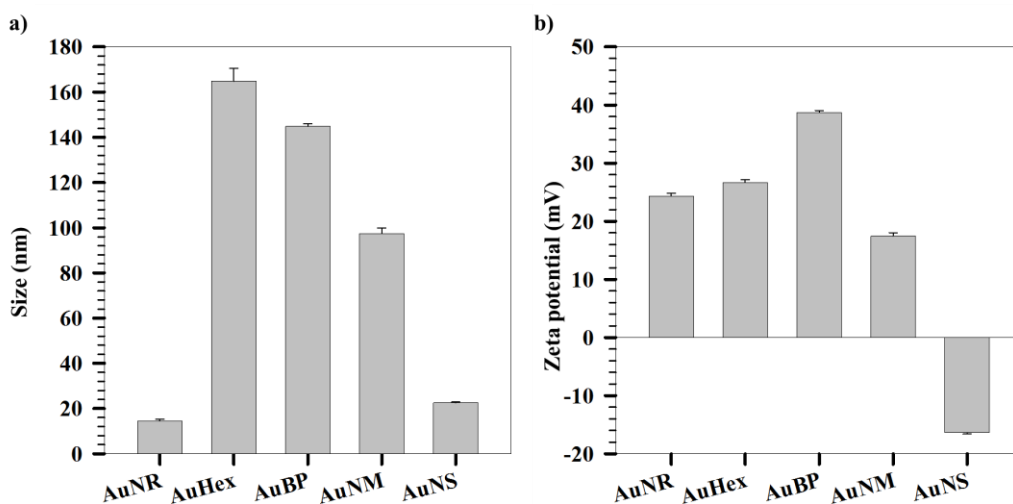
Figure 62 a) Size of bare AuNPs. b) Zeta potential of bare AuNPs.

7. Results and Discussion

Figure 63 shows the S(T)EM images of different AuNPs. Table 6 shows the size comparison obtained from S(T)EM and DLS of the different AuNPs. The S(T)EM size shows an average over the population of NPs. There exists an evident difference between the sizes obtained from DLS and S(T)EM images. DLS measures the hydrodynamic size based on the sphere having the diffusion coefficient as that of the parent particle. As the anisotropic NPs can have multiple axis of rotation, the measured size depends on geometry of spinning. As a result, there is a difference in the actual size of the NPs and the one measured by the DLS instrument. From S(T)EM imaging, it can be inferred that AuBP has the largest sizes of around 381.7 ± 106.8 nm, while AuNS have the smallest size of around 17.2 ± 2.2 nm. The DLS size for the AuNS is in close correspondence to its S(T)EM size due to their isotropic nature which strengthens the fact that DLS size measurements alone cannot be used to comment on the NPs' sizes.

Table 6 Comparison between the sizes obtained from S(T)EM and DLS.

AuNPs	Aspect Ratio (avg ± st. dev)	S(T)EM size (nm) Length/width	DLS size (nm)
AuNR	3.4 ± 0.5	41.8 ± 4.1 /12.6 ± 1.5	14.4 ± 0.7
AuHex	1.4 ± 0.2	232.6 ± 24.6 / 170.7 ± 20.1	164.8 ± 5.6
AuBP	3.8 ± 0.5	381.7 ± 106.8 / 106.5 ± 45.3	144.9 ± 1.1
AuNM	1.5 ± 0.4	117.7 ± 14.8 / 83.2 ± 13.6	97.4 ± 2.4
AuNS	-	17.2 ± 2.2	22.5 ± 0.4
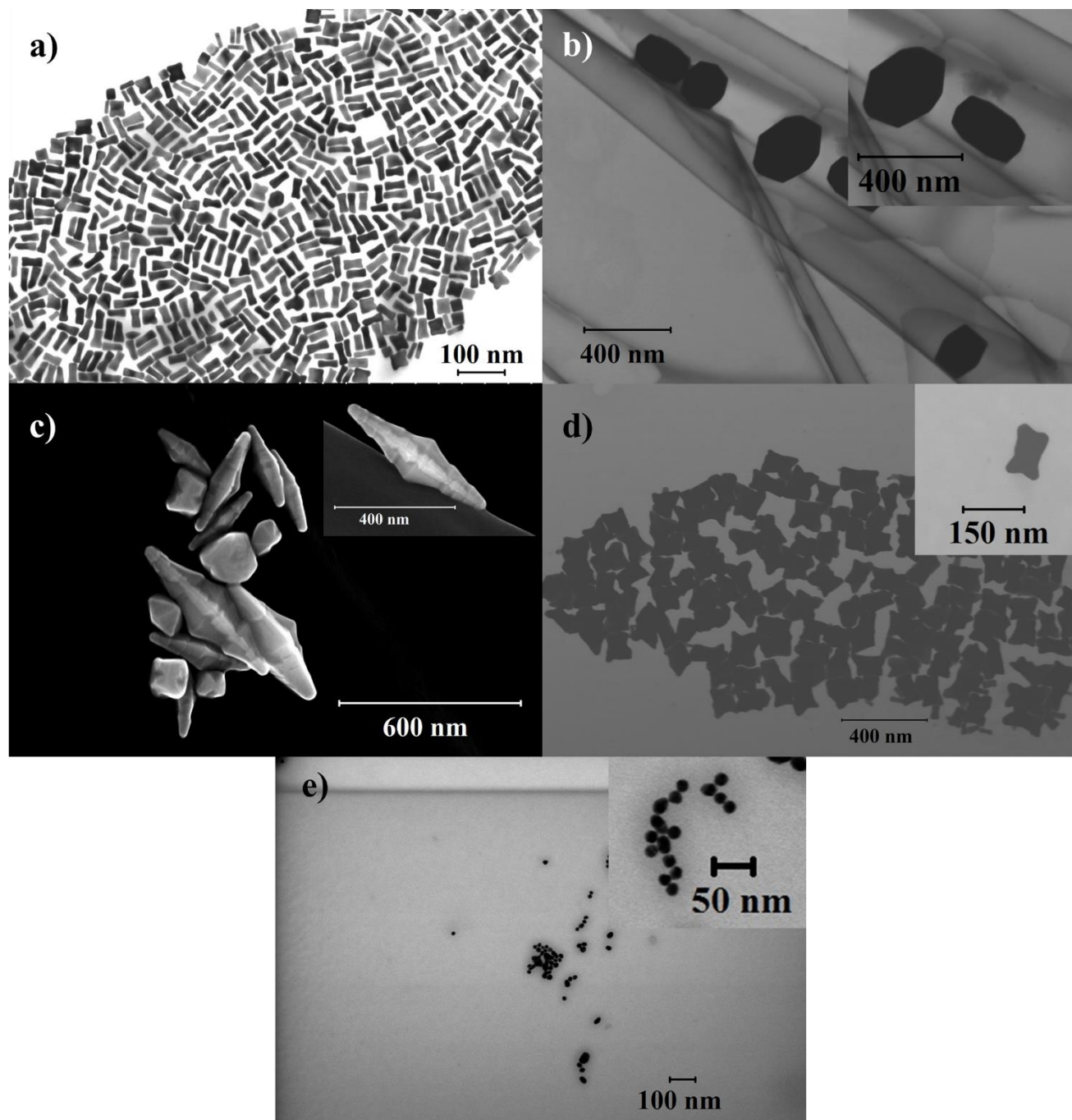
Figure 63 S(T)EM images of a) AuNR, b) AuHex, c) AuBP, d) AuNM and e) AuNS.
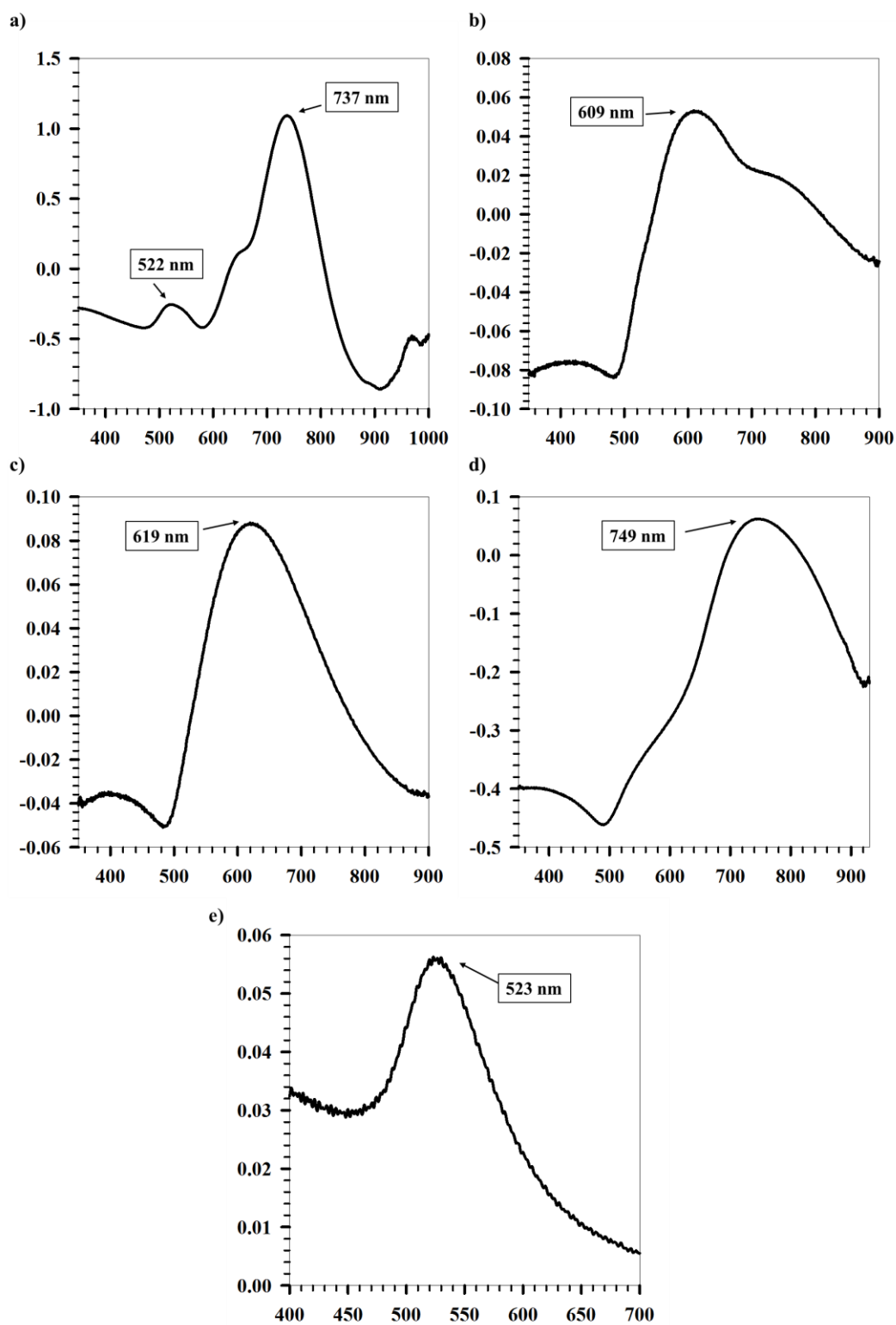
Figure 64 Uv-vis of PEG-hydrogel coated AuNPs. a) AuNR, b) AuHex, c) AuBP, d) AuNM, e) AuNS.

7. Results and Discussion

Figure 64 shows the Uv-vis characterization data for AuNPs. The absorbance peak of spherical gold is obtained at 520 nm which can be seen for AuNS having the peak at 523 nm [210]. AuNR exhibit two peaks corresponding to each of the two axes; transverse (522 nm) and longitudinal (737 nm). AuNM has an absorbance peak at 749 nm, close to that of AuNR, as both comprises of elongated etched features. The blue shift in AuNM is due to the larger size. Multifaceted NPs (AuHex and AuBP) have their peaks close to each other at 609 nm and 619 nm respectively.

PEG Coating

In order to replace the CTAB, PEG was coated on the anisotropic NPs. Three different concentrations of PEG were used (0.5 mg/ml, 1 mg/ml and 2 mg/ml). Figure 65 (a) shows the variation of size of AuNPs with varying PEG concentration. The size increases as the concentration of PEG is increased which indicates successful coating. This is further supported by a reduction in the zeta potential on addition of PEG, depicting substitution of cationic CTAB with anionic PEG (Figure 65 (b)).
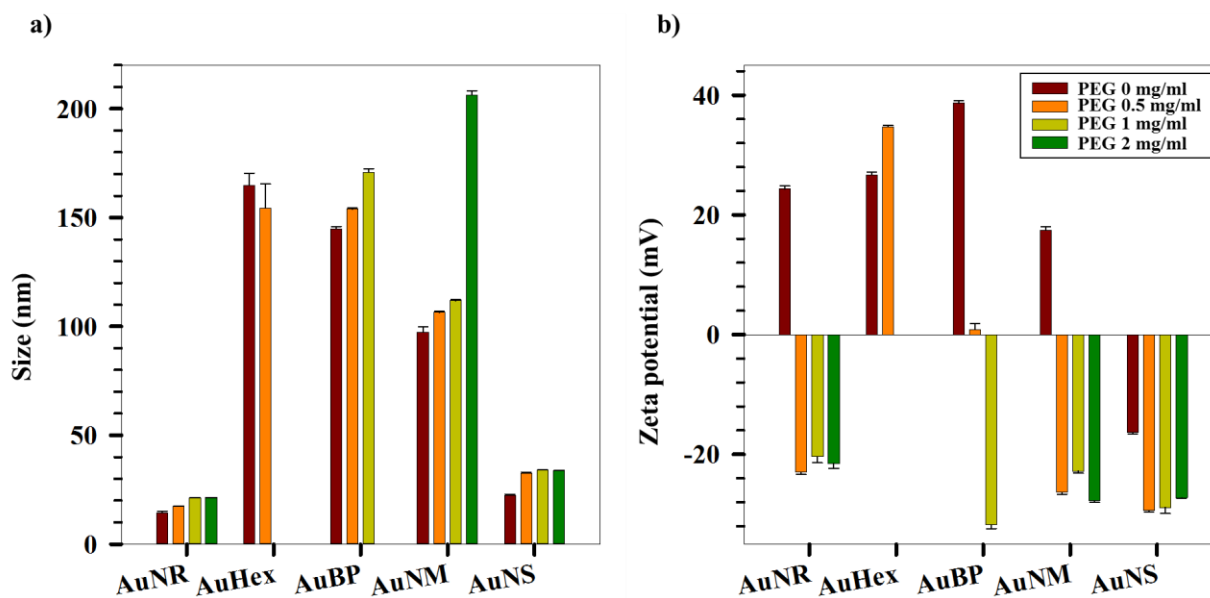
Figure 65 a) Size variation with PEG coating. b) Zeta potential variation with PEG coating.

7. Results and Discussion

Hydrogel Coating

PEG coated AuNPs were further coated with hydrogel C1. Figure 66 (a) and (b) show the variation of sizes and zeta potentials of PEG coated AuNPs with varying hydrogel concentrations. It is evident that the size of PEG coated AuNPs increases with increasing hydrogel concentration. The zeta potential also decreases with hydrogel coating. However, the actual arrangement of NPs and hydrogel cannot be inferred with DLS alone.
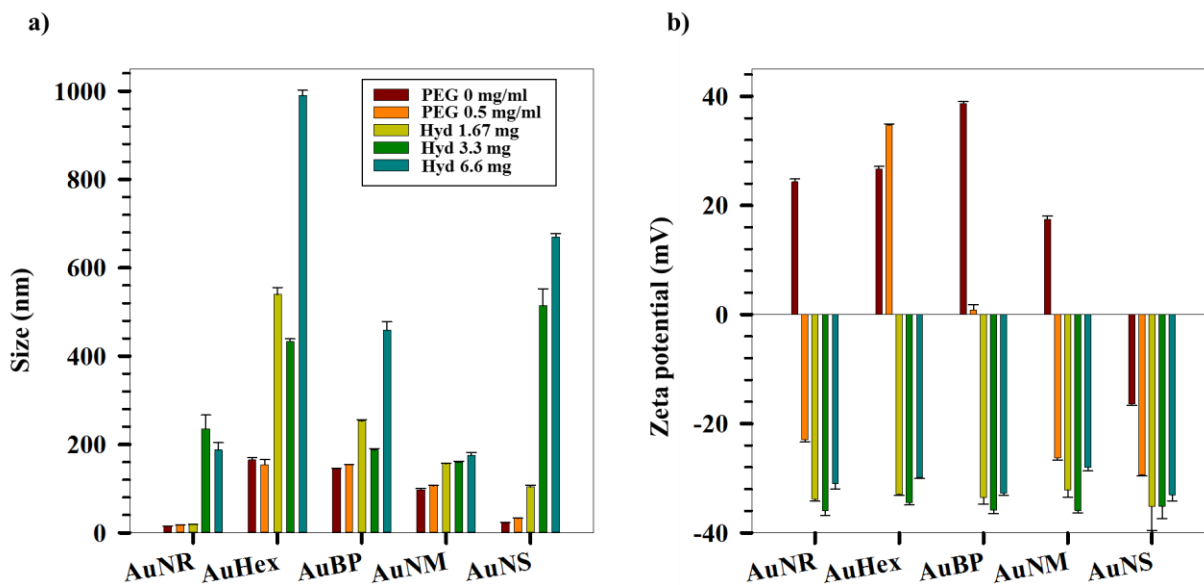
Figure 66 a) Size variation with hydrogel coating. b) Zeta potential variation with hydrogel coating.

Figure 67 shows the S(T)EM of PEG-hydrogel coated AuNPs. It must be noted that the NPs are located at the periphery of the hydrogels instead of the core. AuHex and AuBP have less particle concentration per unit volume with 3.3 mg hydrogel coating.
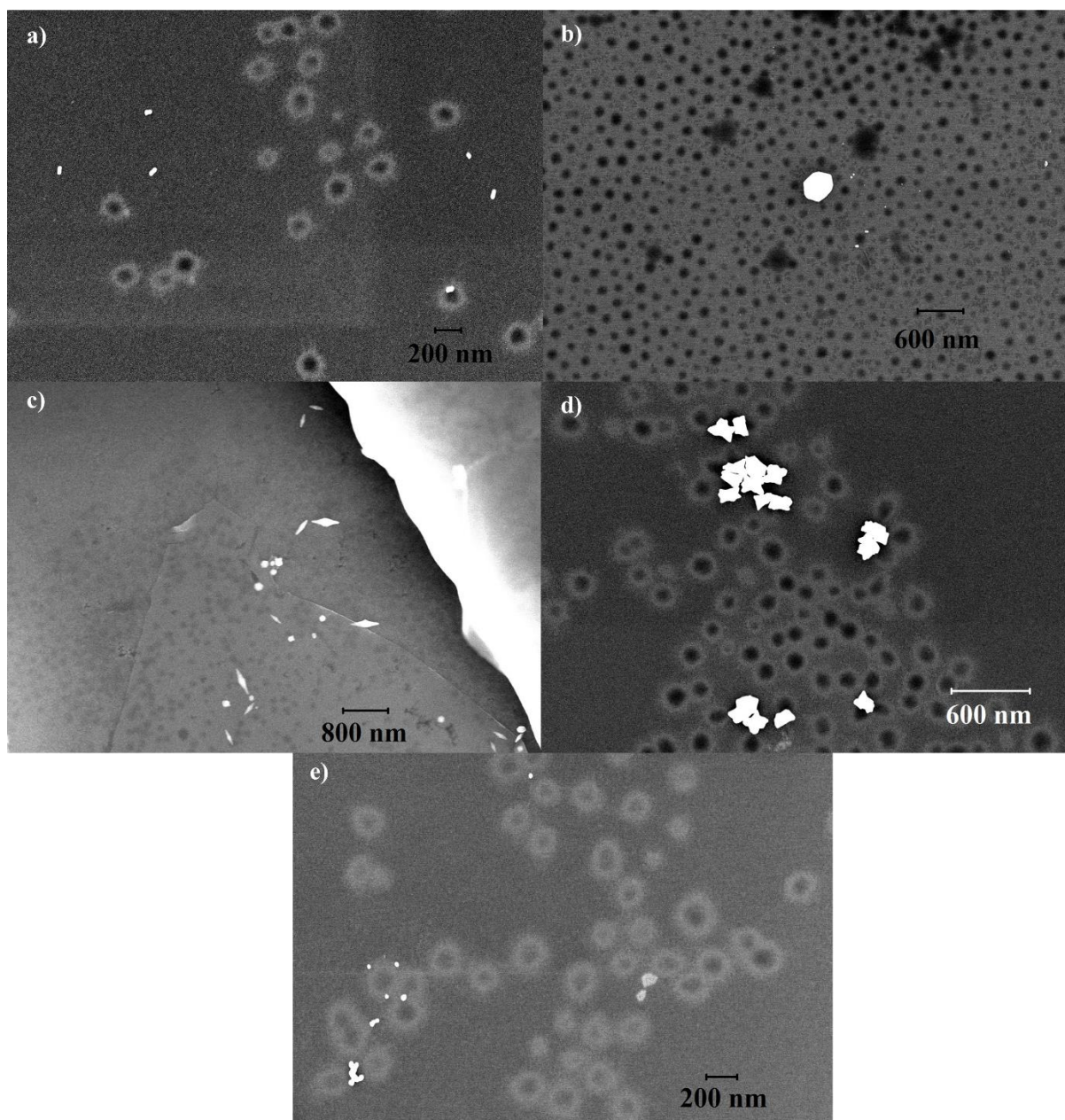
Figure 67 S(T)EM image of PEG-hydrogel coated AuNPs. a) AuNR, b) AuHex, c) AuBP, d) AuNM, e) AuNS.

The PEG concentration and hydrogel amount was taken to be 0.5 mg/ml and 3.3 mg respectively for further characterization studies.

Figure 68 shows the UV-vis data for bare AuNPs, PEG coated AuNPs and PEG-hydrogel coated NPs. A shift in the LSPR peaks of the AuNPs can been seen upon coating. The peak for AuNS undergoes a bathochromic (red) shift on coating with PEG due to its hydrophilic nature [211]. On coating with pNIPAM, the AuNS undergoes a blue shift. The longitudinal peak for AuNR also showed a blue shift from 737 nm to 725 nm for PEG and PEG-hydrogel coating respectively. A blue shift is also observed for AuHex, AuBP and AuNM whose peak shifts from 609 nm to 560 nm, 619 nm to 610 nm, and 749 nm to 728 nm respectively with PEG-hydrogel coating. The shift for AuNS was minimal with the peak going from 523 nm to 524 nm with PEG-hydrogel coating.

The incorporation of the hydrophilic component, hydrogel, with AuNPs, increases the water content of the system. Thus the NPs are in contact with water to a greater extent. This causes a blue shift in the peaks of the NPs.
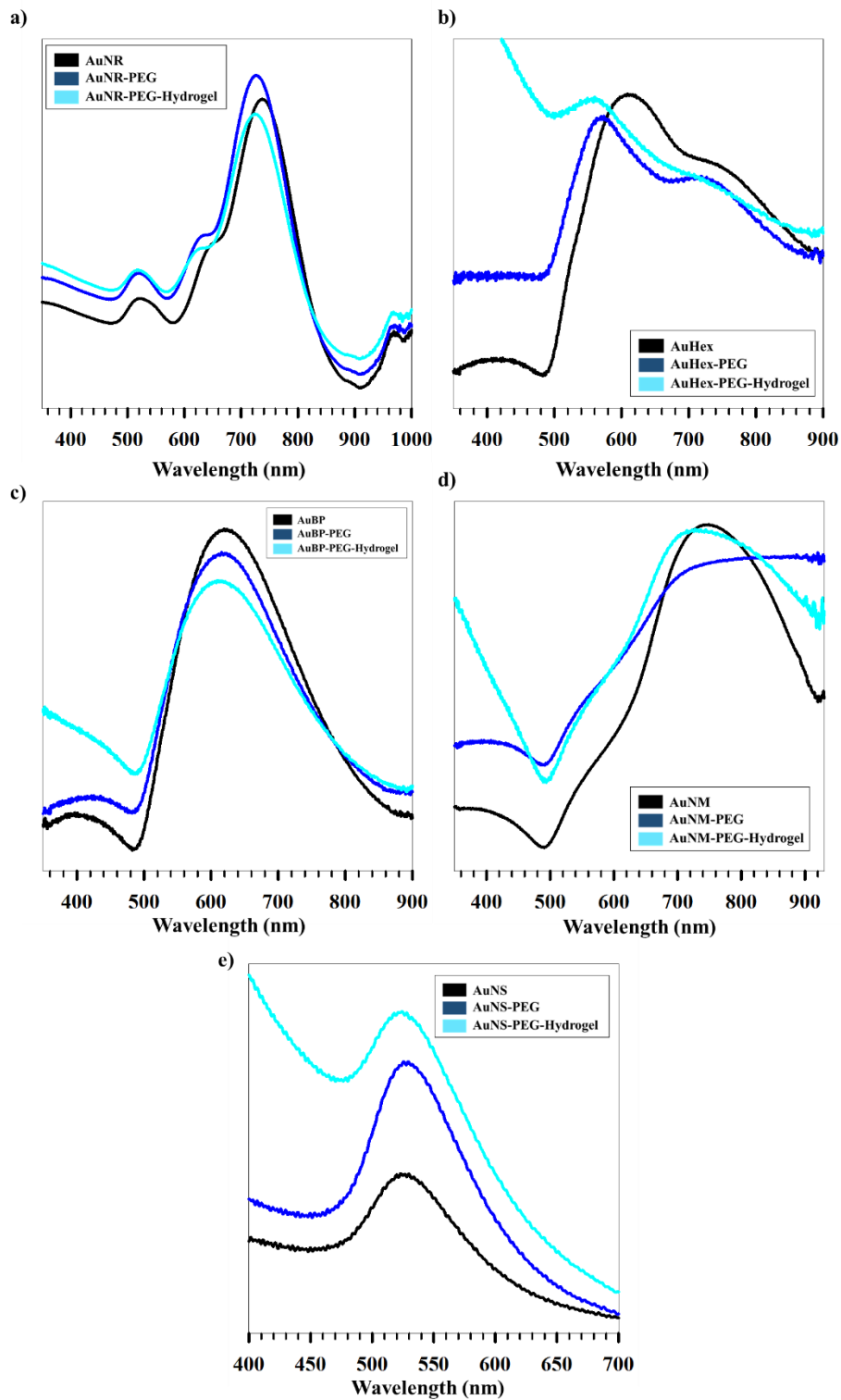
Figure 68 Uv-vis characterization of AuNPs, AuNPs-PEG and AuNPs-PEG-hydrogel. a) AuNR, b) AuHex, c) AuBP, d) AuNM, e) AuNS.

7. Results and Discussion

7.3.2 Variation of Size and Zeta Potential with pH at 25°C

Figure 69 (a) and (b) show the variation of size and zeta potential for AuNR with pH at 25°C. it can be seen from the figures that the rods are unstable and their size fluctuates as the pH is changed from basic to acidic. However, the zeta potential shows a much stable dependence on pH. The decrease in the absolute value of zeta potential on lowering of pH is due to the inability of the AAc groups to dissociate in the presence of a much stronger acid (HCl) as observed for hydrogel also in section 7.1.1.2.
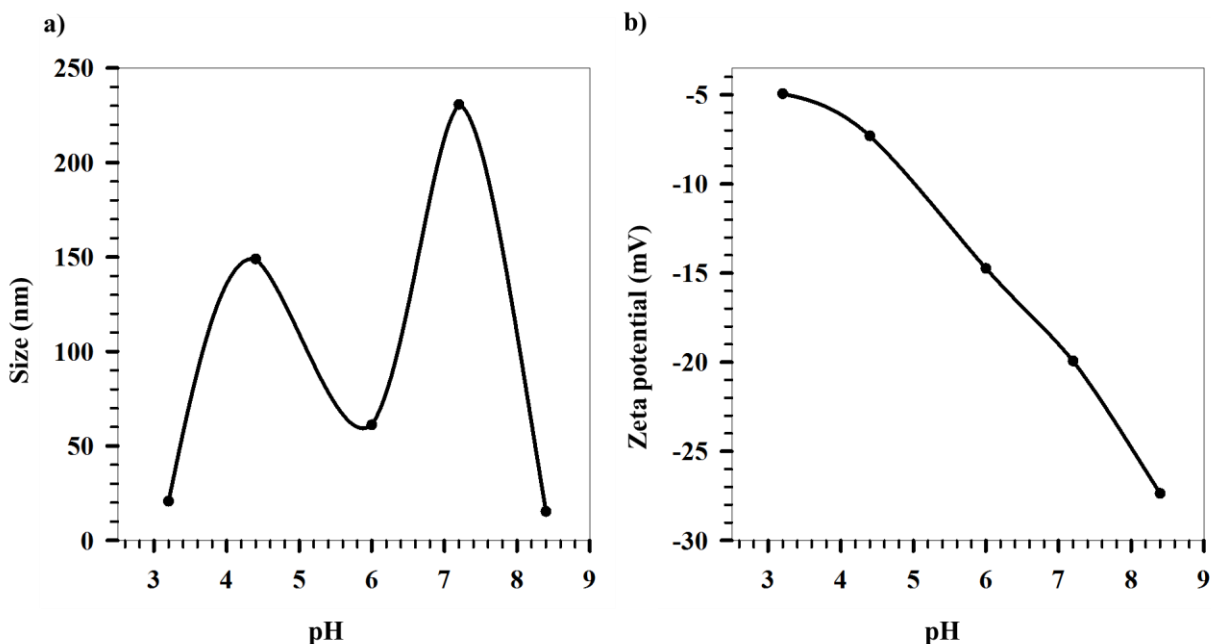
Figure 69 a) Size variation of AuNR with pH @25°C. b) Zeta potential variation of AuNR with pH @25°C.

The size and zeta potential dependence on pH of AuHex is shown by Figure 70 (a) and (b). the size of the AuHex decreases on either side of normal pH condition. At lower pH, the size decreases as the electrostatic repulsion decreases due to lowering in the surface charge density. The decreases in size at higher pH can be attributed to the fact that as the surface charge increases, it causes greater repulsion within the AuNPs hydrogel network. This might result in the breakage of the hydrogel network into smaller moieties.

7. Results and Discussion
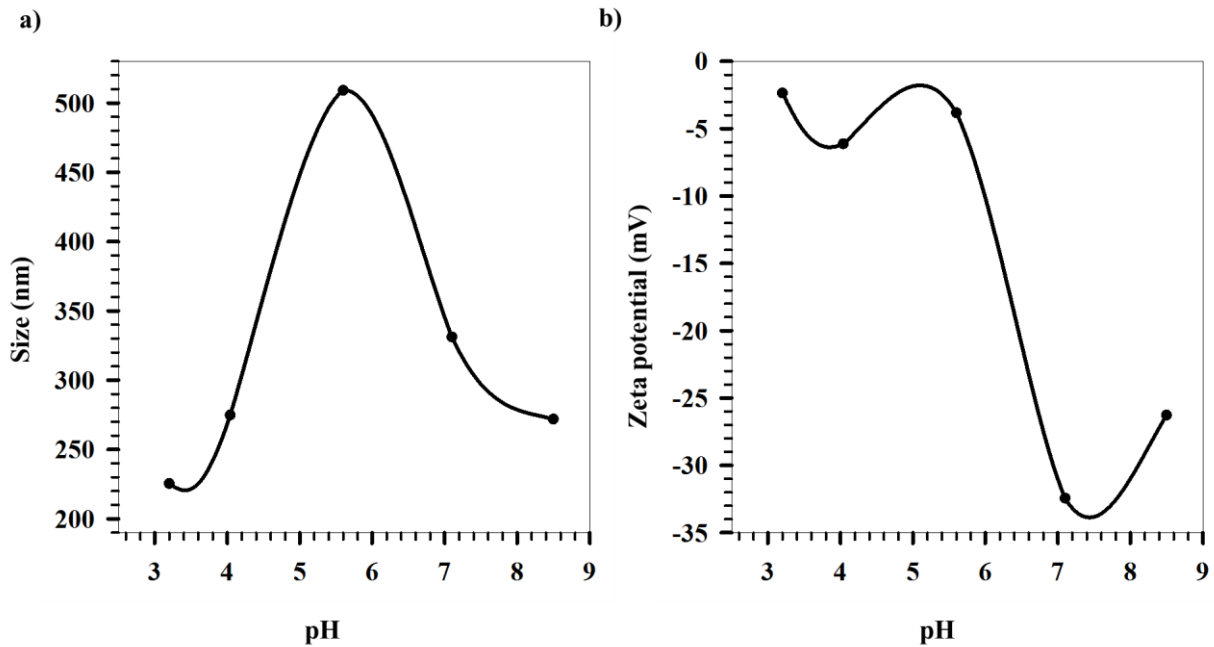
Figure 70 a) Size variation of AuHex with pH @25OC. b) Zeta potential variation of AuHex with pH @25OC.

Sizes of AuBP, AuNM and AuNS show a much stable dependence with pH (Figure 71 (a), (c) and (e)). The size for these three AuNPs increases as the pH shifts from basic to acidic. As the surface charge density decreases owing to the acidic medium, the AuNPs come closer and act as cross-linkers. Thus, the overall size of the hydrogel network increases. The zeta potentials of these NPs show the same trend as with AuNR and AuHex. The increase in negative zeta potential towards the basic region is due to the dissociation of AAc groups thereby increasing the surface charge. The dissociation is hindered at lower pH due to the presence of HCl.
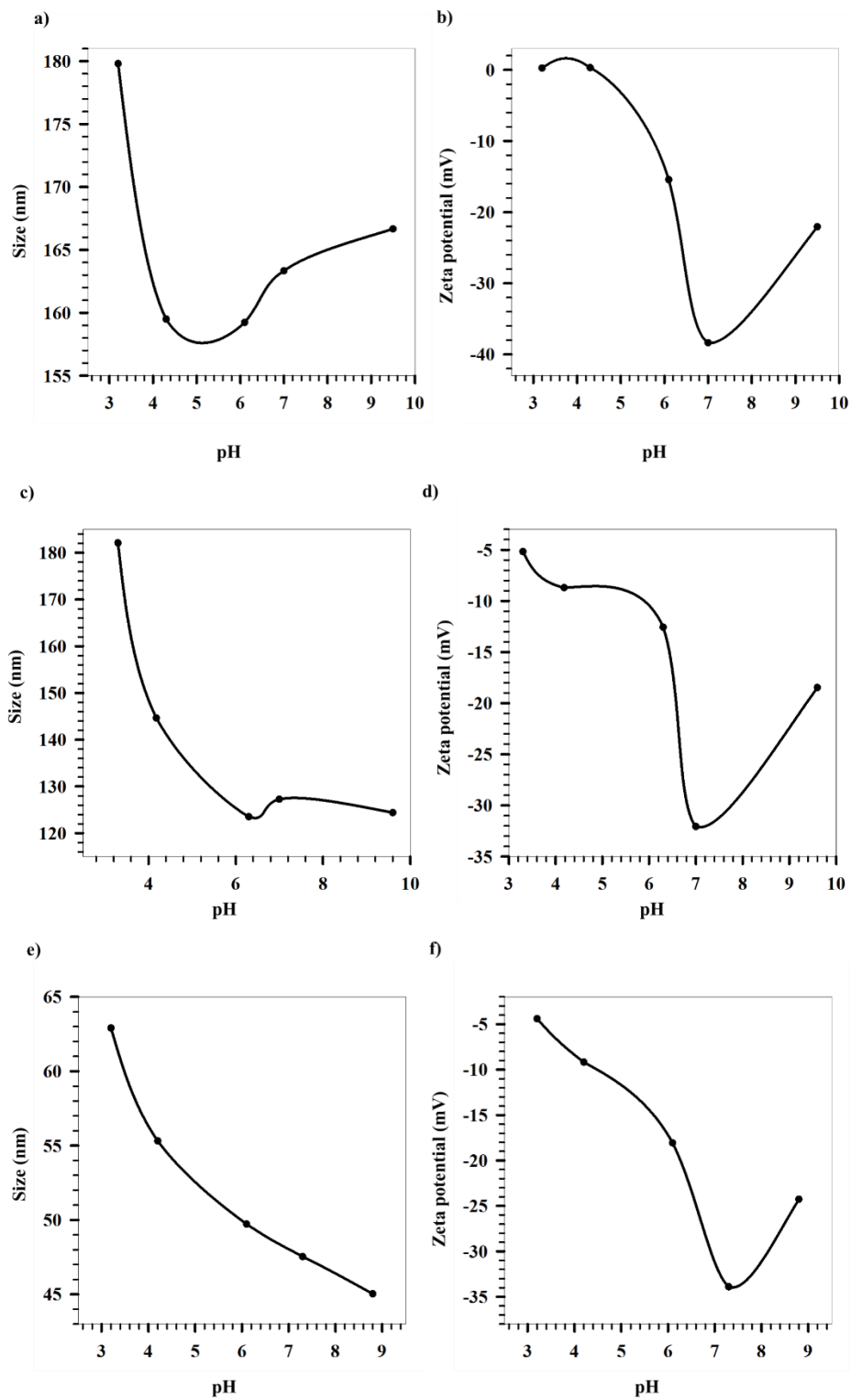
Figure 71 a), c), e) Size variation of AuBP, AuNM and AuNS with pH @ 25ᴼC respectively. b), d), e) Zeta potential variation of AuBP, AuNM and AuNS with pH @ 25ᴼC respectively.

7. Results and Discussion

7.3.3 Variation of Size and Zeta Potential with pH at 45°C

At 45°C, the sizes of AuNR, AuHex and AuNS increase with decreasing pH (Figure 72 (a), (c) and (e)). The increase may be a result of AuNPs coming closer to each other due to decrease in surface charge at lower pH. As the NPs come together, they pull the hydrogel network along with them acting as cross-linkers across different polymeric chains. This causes an increase in the overall hydrogel network.

However, AuBP and AuNM show a reverse size dependence (Figure 73 (a) and (c)). The size decreases as pH decreases. Due to their much larger sizes and different particle concentration, the NPs are prevented from coming closer due to steric hindrance. Therefore, the coated NPs stay apart and the hydrogel network on the surface of these NPs collapses above VPTT thereby causing an overall reduction in size of the system. Also, due to lower NP concentration in the solution, hydrogel concentration plays a decisive role in governing the effective size of the system.

The zeta potential follows the natural dependency trend for all the AuNPs (Figure 72 (b), (d), (f), and Figure 73 (b) and (d)). The potential increases negatively at basic pH as a result of AAc group dissociation. HCl dissociates preferentially over AAc at lower pH thereby reducing the absolute zeta potential of the system.
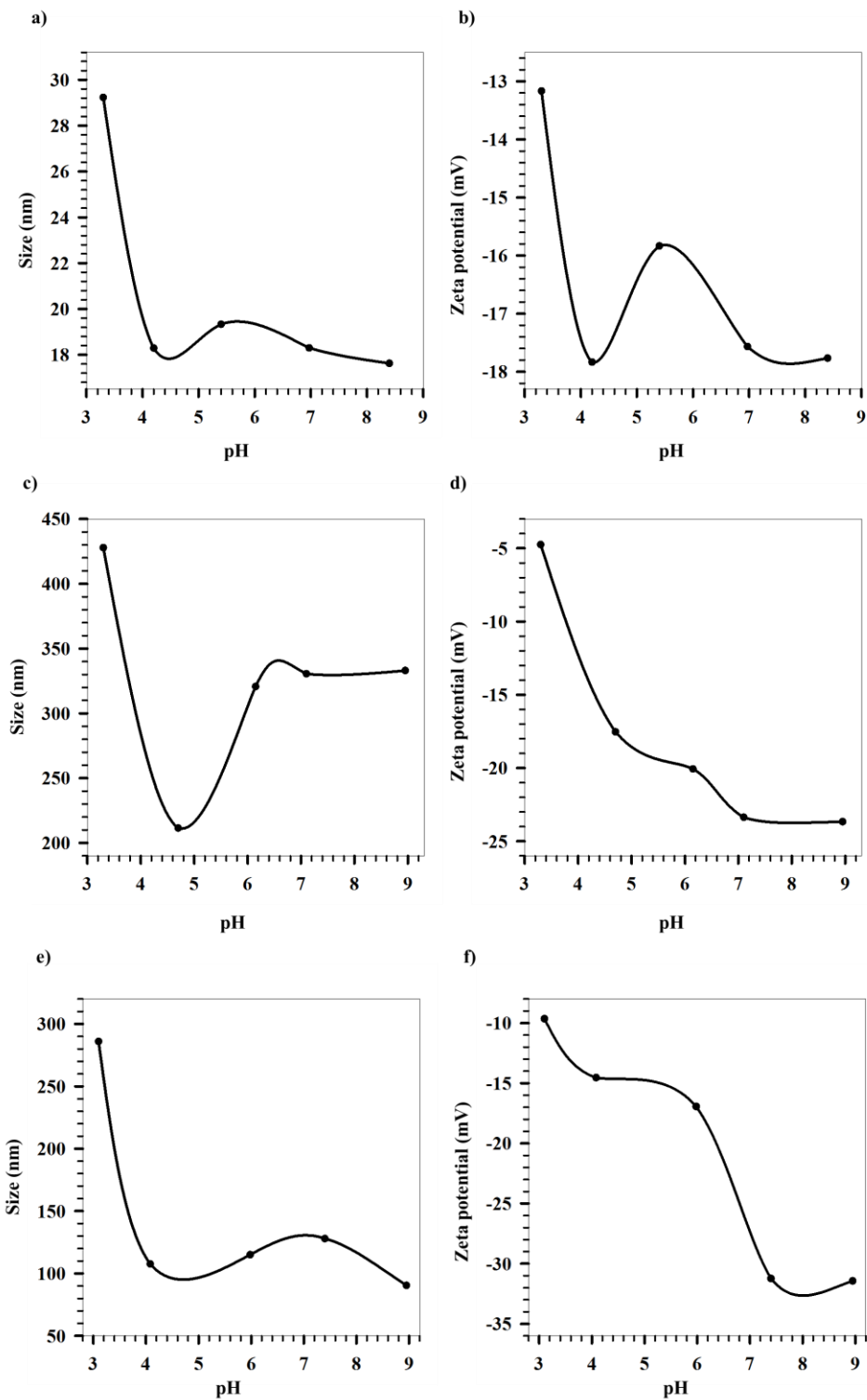
Figure 72 a), c), e) Size variation of AuNR, AuHex and AuNS with pH @ 45°C respectively. b), d), e) Zeta potential variation of AuNR, AuHex and AuNS with pH @ 45°C respectively.

7. Results and Discussion
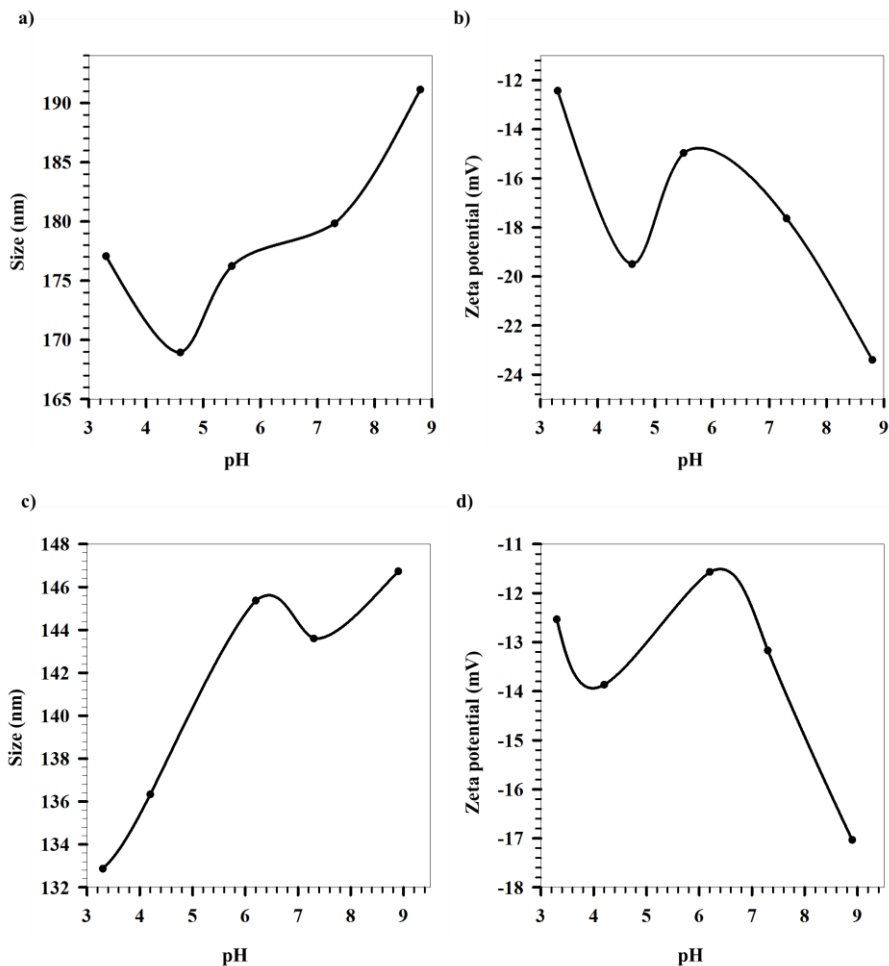
Figure 73 a), c) Size variation of AuBP and AuNM with pH @ 45°C respectively. b), d) Zeta potential variation of AuBP and AuNM with pH @ 45°C respectively.

After performing characterization studies, the AuNPs were loaded with Cyt C and its loading and release was analysed.

Volumetric collapse efficiency (V.C.E.) was calculated for anisotropic NPs based on the size variation from 25°C at normal pH to 45°C at pH 3. While AuNR and AuHex showed collapse with V.C.E. of 89% and 41% respectively, AuBP and AuNM underwent swelling with a negative V.C.E. of 37% and 24% respectively.

7. Results and Discussion
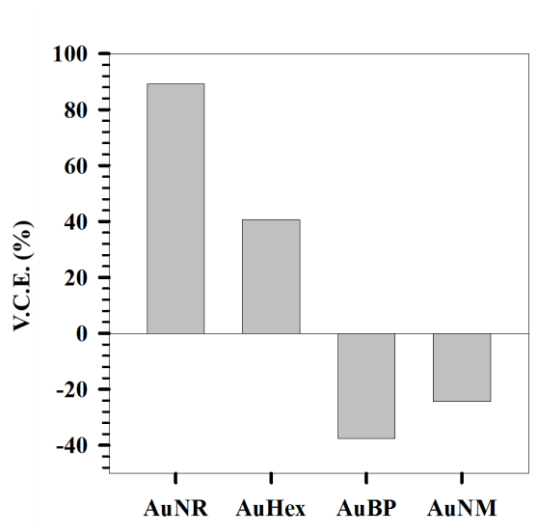
Figure 74 V.C.E. of anisotropic AuNPs.

NR being smaller in size, are effectively incorporated in the hydrogel matrix thereby enhancing their cross-linking effect on the hydrogel network. For larger size NPs, the AuNPs might be present outside the hydrogel network and may be linked to more than as shown by the S(T)EM image in Figure 67. It was shown in section 7.3.3 that at 45^OC and pH 3, the absolute zeta potential for all the systems reduces. Less surface charge results in reduced electrostatic repulsion between NPs and they tend to agglomerate. As the particle come closer, they tag along the hydrogels with them. This increases the overall size of the hydrogel network. It should be noted that as mentioned in section 7.3.1, the DLS measures the hydrodynamic diameter of the particle based on the sphere having the diffusion coefficient of the parent particle. Therefore, in order to check for the viability of DLS measurements for anisotropic NPs, S(T)EM analysis should be performed.

7.4 Loading and Encapsulation

Two different quantities of hydrogel C1 (1.67 mg and 3.3 mg) were coated on the AuNPs to study the effect of amount of hydrogel on drug loading and release studies. Cyt C was loaded on the PEG-hydrogel coated AuNPs via the breathing in method. The L.E. of AuNPs is shown in Figure 75 (a). In case of 1.67 mg hydrogel, lower loading was achieved for AuNR (43%), AuHex (43%) and AuNS (45%). L.E. for AuBP and AuNM were 84% and 71% respectively. As the amount of hydrogel was increased from 1.67 mg to 3.3 mg, the loading efficiencies of AuNR, AuHex, AuNM and AuNS improved to 72%, 84%, 81% and 79% respectively. There was a slight decrease in the L.E. of AuBP (71%). The greater quantity of hydrogel enables larger quantities of Cyt C to be absorbed in the hydrogel matrix thereby increasing the loading capacity of the entire system. Also shown by Figure 57 (a), hydrogel has higher L.E. than coated NPs. Therefore, more the hydrogel incorporated on the NPs' surface, greater is the L.E. Additionally, AuHex and AuBP have the maximum L.E. due to higher hydrogel content per unit volume as seen by the S(T)EM in Figure 67. Higher percentage of hydrogel enables more drug to be engulfed in the hydrogel core.
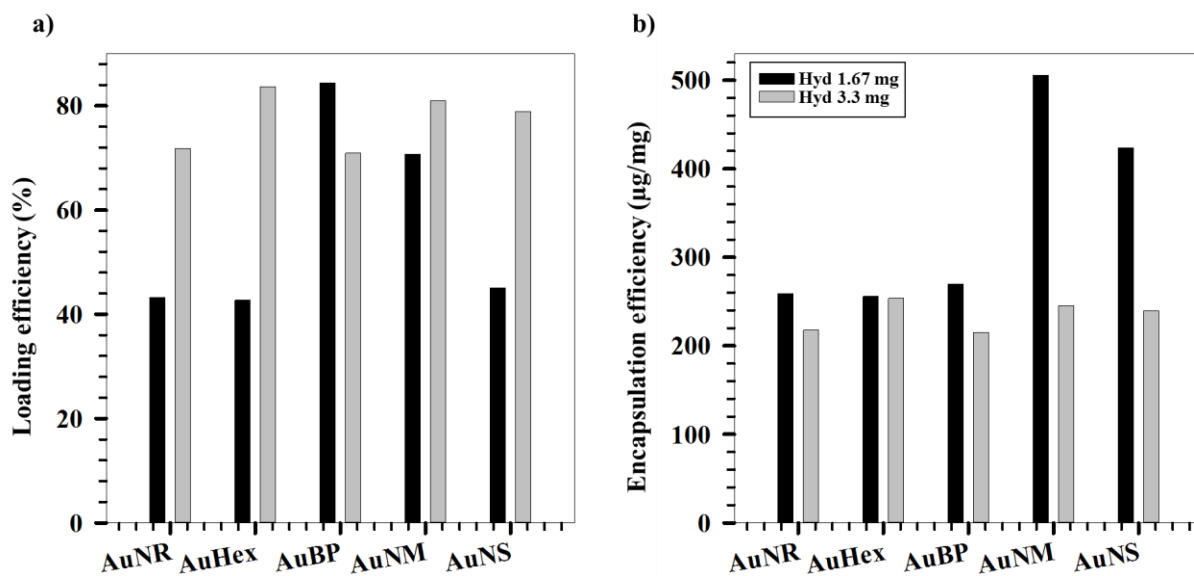
Figure 75 a) Loading efficiencies of AuNPs b) Encapsulation efficiencies of AuNPs.

The E.E. of the AuNPs seem to decrease with increasing amount of hydrogel. It must be noted that the E.E is calculated on hydrogel basis and not on AuNP basis. Thus, as the amount of hydrogel

increases the denominator term increases, in turn lowering the E.E. of the system as depicted by formula in <u>Appendix A</u>.

7.5 Cyt C Release and Kinetics

Figure 76 (a) and (b) show the release profiles of AuNPs containing 1.67 mg and 3.3 mg hydrogel respectively. The release of Cyt C was performed using dialysis based release set-up. High temperature (45^OC) and low pH (3.5) was maintained throughout the duration of the release study. As seen in Figure 75 (a), a higher loading is associated with a thicker hydrogel coating. With more drug in the hydrogel network and greater number of hydrogel chains collapsing, the driving force for Cyt C release increases. Figure 77 shows a comparison of the maximum drug released on using different weights of hydrogel. A higher release was achieved for all the coated AuNPs with 3.3 mg hydrogel.
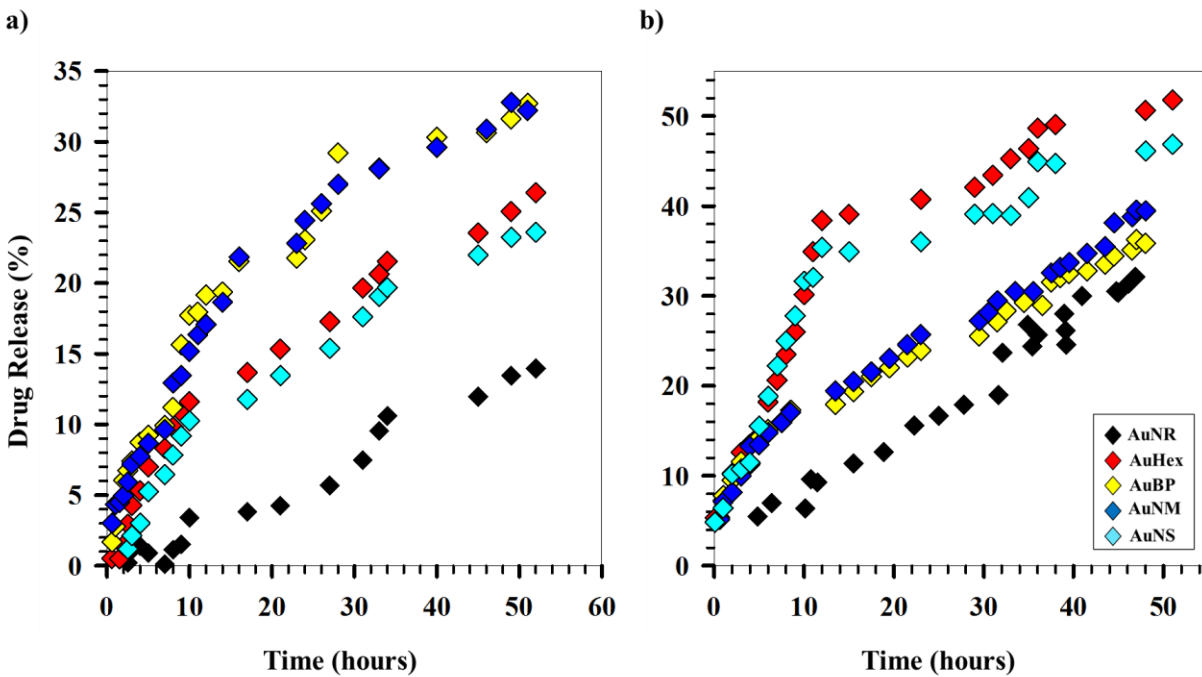
Figure 76 Cyt C release profile of AuNPs with a) 1.67 mg hyd. b) 3.3 mg hyd.

A greater impact of hydrogel concentration is seen on smaller NPs (AuNR, AuHex and AuNS) almost doubling the maximum release of Cyt C (more than 3 folds for AuNR). The smaller NPs act as cross-linkers in between the hydrogel network aiding the collapse of the hydrogel network. With 3.3 mg hydrogel coating, the NPs bind with more number of matrix causing a greater collapse. As for AuBP, the large size of the NPs prevents the effective collapse of the hydrogel network after a limit. In the case of AuNM, the higher concentration of NPs within a specific volume undermines (Figure 67 (d)) the effect of the hydrogel matrix. Thus, in both scenarios, the effect of increased amounts of hydrogel is diminished.

It can also be observed that the maximum release% achieved with 1.67 mg of hydrogel C1 is reached in almost 10 hours with 3.3 mg C1 in all the AuNP cases. Higher Cyt C content results in a greater concentration gradient, forcing faster release of the drug.
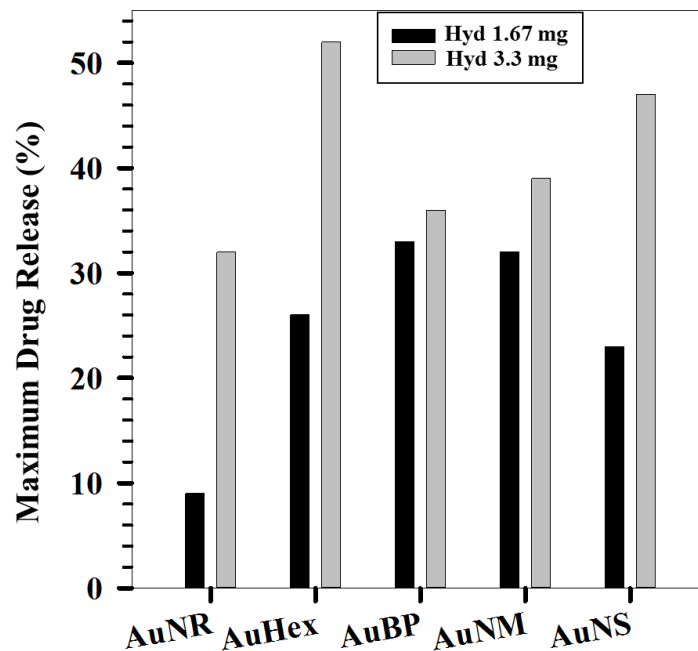
Figure 77 Maximum Cyt C release comparison at different hydrogel concentrations.

7. Results and Discussion

Zero order, first order, Higuchi and power law models were fitted to the release data for all the AuNPs. From Figure 76 (a), it can be inferred that the release of Cyt C from AuNR and AuBP happens in two modes in the same release profile. For AuNR, it's an initial slow release which increases after approximately 10 hours. AuBP undergo a fast release till 10 hours which slows down with further passage of time. To analyse the release in a better manner, the release prfiles of AuNR and AuBP were divided into two parts; part-I and part-II. The other NPs (AuHex, AuNM and AuNS) have a gradual slope.

Figure 78 (a)-(d) show the fitted release models for AuNR coated with 1.67 mg C1. The release profile was divided into two sections at approximately 10 hours and their release kinetics was studied separately. For both the cases, AuNR shows the best fit with zero order kinetic model with R^2 values of 0.9708, part-I (Figure 78 (a)) and 0.9311, part-I (Figure 78 (c)). The values of rate constants (k) for this system are 0.03511 hour^{-1} and 0.0418 hour^{-1}.

Figure 78 (b) and (d) show the fitted release models for AuHex coated with 1.67 mg C1. AuHex show the best fit with zero order kinetic model with R^2 = 0.9889. The value of rate constant for this system is k = 0.0184 hour^{-1}.
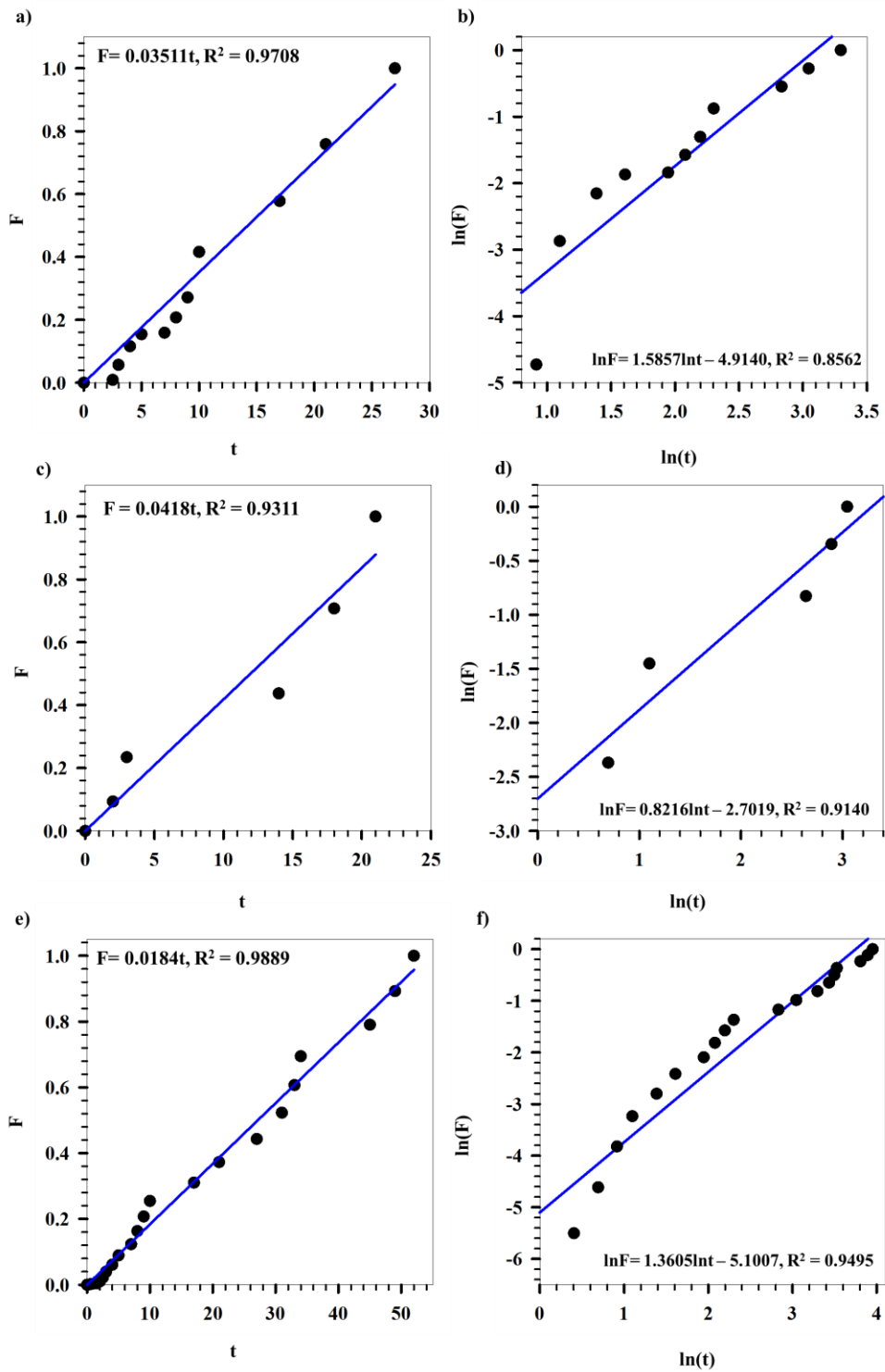
Figure 78 Release kinetics models for AuNPs coated with 1.67 mg hydrogel. Zero order model a) AuNR part-I, c) AuNR part-II, e) AuHex. Power law b) AuNR part-I, d) AuNR part-II, f) AuHex.
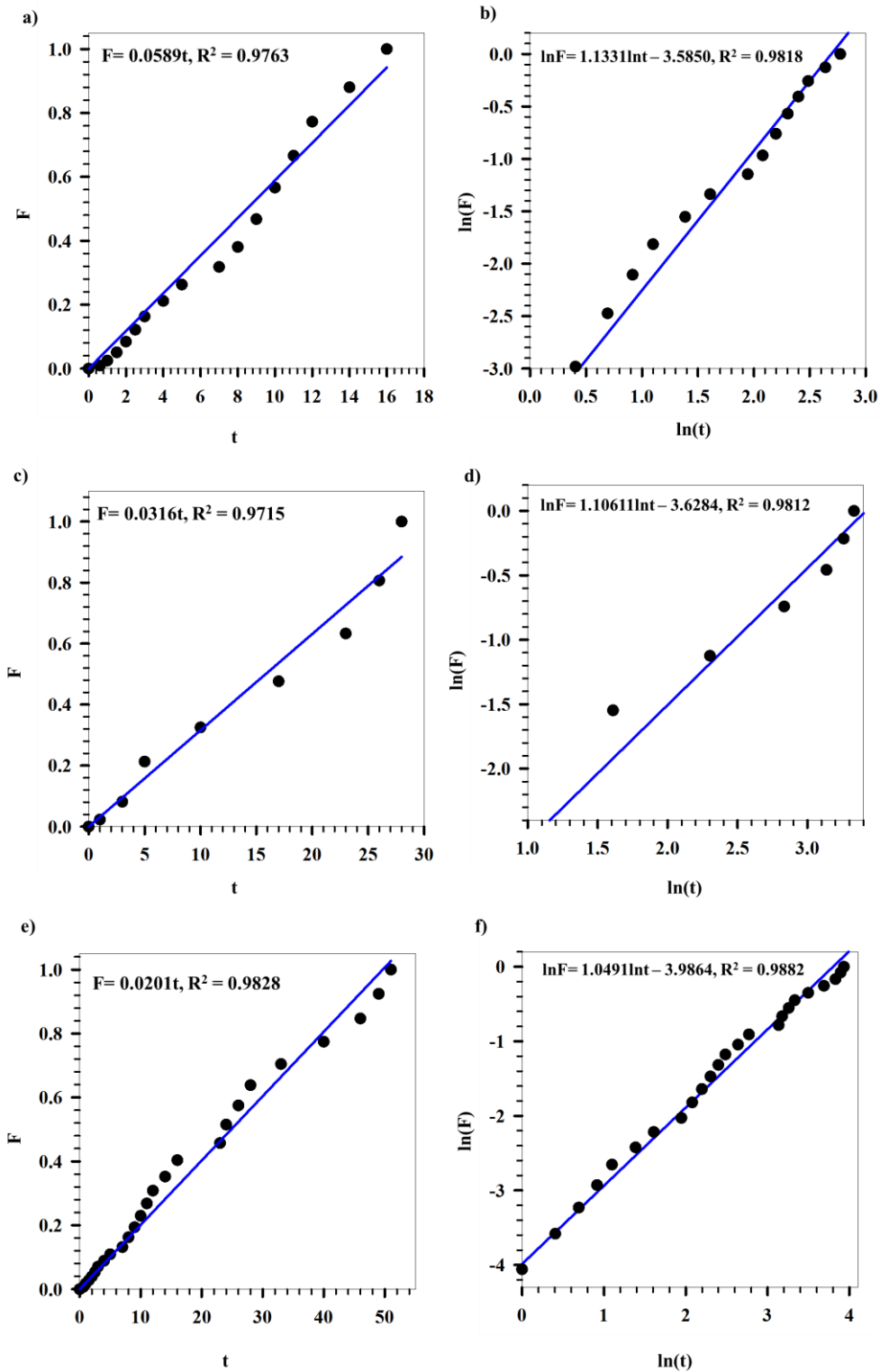
Figure 79 Release kinetics models for AuNPs coated with 1.67 mg hydrogel. Zero order model a) AuBP part-I, c) AuBP part-II, e) AuNM. Power law b) AuBP part-I, d) AuBP part-II, f) AuNM.

7. Results and Discussion

Figure 79 (a)-(d) show the fitted release models for AuBP coated with 1.67 mg C1. The release profile was divided into two sections at approximately 10 hours and their release kinetics was studied separately as in the case of AuNR. For both the cases, AuBP shows the best fit with zero order kinetic model with R^2 values of 0.9763, part-I (Figure 79 (a)) and 0.9715, part-II (Figure 79 (c)). The values of rate constants (k) for this system are 0.0589 hour^{-1} and 0.0316 hour^{-1}.

Figure 79 (b) and (d) show the fitted release models for AuNM coated with 1.67 mg C1. AuNM show the best fit with zero order kinetic model with R^2 = 0.9828. The value of rate constant for this system is k = 0.0201 hour^{-1}.

Figure 80 (a) and (b) show the fitted release models for AuNS coated with 1.67 mg C1. AuNS show the best fit with zero order kinetic model with R^2 = 0.9821. The value of rate constant for this system is k = 0.01781 hour^{-1}.
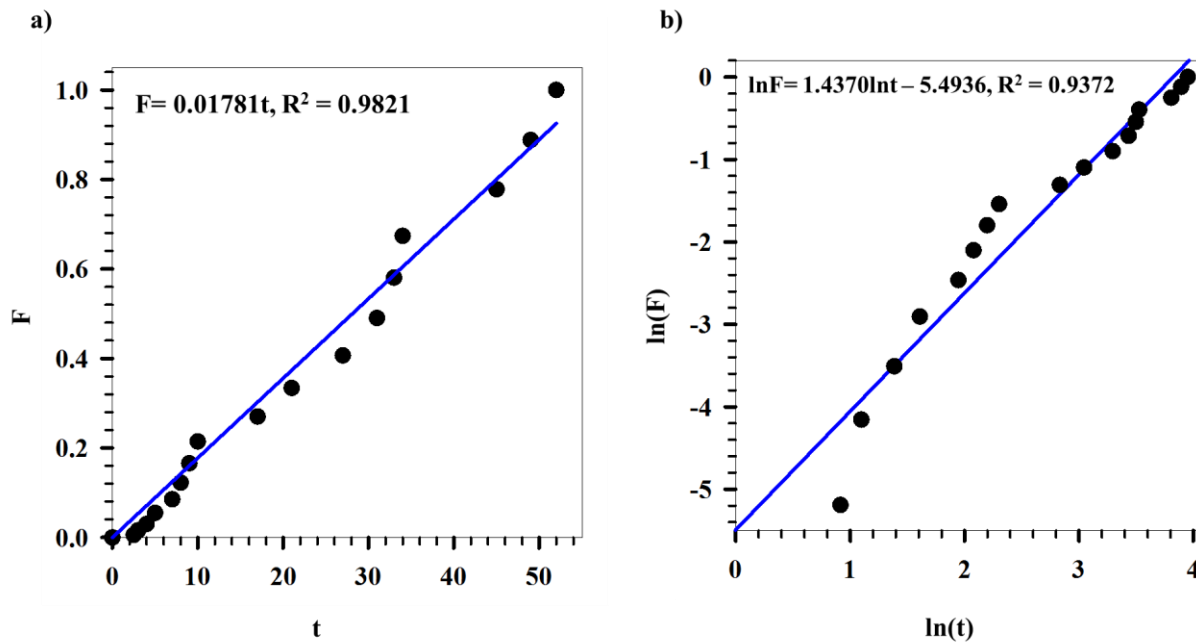
Figure 80 Release kinetics models for AuNS coated with 1.67 mg hydrogel. a) Zero order model. b) Power law.

Table 7 summarises the values of release rate constants, release orders and the time for 50% drug release ($t_{1/2}$) for the different AuNPs coated with 1.67 mg hydrogel.

7. Results and Discussion

Table 7 Release rate constant, order and t1/2 for the 1.67 mg hydrogel coated AuNPs.

Sample	Rate constant, k (hour^{-1})	Release order	$t_{1/2}$ (hours)
AuNR			
part-I	0.0351	Zero order	14.2
part-II	0.0418	Zero order	11.9
AuHex	0.0184	Zero order	27.1
AuBP			
part-I	0.0589	Zero order	8.5
part-II	0.0316	Zero order	15.8
AuNM	0.0201	Zero order	24.9
AuNS	0.0178	Zero order	28.1

All the AuNPs follow a zero order kinetics. The increase in value of rate constant for AuNR from 0.351 hours^{-1} to 0.0418 hours^{-1}, shows an increase in release rate which further substantiates the claim that the AuNR follow two distinct release patterns. Similarly, a decrease in the rate constant value for AuBP from 0.0589 hours^{-1} to 0.0316 hours^{-1} proves a decrease in release rate.

7. Results and Discussion

The values of release exponent, geometry and transport mechanism have been summarised in Table 8.

Table 8 Release exponent and transport mechanisms shown by 1.67 mg hydrogel coated AuNPs.

Samples	Release exponent (n)	Geometry	Transport mechanism
AuNR			
part-I	1.59	Thin film	Super Case-II transport
part-II	0.82	Sphere or Cylinder	Anomalous
AuHex	1.36	Thin film	Super Case-II transport
AuBP			
part-I	1.13	Thin film	Case-II transport
part-II	1.11	Thin film	Case-II transport
AuNM	1.05	Thin film	Case-II transport
AuNS	1.44	Thin film	Super Case-II transport

It is seen from Table 8 that the smaller NPs (AuNR and AuNS) have a higher initial release exponent than their other counterparts. This might be due to the fact that due to their small sizes, the hydrogels can accommodate them quite easily into their matrix, thereby increasing the cross-linking effect of the NPs. However, for larger NPs (AuHex, AuBP, and AuNM) the effect cross-linking is poor due to their poor embedment in the hydrogel network. Thus, the AuNR have a higher initial release exponent which decreases with time due to the decrease in diffusion driving force owing to the decrease in the concentration of Cyt C inside the hydrogel matrix. Due to lower concentration of hydrogel in the system, a coating is achieved. Thus, the collapse of the hydrogel is faster and release conformation takes the shape of a thin film as depicted by high initial value of release exponent.

7. Results and Discussion

In cases of AuNPs coated with 3.3 mg hydrogel C1, they showed multiple release regimes in the time studied. Therefore, the release profiles of these AuNPs were divided at relevant junctions in order to achieve a better fit of the release kinetics data.

Figure 81 shows the fitted release models for AuNR coated with 3.3 mg C1. The release profile was divided into two sections at approximately 16 hours and their release kinetics was studied separately. For both the cases, AuNR shows the best fit with zero order kinetic model with R^2 values of 0.9674, part-I (Figure 81 (a)) and 0.9279, part-II (Figure 81 (c)). The values of rate constants (k) for this system are 0.0636 hour^{-1} and 0.0371 hour^{-1}.

Figure 82 shows the fitted release models for AuHex coated with 3.3 mg C1. The release profile was divided into two sections at approximately 12 hours and their release kinetics was studied separately. For both the cases, AuHex shows the best fit with zero order kinetic model with R^2 values of 0.9357, part-I Figure 82 (a)) and 0.8057, part-II (Figure 82 (c)). The values of rate constants (k) for this system are 0.0691 hour^{-1} and 0.0226 hour^{-1}.
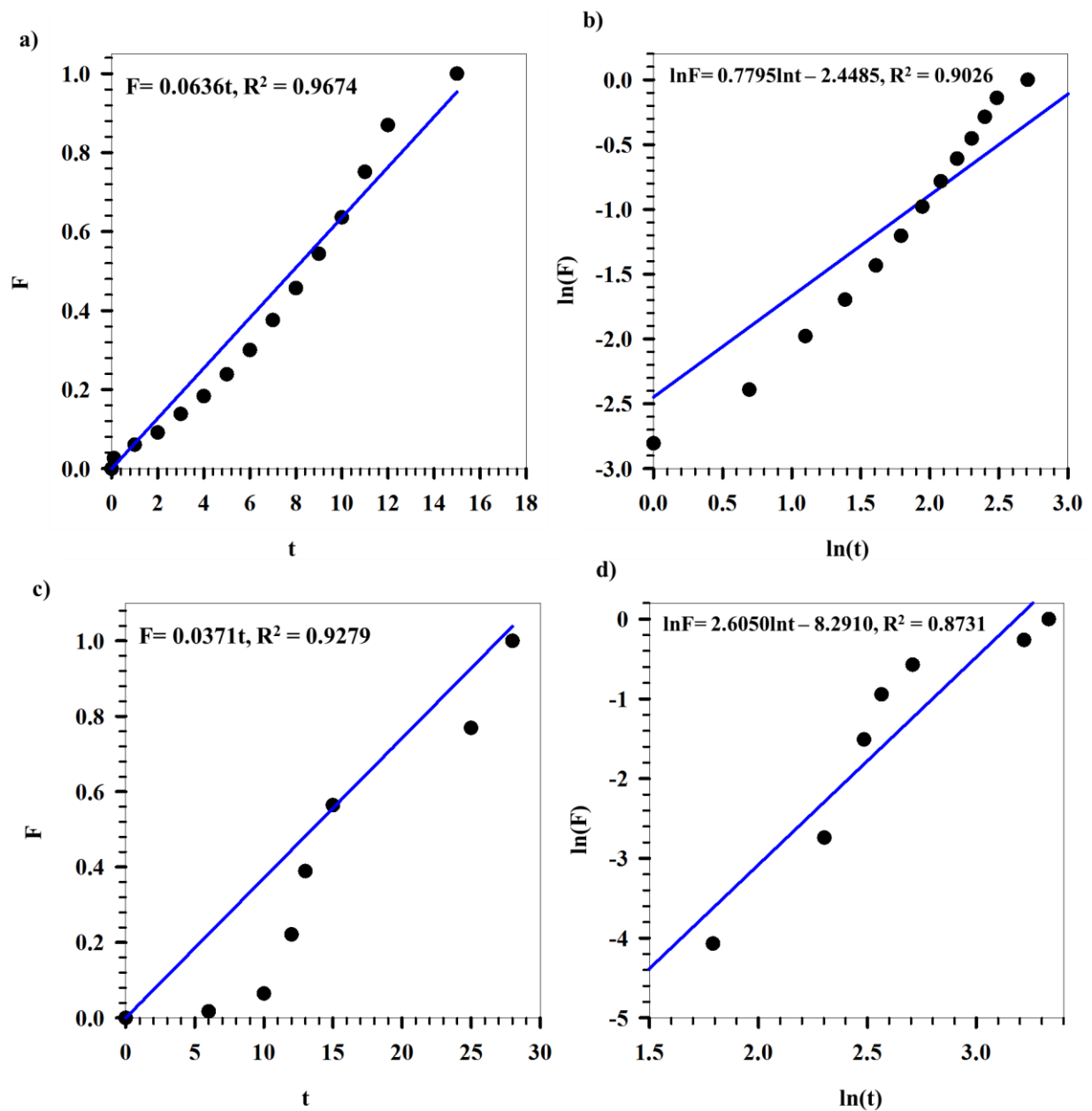
Figure 81 Release kinetics models for AuNR with 3.3 mg coated hydrogel. Zero order model a) part-I, c) part-II. Power law model b) part-I, d) part-II.

7. Results and Discussion
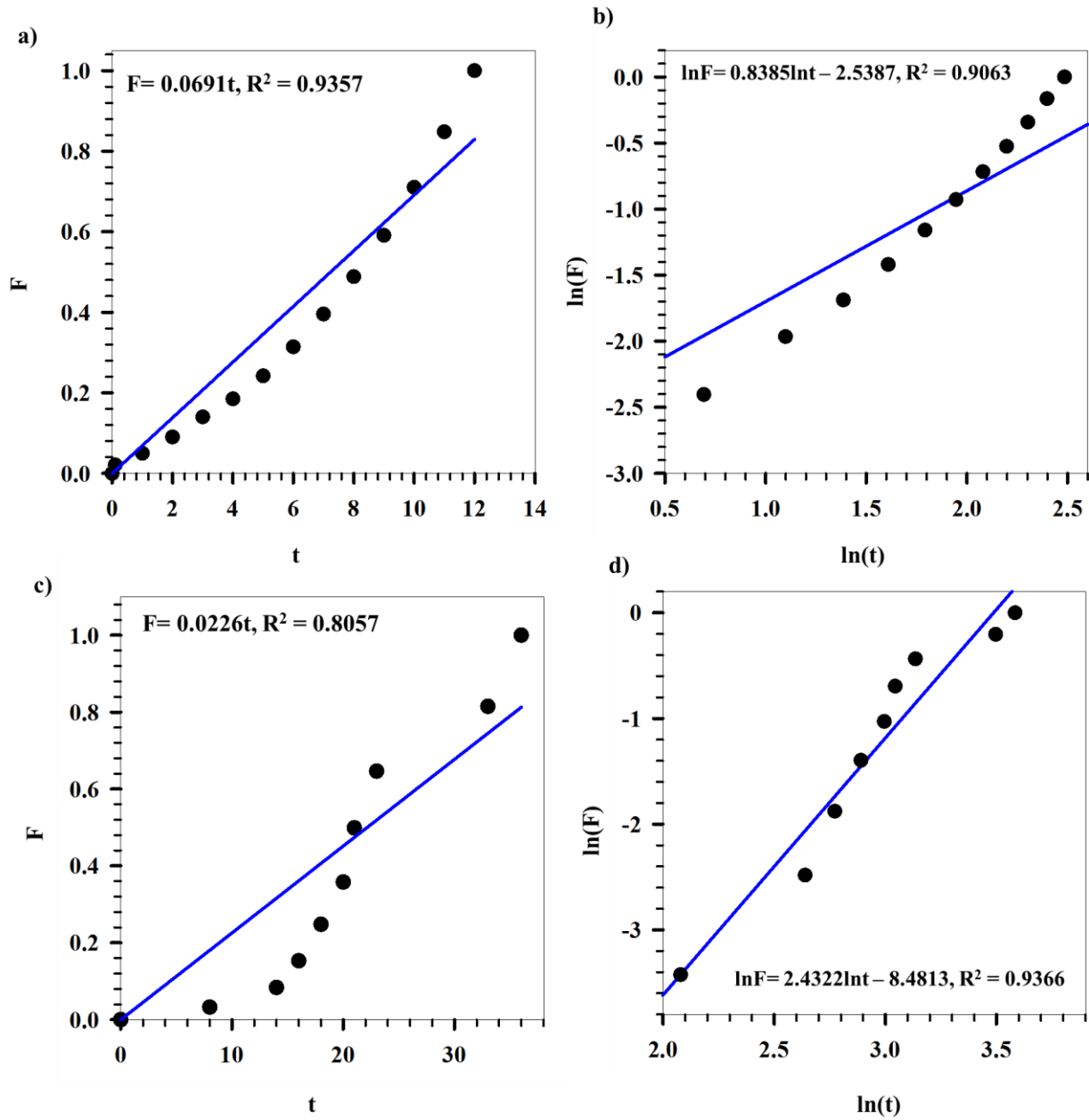
Figure 82 Release kinetics models for AuHex with 3.3 mg coated hydrogel. Zero order model a) part-I, c) part-II. Power law model b) part-I, d) part-II.

7. Results and Discussion

Figure 83 shows the fitted release models for AuBP coated with 3.3 mg C1. The release profile was divided into three sections at approximately 10 hours and at 23 hours from the start of release. For all cases, AuBP shows the best fit with zero order kinetic model with R^2 values of 0.9964, part-I (Figure 83 (a)), 0.9171, part-II (Figure 83 (c)), and 0.8918, part-III (Figure 83 (e)). The values of rate constants (k) for this system are 0.1139 hour^{-1}, 0.0892 hour^{-1} and 0.0429 hour$_{-1}$.

Figure 84 shows the fitted release models for AuNM coated with 3.3 mg C1. Similar to the case of AuBP, the release profile of AuNM was divided into three sections at approximately 10 hours and at 23 hours from the start of release. For all cases, AuNM shows the best fit with zero order kinetic model with R^2 values of 0.9934, part-I (Figure 84 (a)), 0.8706, part-II (Figure 84 (c)), and 0.8687, part-III (Figure 84 (e)). The values of rate constants (k) for this system are 0.1123 hour^{-1}, 0.0846 hour^{-1} and 0.0409 hour$_{-1}$.

Figure 85 shows the fitted release models for AuNS coated with 3.3 mg C1. The release profile was divided into two sections at approximately 12 hours and their release kinetics was studied separately. For both the cases, AuNS shows the best fit with zero order kinetic model with R^2 values of 0.9323, part-I (Figure 85 (a)) and 0.9102, part-II (Figure 85 (c)). The values of rate constants (k) for this system are 0.0697 hour^{-1} and 0.0265 hour^{-1}.
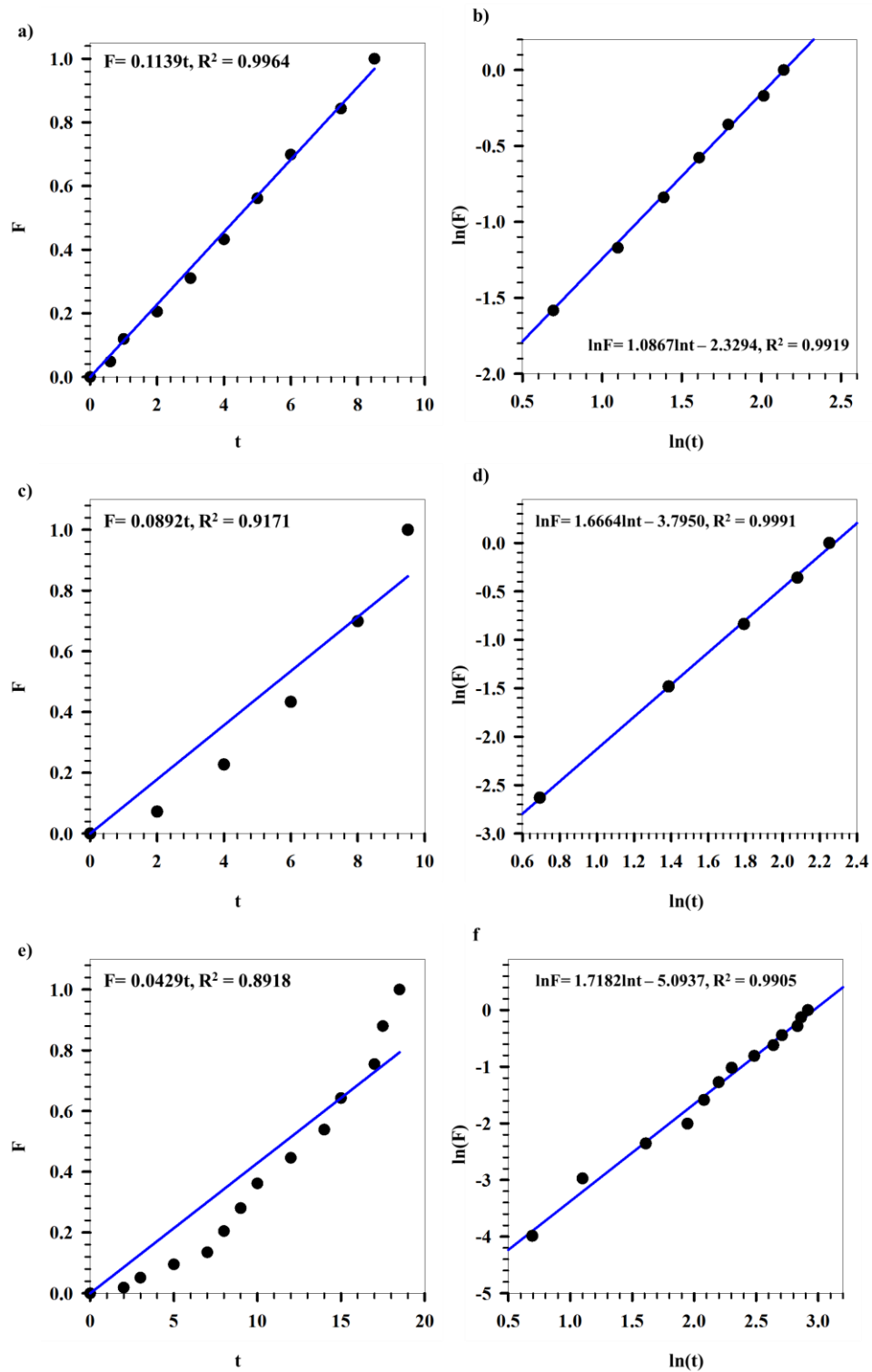
Figure 83 Release kinetics models for AuBP with 3.3 mg coated hydrogel. Zero order model a) part-I, c) part-II, e) part-III. Power law model b) part-I, d) part-II, f) part-III.
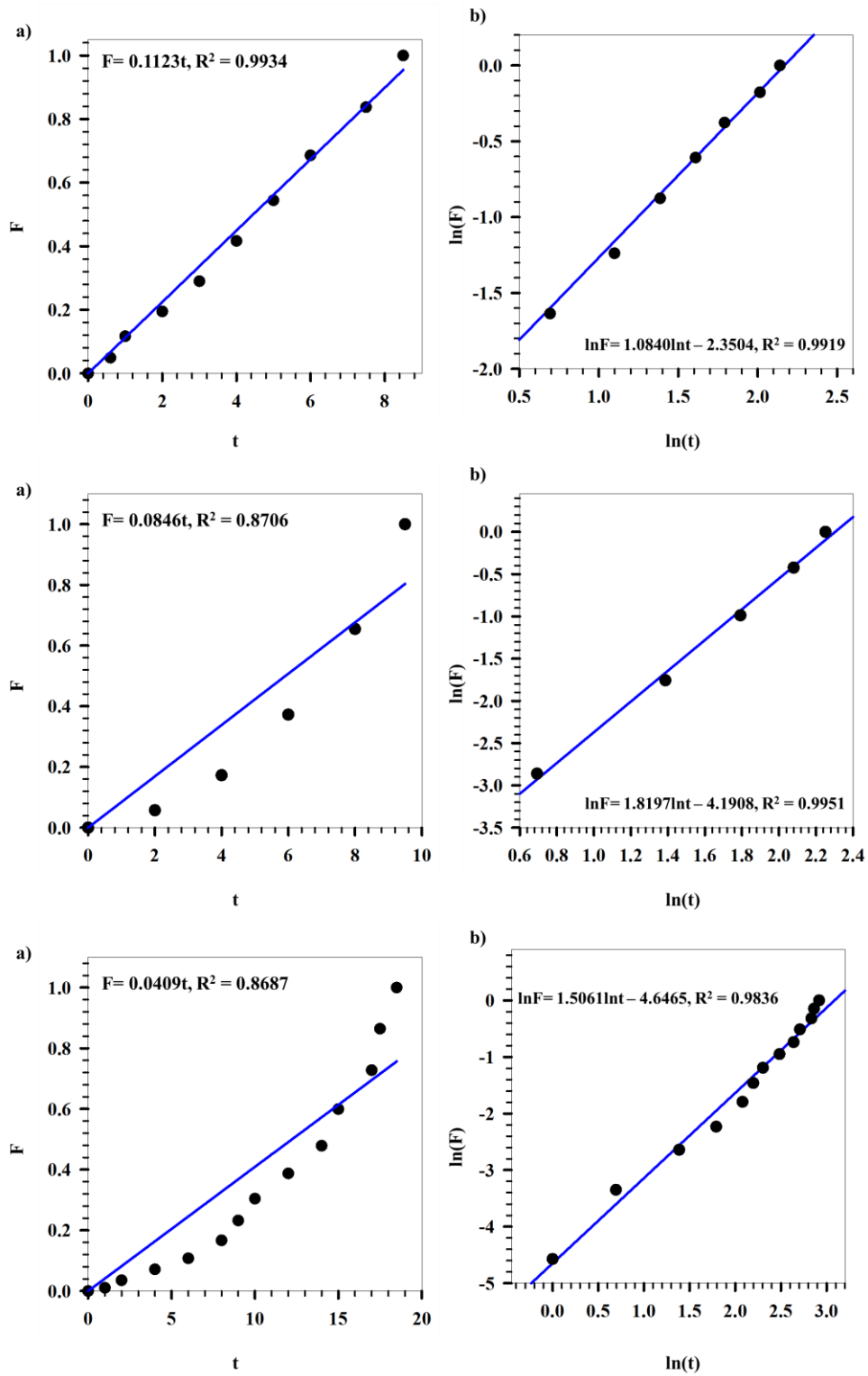
Figure 84 Release kinetics models for AuNM with 3.3 mg coated hydrogel. Zero order model a) part-I, c) part-II, e) part-III. Power law model b) part-I, d) part-II, f) part-III.
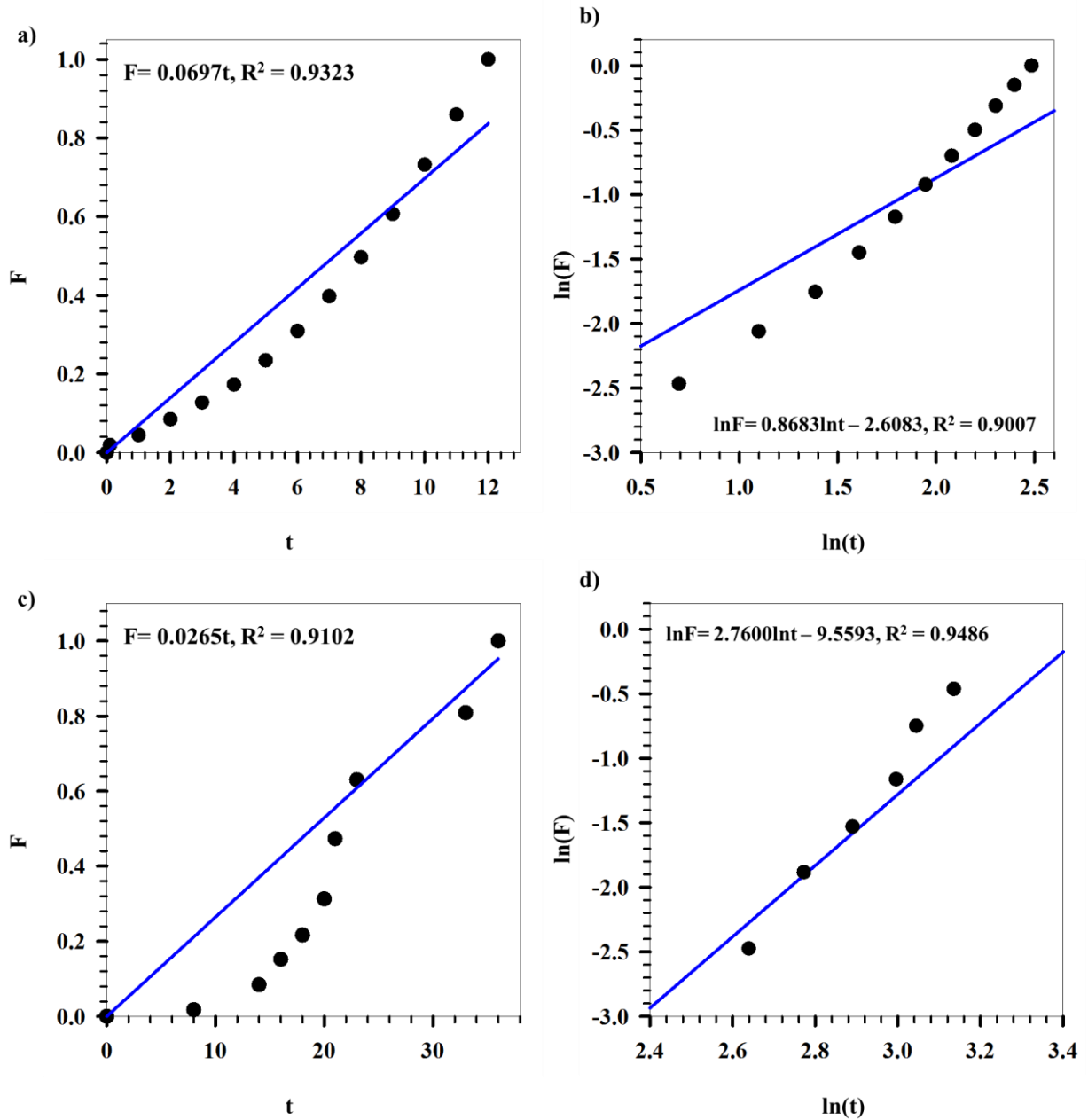
Figure 85 Release kinetics models for AuNS with 3.3 mg coated hydrogel. Zero order model a) part-I, c) part-II. Power law model b) part-I, d) part-II.

7. Results and Discussion

Table 9 summarises the values of release rate constants, release orders and the time for 50% drug release ($t_{1/2}$) for the different AuNPs coated with 3.3 mg hydrogel.

Table 9 Release rate constant, order and t1/2 for the 3.3 mg hydrogel coated AuNPs

Sample	Rate constant, k (hour^{-1})	Release order	$t_{1/2}$ (hours)
AuNR			
part-I	0.0636	Zero order	7.9
part-II	0.0371	Zero order	13.5
AuHex			
part-I	0.0691	Zero order	7.2
part-II	0.0226	Zero order	22.1
AuBP			
part-I	0.1139	Zero order	4.4
part-II	0.0892	Zero order	5.6
part-III	0.0429	Zero order	11.7
AuNM			
part-I	0.1123	Zero order	4.5
part-II	0.0864	Zero order	5.8
part-III	0.0409	Zero order	12.2
AuNS			
part-I	0.0697	Zero order	7.4
part-II	0.0265	Zero order	18.9

7. Results and Discussion

All the AuNPs coated with 3.3 mg hydrogel C1 follow zero order kinetics (Table 9). A decrease in the values of k for all AuNPs can be seen which infers decreasing release rate with increasing time. As the drug is released, the concentration gradient decreases resulting in reduced driving force for diffusion thereby slowing the release of the drug with passage of time. The $t_{1/2}$ values for all the AuNPs is lower in case of coating with 3.3 mg hydrogel than in the case of 1.67 mg hydrogel. This can be explained by the higher loading efficiencies of the AuNPs with 3.3 mg hydrogel, resulting in higher drug concentration in the hydrogel matrix thereby increasing the concentration gradient for faster diffusion across the hydrogel network.

The values of release exponent, geometry and transport mechanism have been summarised in Table 10. The release exponent is lower for all AuNPs at the start of the release and gradually increases as the release progresses. This might be explained that the drug has to initially travel from the hydrogel matrix to the interface of the hydrogel matrix and the solvent. Thus the initial diffusion rate of the drug is slower. But, as the release progresses and the hydrogel matrix collapses the regime changes from a spherical/cylindrical to a thin film thereby, reducing the diffusion path of the drug and the value of the release exponent (n) increases. In should be noted that even though 'n' increases, the release rate does not increase with time, but, maintains a constant release as seen from the release profiles in Figure 76 (b). this might be due to the fact that the amount of the drug inside the hydrogel matrix decreases over time, lowering the concentration gradient for the diffusion of Cyt C outside of the hydrogel network. Thus, the increase in the release exponent is counter balanced by the constant decreasing diffusion rate. Also, in case of higher hydrogel, the drug located at the periphery is release first. As the hydrogel collapses, the geometry changes from spherical to thin film increasing the value of release exponent.

7. Results and Discussion

Table 10 Release exponent and transport mechanisms shown by 3.3 mg hydrogel coated AuNPs.

Samples	Release exponent (n)	Geometry	Transport mechanism
AuNR			
part-I	0.7	Sphere or Cylinder	Anomalous
part-II	2.6	Thin Film	Super Case-II transport
AuHex			
part-I	0.8	Sphere or Cylinder	Anomalous
part-II	2.4	Thin Film	Super Case-II transport
AuBP			
part-I	1.1	Thin Film	Case-II transport
part-II	1.7	Thin Film	Super Case-II transport
part-III	1.7	Thin Film	Super Case-II transport
AuNM			
part-I	1.1	Thin Film	Case-II transport
part-II	1.8	Thin Film	Super Case-II transport
part-III	1.8	Thin Film	Super Case-II transport
AuNS			
part-I	0.8	Sphere or Cylinder	Anomalous
part-II	2.7	Thin Film	Super Case-II transport

8. Conclusion

The study shows that inorganic NPs can successfully be incorporated with thermo-responsive PEG-pNIPAM based hydrogels. The effect of variation of temperature and pH on the hydrogel was investigated by varying the temperature from 25^OC to 45^OC and pH from 9 to 3. The hydrogels showed a volumetric collapse on exposure to high temperatures and low pH attaining a volumetric collapse efficiency of 83.9%. VPTT of the hydrogels was calculated using a MATLAB$^©$ code by plotting the swelling ratio with temperature and equating the areas of swelling and collapsed fractions of the hydrogel. The VPTT was calculated to be 39.3 ± 0.6^OC.

Successful binding of the hydrogel to the inorganic Fe@Au and AuNPs have been confirmed using DLS, UV-vis and S(T)EM characterization techniques. Two kinds of incorporation; *in-situ* and coated were analysed. The Fe@Au_insitu NPs had a similar collapse behaviour (collapse efficiency, 94 %) to that of the hydrogels (collapse efficiency, 84%), and the Fe@Au_coated NPs' had swelling (swelling efficiency, 227%) behaviour similar to that of the bare Fe@Au NPs (swelling efficiency, 57%). Hydrogel, Fe@Au_insitu and Fe@Au_coated systems were loaded with Cyt C using breathing in mechanism, which gave high loading efficiencies of 96%, 86% and 78% respectively for the three systems. Cyt C release was carried out using dialysis under conditions of high temperature (45^OC) and acidic pH (3). Fe@Au_coated showed maximum release of 35% over time, compared to Fe@Au_insitu and bare hydrogels, showing maximum release of 12% and 13% respectively. This led to the incorporation of AuNPs in the hydrogel in subsequent study using the coating method.

After confirming the advantage of hydrogel coating on Fe@Au NPs on the loading and release properties, their effect on different shaped AuNPs were investigated. Five shapes namely, nanorods (AuNR), tetrahexahedral (AuHex), bipyramids (AuBP), nanomakura (AuNM) and nanospheres (AuNS), were synthesized using seed-mediated approach for anisotropic NPs and modified Turkevich for AuNS. Their characterization was conducted using DLS, zeta potential, UV-vis and S(T)EM. The S(T)EM images revealed AuBP as the largest structures having an aspect ratio (A.R.) 3.8 ± 0.5 with length 381.7 ± 106.8 nm and width 106.5 ± 45.3 nm. AuNS had the smallest size of 17.2 ± 2.2 nm followed by AuNR (A.R 3.4 ± 0.5, length 41.8 ± 4.1 nm, width 12.6

± 1.5 nm) < AuNM (A.R 1.5 ± 0.4, length 117.7 ± 14.8 nm, width 83.2 ± 13.6 nm) < AuHex (A.R 1.4 ± 0.2, length 232.6 ± 24.6 nm, width 170.7 ± 20.1 nm). These NPs were first coated with PEG followed by hydrogel C1. The association of PEG-hydrogel with the NPs was confirmed with the reduction on zeta potentials of anisotropic NPs owing to the replacement of cationic CTAB with anionic PEG. The shifts in the UV-vis peaks further validated PEG-hydrogel coating.

Finally, PEG-hydrogel coated AuNPs were loaded with Cyt C using breathing in method. The effect of the hydrogel amount on drug loading and release was studied using 1.67 mg and 3.3 mg of hydrogel for coating of the NPs. A higher loading efficiency (~70-80%) was observed for all the samples with increased hydrogel content. Cyt C was released under conditions of high temperature (45^OC) and acidic pH (3). A greater release was seen with higher hydrogel content due to the increase in the diffusion driving force resulting from higher drug concentration gradient inside and outside of the hydrogel matrix.

Zero order, first order, Higuchi and power law models were fitted to the release data in order to investigate the release mechanism from these AuNPs. The AuNPs followed a zero order kinetics with 1.67 mg and 3.3 mg hydrogel coating. The release in the prior case showed progressive decline with the passage of time due to the decrease in the diffusion driving force with the release of Cyt C. In case of 1.67 mg hydrogel, the coating is thinner resulting in faster collapse of the hydrogel. Thus, the release takes up the thin film conformation. In the case of higher hydrogel concentration, the release system takes up spherical/cylindrical geometry for AuNR, AuHex and AuNS, due to a thicker layer of the coated hydrogel, which later switches to thin film as the hydrogel collapses with time.

Thus, the swelling collapse behaviour of the which is used for efficient targeted drug deliver, can be combined with the imaging property of AuNPs, resulting from LSPR, to form hybrid NPs for theranostic applications.

9. Future scope

Coating of thermo-responsive pNIPAM on isotropic and anisotropic nanostructures, has been successfully shown within the scope of this thesis work, having good loading and release properties. Extensive studies can be performed by examining the variation of PEG-hydrogel coating with different sizes of the same NP shape.

The size and zeta potential behaviour of AuNPs was examined using DLS. However, as already stated the validity of the DLS measurements should be cross-examined using other characterization techniques like S(T)EM, analysing the changes in size of the sample at different conditions of temperature and pH.

Having shown that AuNPs have good loading and release properties using Cyt C, the study can be extended to investigate the effect of drug concentration as well as analysing the loading and release capacities of these systems with other commercially used potential drugs such as L-Dopa and Coumarin.

The study showed the incorporation of Fe@Au NPs in the hydrogel matrix using in-situ and coating methods, indicating that the Fe@Au_insitu system resembled that of the hydrogel and the Fe@Au_coated to that of the bare Fe@Au NPs. An approach was provided as to how the Fe@Au NPs are incorporated in the hydrogel matrix but, additional analysis can be conducted using S(T)EM. Similarly, the incorporation of Cyt C in the hydrogel matrix can also be examined using techniques like Fourier Transform Infrared Spectroscopy (FTIR).

Appendices

Appendix A

Loading and Encapsulation Calculations

The loading studies were performed by measuring the absorbance of the systems using Uv-vis. The absorbance peak of nascent Cyt C was noted at a wavelength of 409 nm (A_{CytC}). Another reading was taken after loading of Cyt C on the hydrogel or coated NP systems (A_{loaded}). A final measurement was conducted after dialysis of the loaded sample ($A_{dialysis}$). The dialysis ensured removal of free Cyt C from the system under analysis.

The L.E. was calculated as follows:

$$L.E. = \left(\frac{A_{dialysis}}{A_{Cyt\,C}} \right) X\ 100\%$$

The E.E. was calculated as:

$$E.E. = \left(\frac{L.E.\%\ X\ mass\ of\ drug\ (\mu g)}{mass\ of\ nanocarrier\ system\ (mg)} \right) \quad [\mu g/mg]$$

A sample has been demonstrated by the following example using Fe@Au_insitu NPs as shown by Figure 86.

$A_{Cyt\,C} = 1.80443$
$A_{loaded} = 1.95349$
$A_{dialysis} = 1.55685$

$$L.E. = \left(\frac{1.55685}{1.80443} \right) X\ 100\%$$

$$L.E. = 86.3\ \%$$

Mass of drug loaded = 3 mg
Mass of Fe@Au_insitu = 3.3 mg

$$E.E. = \left(\frac{86.3 \; X \; 3}{100 \; X \; 3.3 \; X \; 1000} \right)$$

$$E.E. = 784.4 \; \mu g/mg$$
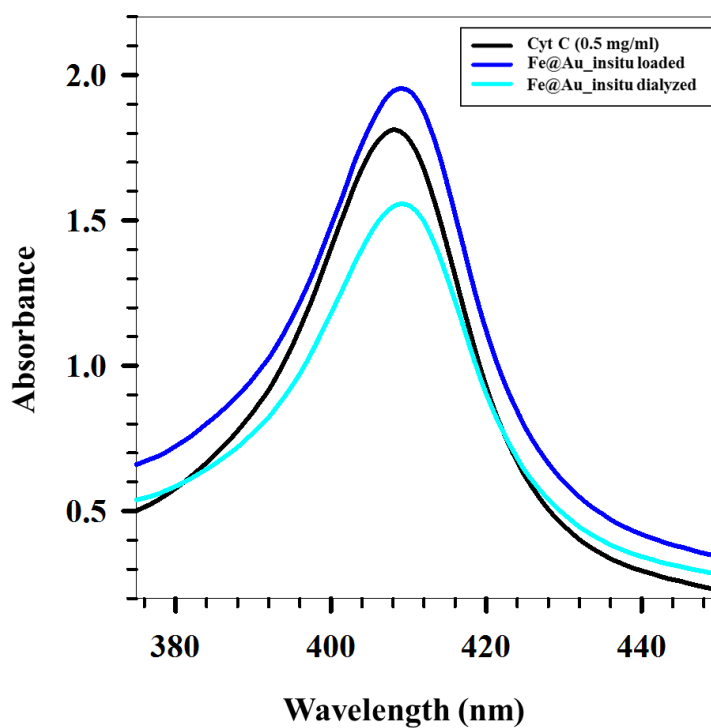
Figure 86 Uv-vis conducted for Fe@Au_insitu for calculating L.E.

Appendices

Appendix B

Uv-vis Release Profiles and Kinetics

The release percentage of Cyt C from the hydrogel based systems was calculated as follows:

$$(\%)\ Drug\ Release = \left(\frac{Absorbance\ at\ time\ (t_o) - Absorbance\ at\ the\ time\ (t)}{Absorbance\ at\ time\ (t_o)}\right) X\ 100$$

Where,
t_o = Initial time of at the start of release
t = Time at the point of measurement

The mass of drug released in time t is calculated as follows:

$$M_d = [(\%)\ Drug\ Release]\ X\ L.E.X\ \left(\frac{Drug\ concentration\ (mg/ml)}{100}\right)$$

$$M_t = \sum_{0}^{t} M_{d,t}$$

Where, M_t represents the cumulative mass of the drug released from $t = 0$ to the time of the current reading.

Fraction of the drug released in time t is calculated as:

$$F = \frac{M_t}{M_\infty}$$

Where, M_∞ is the mass of the drug released at t final.

Appendices

A sample calculation has been shown using the release profile and kinetics data for Fe@Au_coated system. Figure 87 shows the decrease in absorbance peaks with Cyt C release with time using Uv-vis. The value of absorbance is noted at the start of release (t_0). The following calculation is shown 10 hours after commencement of release of Cyt C from Fe@Au_coated NPs.
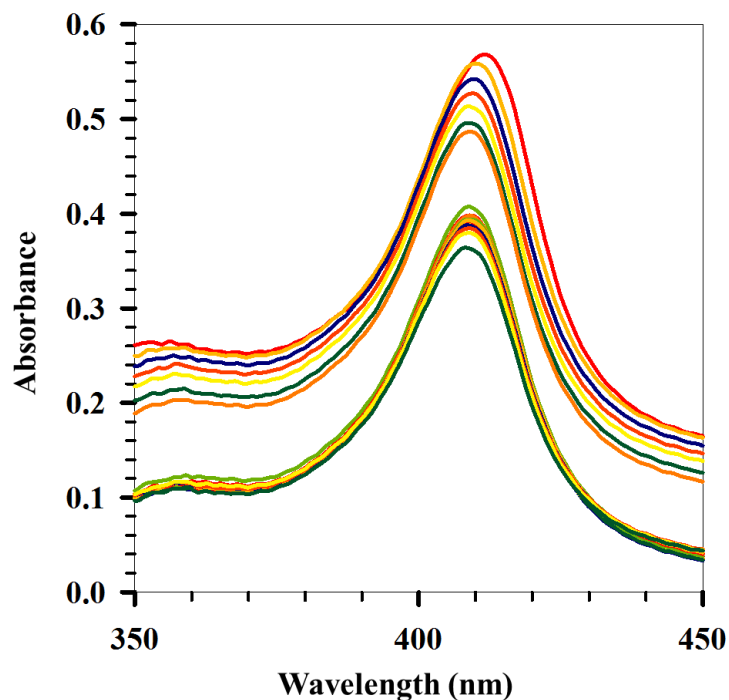
Figure 87 Release profile of Fe@Au_coated NPs loaded with Cyt C using Uv-vis.

The calculations, at t = 10 hours, are as follows:

Absorbance at t_o = 0.55743
Absorbance at t_{10} = 0.3918
M_∞ = 0.41 mg
L.E. of Fe@Au_coated system = 78%
Concentration of Cyt C = 0.1 mg/ml

$$\% \, Drug \, release = \left[\frac{0.55743 - 0.3918}{0.55743}\right] X \, 100$$

$$\% \, Drug \, release = 29.71 \, \%$$

Mass of drug released after 10 hours:

$$M_d = \frac{29.71 \, X \, 78 \, X \, 0.1}{100 \, X 100} = 0.023 \, mg$$

Cumulative mass released in 10 hours:

$$M_{10} = 0.14 \, mg$$

Fraction of mass released:

$$F = \frac{0.14}{0.41} = 0.35$$

Appendices

Table 11 provides the values of various parameters used to determine the release kinetics for Fe@Au_coated system.

Table 11 Release kinetics data for Fe@Au_coated systems.

t	% Release	Mass released (mg)	Mt (mg)	F	ln(1-F)	t^0.5	ln(F)	ln(t)
0.00	0.00	0.00	0.00	0.00	0.00	0.00		
0.50	0.08	0.00	0.00	0.00	0.00	0.71	-8.77	-0.69
1.00	2.87	0.00	0.00	0.01	-0.01	1.00	-5.17	0.00
2.00	5.50	0.00	0.01	0.02	-0.02	1.41	-4.12	0.69
3.00	7.93	0.01	0.01	0.03	-0.03	1.73	-3.46	1.10
4.00	11.08	0.01	0.02	0.05	-0.05	2.00	-2.94	1.39
5.00	12.67	0.01	0.03	0.08	-0.08	2.24	-2.56	1.61
6.00	26.93	0.02	0.05	0.13	-0.14	2.45	-2.05	1.79
7.00	28.56	0.02	0.07	0.18	-0.20	2.65	-1.70	1.95
8.00	28.79	0.02	0.10	0.24	-0.27	2.83	-1.43	2.08
9.00	29.64	0.02	0.12	0.30	-0.35	3.00	-1.22	2.20
10.00	29.71	0.02	0.14	0.35	-0.44	3.16	-1.04	2.30
11.00	29.80	0.02	0.17	0.41	-0.53	3.32	-0.89	2.40
13.00	29.59	0.02	0.19	0.47	-0.63	3.61	-0.76	2.56
15.00	28.57	0.02	0.21	0.52	-0.74	3.87	-0.65	2.71
17.00	29.31	0.02	0.23	0.58	-0.86	4.12	-0.55	2.83
19.00	29.64	0.02	0.26	0.63	-1.01	4.36	-0.45	2.94
21.00	29.49	0.02	0.28	0.69	-1.18	4.58	-0.37	3.04
25.00	30.41	0.02	0.30	0.75	-1.39	5.00	-0.29	3.22
29.00	31.00	0.02	0.33	0.81	-1.66	5.39	-0.21	3.37
33.00	31.88	0.02	0.35	0.87	-2.04	5.74	-0.14	3.50
37.00	32.70	0.03	0.38	0.93	-2.71	6.08	-0.07	3.61
51.00	34.70	0.03	0.41	1.00		7.14	0.00	3.93

Appendix C

Release Kinetics Models for AuNPs with 1.67 mg hydrogel coating

a)
$\ln(1-F) = -0.0531t, R^2 = 0.8732$

b)
$F = 0.1311\sqrt{t}, R^2 = 0.7166$

c)
$\ln(1-F) = -0.0585t, R^2 = 0.8990$

d)
$F = 0.1683\sqrt{t}, R^2 = 0.8459$

e)
$\ln(1-F) = -0.0332t, R^2 = 0.8971$

f)
$F = 0.1028\sqrt{t}, R^2 = 0.8437$
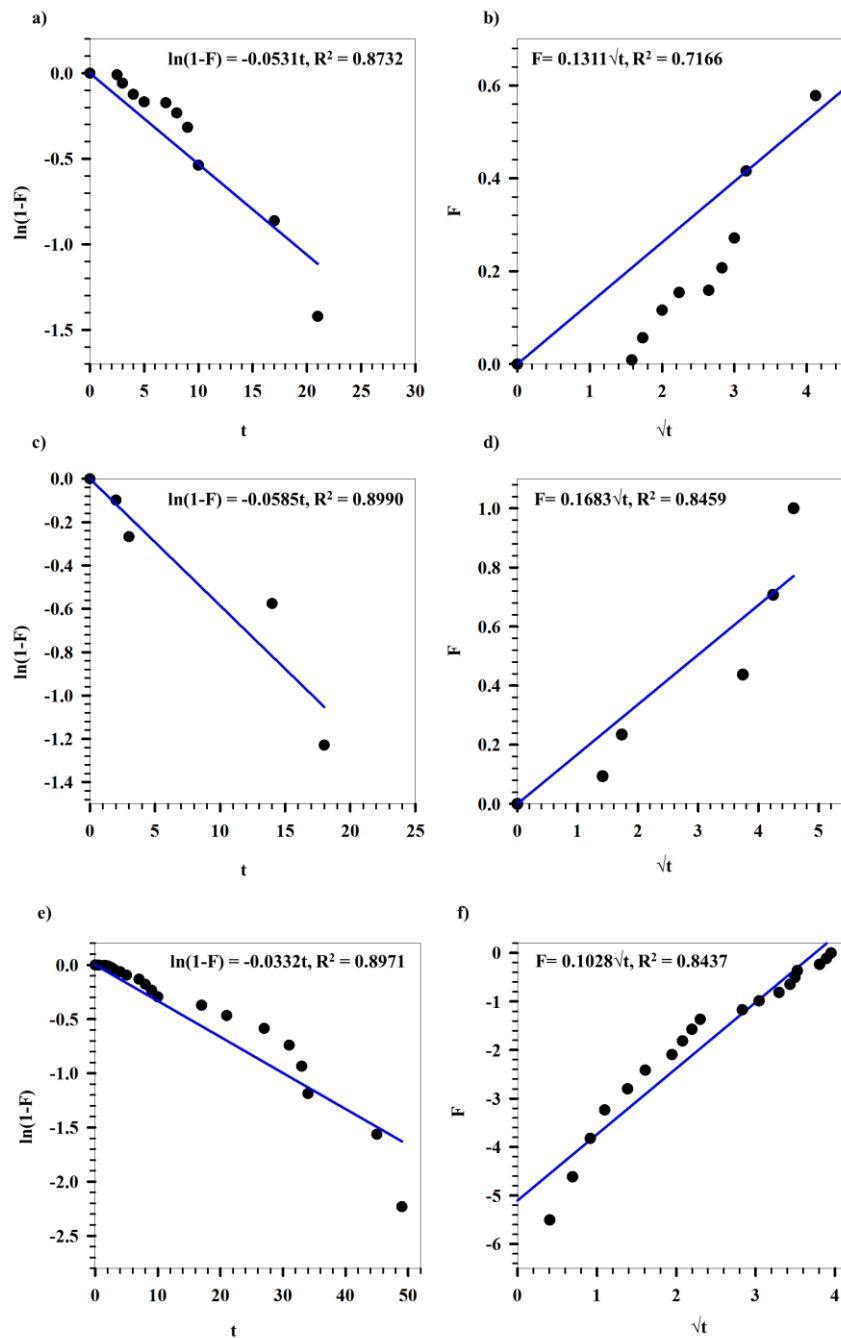
Figure 88 Release kinetic model for 1.67 mg hydrogel coated AuNPs. First order model, a) AuNR part-I, c) AuNR part-II, e) AuHex. Higuchi model b) AuNR part-I, d) AuNR part-II, f) AuHex.
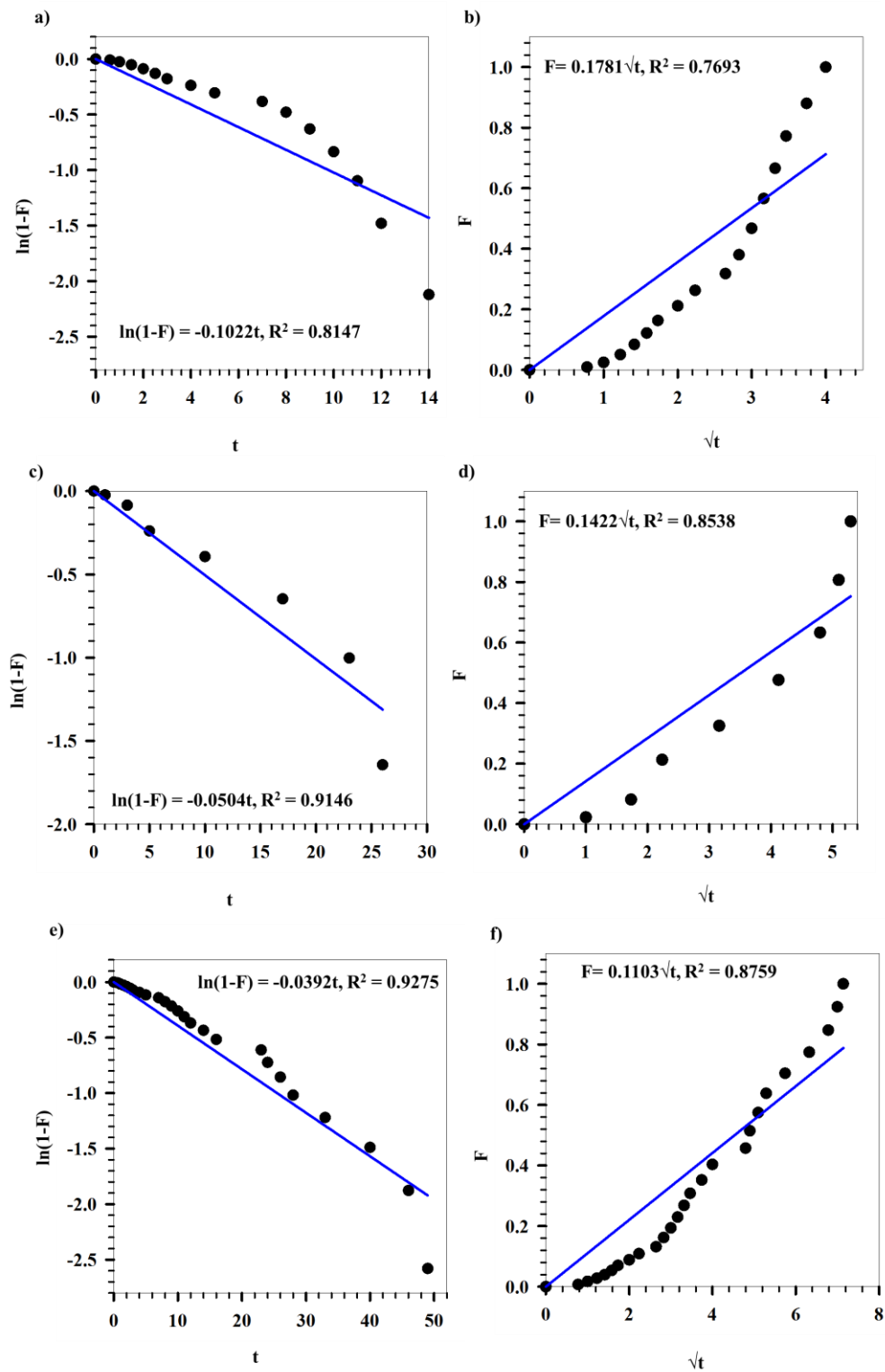
Figure 89 Release kinetic model for 1.67 mg hydrogel coated AuNPs. First order model, a) AuBP part-I, c) AuBP part-II, e) AuNM. Higuchi model b) AuBP part-I, d) AuBP part-II, f) AuNM.

a)

b)

$\ln(1-F) = -0.0314t$, $R^2 = 0.8602$

$F = 0.0989\sqrt{t}$, $R^2 = 0.7901$
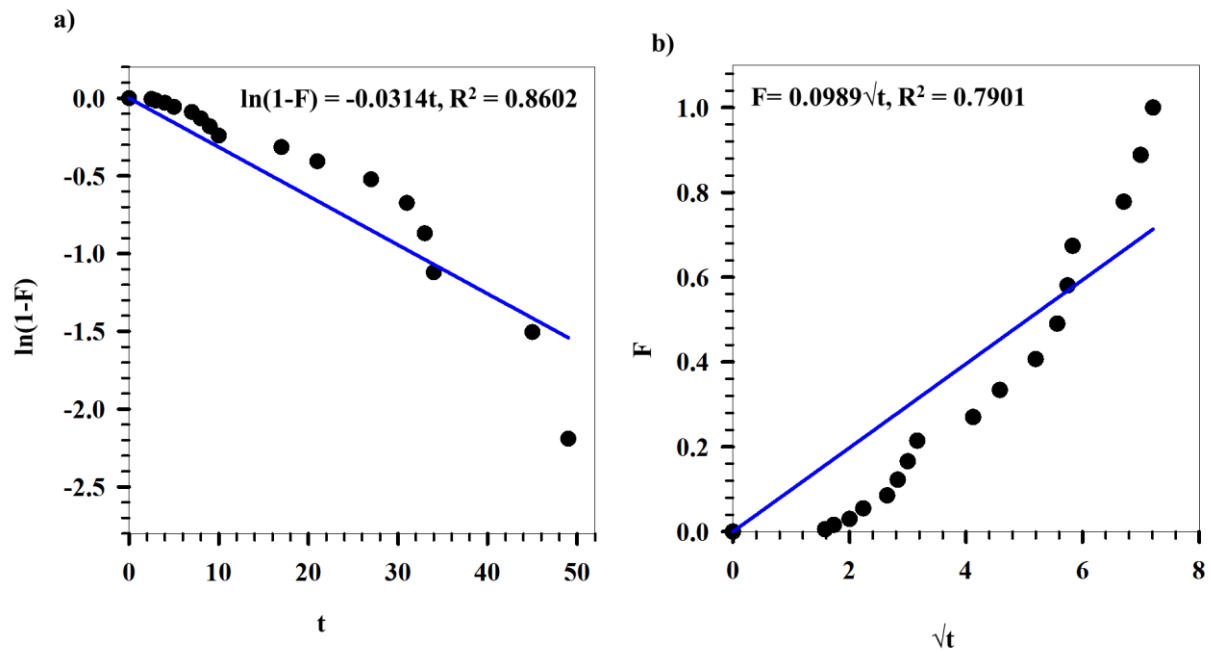
Figure 90 Release kinetic model for 1.67 mg hydrogel coated AuNS. a) First order model. b) Higuchi model

Release Kinetics Models for AuNPs with 3.3 mg hydrogel coating
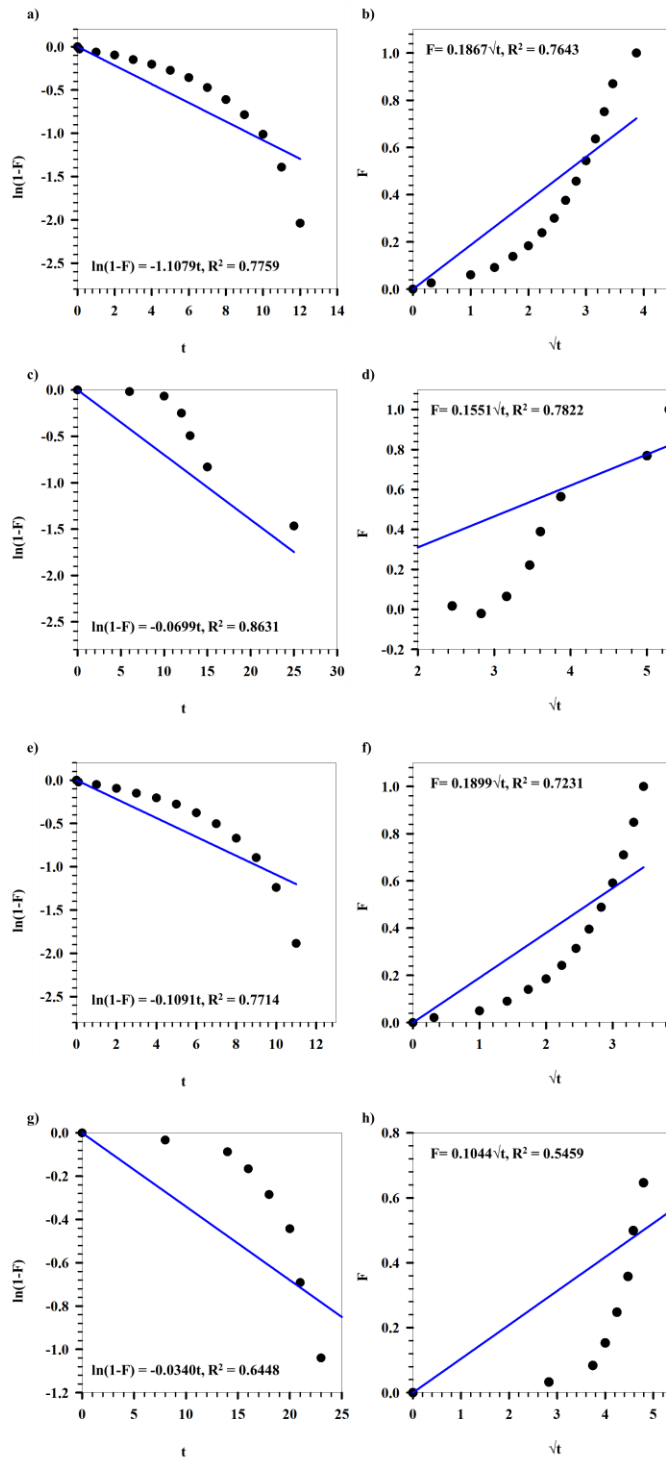
Figure 91 Release kinetic model for 3.3 mg hydrogel coated AuNPs. First order model, a) AuNR part-I, c) AuNR part-II, e) AuHex part-I, g) AuHex part-II. Higuchi model b) AuNR part-I, d) AuNR part-II, f) AuHex part-I, g) AuHex part-II.
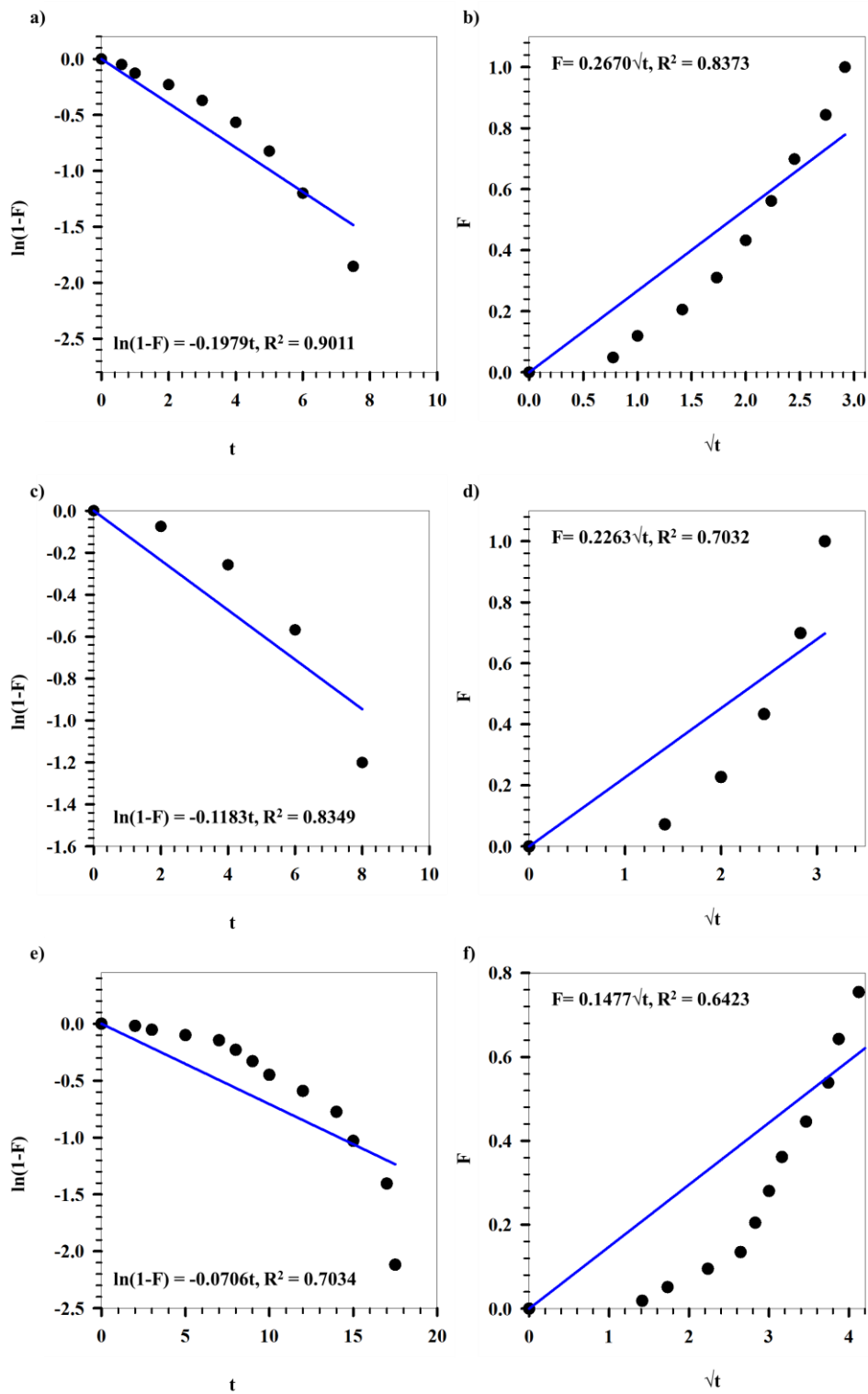
Figure 92 Release kinetic model for 3.3 mg hydrogel coated AuBP. First order model, a) AuBP part-I, c) AuBP part-II, e) AuBP part-III. Higuchi model b) AuBP part-I, d) AuBP part-II, f) AuBP part-III.
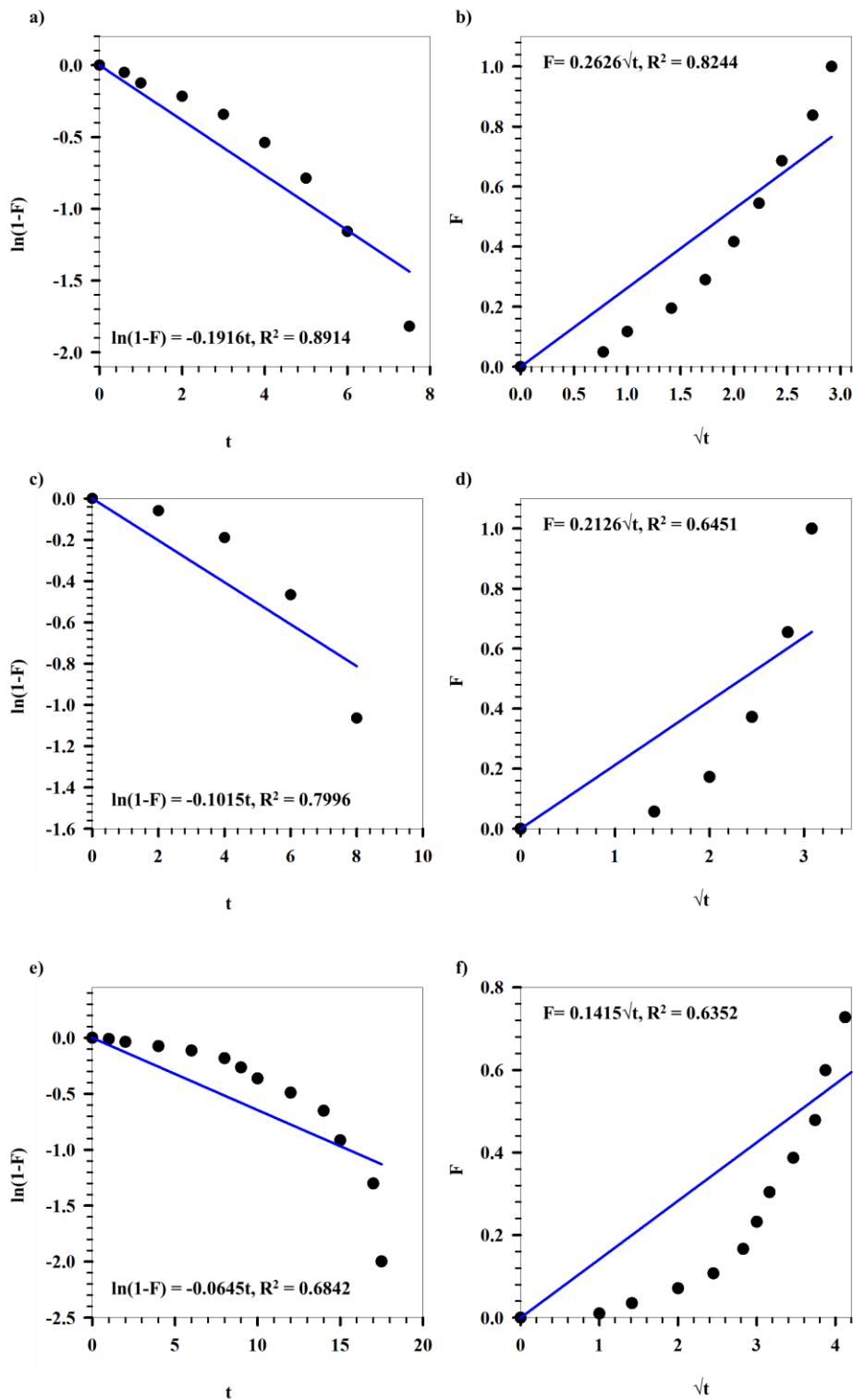
Figure 93 Release kinetic model for 3.3 mg hydrogel coated AuNM. First order model, a) AuNM part-I, c) AuNM part-II, e) AuNM part-III. Higuchi model b) AuNM part-I, d) AuNM part-II, f) AuNM part-III.
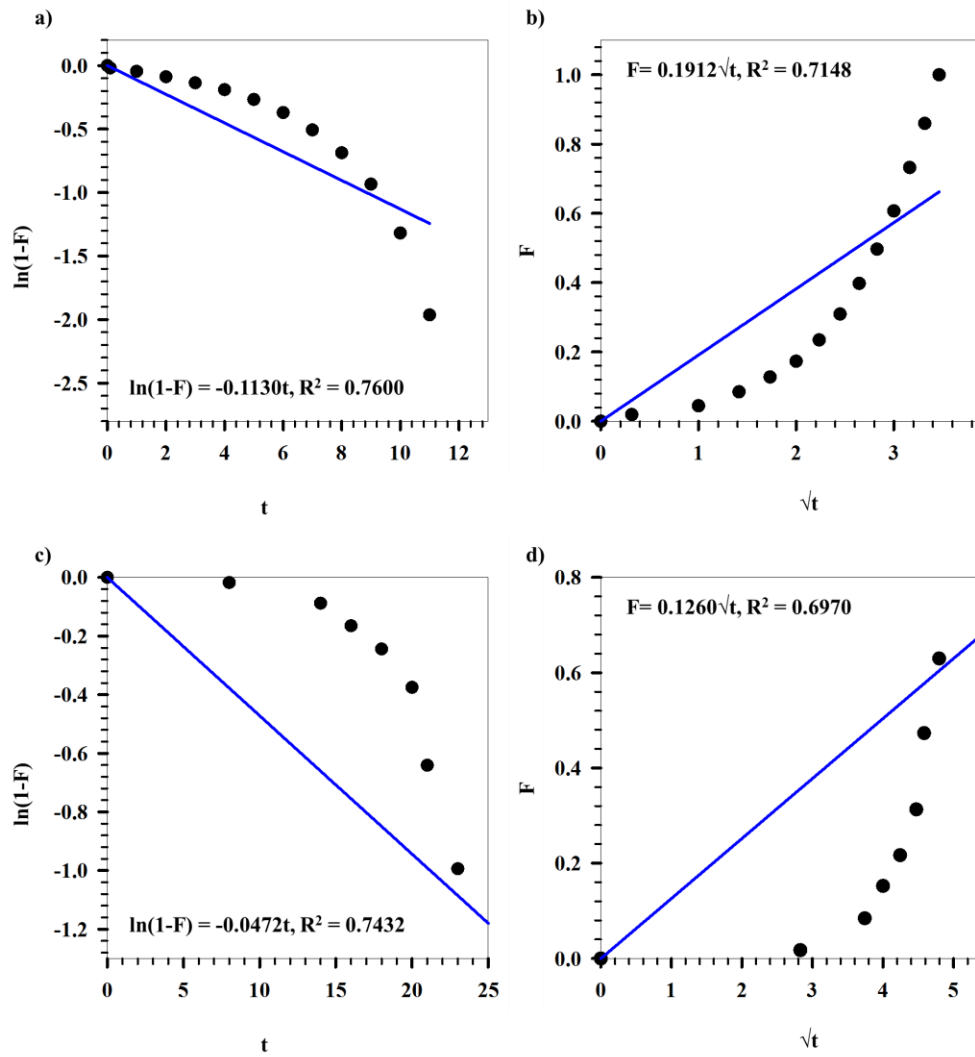
Figure 94 Release kinetic model for 3.3 mg hydrogel coated AuNS. First order model, a) AuNS part-I, c) AuNS part-II. Higuchi model b) AuNS part-I, d) AuNS part-II.

References

1.   Silva, G.A., *Introduction to nanotechnology and its applications to medicine.* Surg Neurol, 2004. **61**(3): p. 216-20.

2.   Ragusa, A., I. GarcÍa, and S. PenadÉs, *Nanoparticles as nonviral gene delivery vectors.* IEEE transactions on nanobioscience, 2007. **6**(4): p. 319-330.

3.   Månsson, S., et al., *13C imaging—a new diagnostic platform.* European radiology, 2006. **16**(1): p. 57-67.

4.   Astruc, D., F. Lu, and J.R. Aranzaes, *Nanoparticles as recyclable catalysts: the frontier between homogeneous and heterogeneous catalysis.* Angewandte Chemie International Edition, 2005. **44**(48): p. 7852-7872.

5.   Murty, B., et al., *Applications of nanomaterials*, in *Textbook of Nanoscience and Nanotechnology*. 2013, Springer. p. 107-148.

6.   Parveen, S., R. Misra, and S.K. Sahoo, *Nanoparticles: a boon to drug delivery, therapeutics, diagnostics and imaging.* Nanomedicine, 2012. **8**(2): p. 147-66.

7.   Roco, M.C., *Nanotechnology: convergence with modern biology and medicine.* Curr Opin Biotechnol, 2003. **14**(3): p. 337-46.

8.   Allen, T.M. and P.R. Cullis, *Drug delivery systems: entering the mainstream.* Science, 2004. **303**(5665): p. 1818-1822.

9.   Wu, W. and S. Zhou, *Responsive Polymer-Inorganic Hybrid Nanogels for Optical Sensing, Imaging, and Drug Delivery.* Nanomaterials in Drug Delivery, Imaging, and Tissue Engineering, 2013: p. 269-319.

10.   Haug, H. and S.W. Koch, *Quantum theory of the optical and electronic properties of semiconductors*. Vol. 5. 2004: World Scientific.

11.   Giljohann, D.A., et al., *Gold nanoparticles for biology and medicine.* Angew Chem Int Ed Engl, 2010. **49**(19): p. 3280-94.

12.   Yeh, Y.C., B. Creran, and V.M. Rotello, *Gold nanoparticles: preparation, properties, and applications in bionanotechnology.* Nanoscale, 2012. **4**(6): p. 1871-80.

13.   Rosi, N.L., et al., *Oligonucleotide-modified gold nanoparticles for intracellular gene regulation.* Science, 2006. **312**(5776): p. 1027-30.

14.   Mukherjee, P., et al., *Potential therapeutic application of gold nanoparticles in B-chronic lymphocytic leukemia (BCLL): enhancing apoptosis.* J Nanobiotechnology, 2007. **5**: p. 4.

15.   Calzolai, L., et al., *Protein--nanoparticle interaction: identification of the ubiquitin--gold nanoparticle interaction site.* Nano Lett, 2010. **10**(8): p. 3101-5.

16.   McBain, S.C., H.H. Yiu, and J. Dobson, *Magnetic nanoparticles for gene and drug delivery.* Int J Nanomedicine, 2008. **3**(2): p. 169-80.

References

17.   Gupta, A.K. and M. Gupta, *Synthesis and surface engineering of iron oxide nanoparticles for biomedical applications.* Biomaterials, 2005. **26**(18): p. 3995-4021.

18.   Dilnawaz, F., et al., *Dual drug loaded superparamagnetic iron oxide nanoparticles for targeted cancer therapy.* Biomaterials, 2010. **31**(13): p. 3694-706.

19.   Ghorbani, M., et al., *Ternary-responsive magnetic nanocarriers for targeted delivery of thiol-containing anticancer drugs.* New Journal of Chemistry, 2016. **40**(4): p. 3561-3570.

20.   Gupta, A.K. and M. Gupta, *Cytotoxicity suppression and cellular uptake enhancement of surface modified magnetic nanoparticles.* Biomaterials, 2005. **26**(13): p. 1565-73.

21.   Anglin, E.J., et al., *Porous silicon in drug delivery devices and materials.* Adv Drug Deliv Rev, 2008. **60**(11): p. 1266-77.

22.   Shi, S., F. Chen, and W. Cai, *Biomedical applications of functionalized hollow mesoporous silica nanoparticles: focusing on molecular imaging.* Nanomedicine (Lond), 2013. **8**(12): p. 2027-39.

23.   Kumar, R., et al., *In vivo biodistribution and clearance studies using multimodal organically modified silica nanoparticles.* ACS Nano, 2010. **4**(2): p. 699-708.

24.   Rampazzo, E., et al., *Proper design of silica nanoparticles combines high brightness, lack of cytotoxicity and efficient cell endocytosis.* Nanoscale, 2013. **5**(17): p. 7897-905.

25.   Xue, M., et al., *pH-Operated mechanized porous silicon nanoparticles.* J Am Chem Soc, 2011. **133**(23): p. 8798-801.

26.   Ikoba, U., et al., *Nanocarriers in therapy of infectious and inflammatory diseases.* Nanoscale, 2015. **7**(10): p. 4291-305.

27.   Yuan, X., et al., *Highly luminescent silver nanoclusters with tunable emissions: cyclic reduction–decomposition synthesis and antimicrobial properties.* NPG Asia Materials, 2013. **5**(2): p. e39.

28.   Sahoo, S.K., W. Ma, and V. Labhasetwar, *Efficacy of transferrin-conjugated paclitaxel-loaded nanoparticles in a murine model of prostate cancer.* Int J Cancer, 2004. **112**(2): p. 335-40.

29.   Tromsø, U.i. *Drug Delivery Systems*. [cited 2016 21, July].

30.   Cevc, G., *Rational design of new product candidates: the next generation of highly deformable bilayer vesicles for noninvasive, targeted therapy.* Journal of controlled release, 2012. **160**(2): p. 135-146.

31.   Zara, G.P., et al., *Intravenous administration to rabbits of non-stealth and stealth doxorubicin-loaded solid lipid nanoparticles at increasing concentrations of stealth agent: pharmacokinetics and distribution of doxorubicin in brain and other tissues.* J Drug Target, 2002. **10**(4): p. 327-35.

32.   Owens, D.E., 3rd and N.A. Peppas, *Opsonization, biodistribution, and pharmacokinetics of polymeric nanoparticles.* Int J Pharm, 2006. **307**(1): p. 93-102.

References

33. Torchilin, V.P., *Targeted polymeric micelles for delivery of poorly soluble drugs.* Cell Mol Life Sci, 2004. **61**(19-20): p. 2549-59.

34. Torchilin, V.P., et al., *New synthetic amphiphilic polymers for steric protection of liposomes in vivo.* J Pharm Sci, 1995. **84**(9): p. 1049-53.

35. Turnbull, W.B. and J.F. Stoddart, *Design and synthesis of glycodendrimers.* J Biotechnol, 2002. **90**(3-4): p. 231-55.

36. Li, Y., et al., *Controlled assembly of dendrimer-like DNA.* Nat Mater, 2004. **3**(1): p. 38-42.

37. Huang, B., *Development of PETAA Dendrimers: Better, Faster, Cleaner.*, in *MNIMBS Endowment*. Michigan Nanotechnology Institute for Medical and Biological Sciences: Michigan

38. Langer, R. and N.A. Peppas, *Advances in biomaterials, drug delivery, and bionanotechnology.* AIChE Journal, 2003. **49**(12): p. 2990-3006.

39. Peppas, N.A., et al., *Hydrogels in biology and medicine: from molecular principles to bionanotechnology.* Advanced Materials, 2006. **18**(11): p. 1345-1360.

40. Das, N., *Preparation methods and properties of hydrogel: a review.* Int J Pharm Pharm Sci, 2013. **5**: p. 112-7.

41. Akhter, S., et al., *Gold nanoparticles in theranostic oncology: current state-of-the-art.* Expert Opin Drug Deliv, 2012. **9**(10): p. 1225-43.

42. Yeh, Y.-C., B. Creran, and V.M. Rotello, *Gold nanoparticles: preparation, properties, and applications in bionanotechnology.* Nanoscale, 2012. **4**(6): p. 1871-1880.

43. Petryayeva, E. and U.J. Krull, *Localized surface plasmon resonance: nanostructures, bioassays and biosensing--a review.* Anal Chim Acta, 2011. **706**(1): p. 8-24.

44. Sarina, S., E.R. Waclawik, and H. Zhu, *Photocatalysis on supported gold and silver nanoparticles under ultraviolet and visible light irradiation.* Green Chemistry, 2013. **15**(7): p. 1814-1833.

45. Boisselier, E. and D. Astruc, *Gold nanoparticles in nanomedicine: preparations, imaging, diagnostics, therapies and toxicity.* Chem Soc Rev, 2009. **38**(6): p. 1759-82.

46. Huang, X., et al., *Cancer cell imaging and photothermal therapy in the near-infrared region by using gold nanorods.* J Am Chem Soc, 2006. **128**(6): p. 2115-20.

47. Nagesha, D., et al., *In vitro imaging of embryonic stem cells using multiphoton luminescence of gold nanoparticles.* Int J Nanomedicine, 2007. **2**(4): p. 813-9.

48. Kneipp, K., H. Kneipp, and J. Kneipp, *Surface-enhanced Raman scattering in local optical fields of silver and gold nanoaggregates-from single-molecule Raman spectroscopy to ultrasensitive probing in live cells.* Acc Chem Res, 2006. **39**(7): p. 443-50.

49. Adler, D.C., et al., *Photothermal detection of gold nanoparticles using phase-sensitive optical coherence tomography.* Opt Express, 2008. **16**(7): p. 4376-93.

References

50. Mieszawska, A.J., et al., *Multifunctional gold nanoparticles for diagnosis and therapy of disease.* Molecular pharmaceutics, 2013. **10**(3): p. 831-847.

51. Cai, Q.Y., et al., *Colloidal gold nanoparticles as a blood-pool contrast agent for X-ray computed tomography in mice.* Invest Radiol, 2007. **42**(12): p. 797-806.

52. Hainfeld, J.F., et al., *Gold nanoparticles: a new X-ray contrast agent.* Br J Radiol, 2006. **79**(939): p. 248-53.

53. Haes, A.J., et al., *Detection of a biomarker for Alzheimer's disease from synthetic and clinical samples using a nanoscale optical biosensor.* J Am Chem Soc, 2005. **127**(7): p. 2264-71.

54. Mahmoud, K.A. and J.H. Luong, *Impedance method for detecting HIV-1 protease and screening for its inhibitors using ferrocene-peptide conjugate/Au nanoparticle/single-walled carbon nanotube modified electrode.* Anal Chem, 2008. **80**(18): p. 7056-62.

55. Baptista, P.V., et al., *Gold-nanoparticle-probe-based assay for rapid and direct detection of Mycobacterium tuberculosis DNA in clinical samples.* Clin Chem, 2006. **52**(7): p. 1433-4.

56. Cheng, Y., et al., *Delivery and efficacy of a cancer drug as a function of the bond to the gold nanoparticle surface.* Langmuir, 2010. **26**(4): p. 2248-55.

57. Cheng, Y., et al., *Highly efficient drug delivery with gold nanoparticle vectors for in vivo photodynamic therapy of cancer.* J Am Chem Soc, 2008. **130**(32): p. 10643-7.

58. Meyers, J.D., et al., *Peptide-Targeted Gold Nanoparticles for Photodynamic Therapy of Brain Cancer.* Part Part Syst Charact, 2015. **32**(4): p. 448-457.

59. Gannon, C.J., et al., *Intracellular gold nanoparticles enhance non-invasive radiofrequency thermal destruction of human gastrointestinal cancer cells.* J Nanobiotechnology, 2008. **6**: p. 2.

60. Bhattacharya, R. and P. Mukherjee, *Biological properties of "naked" metal nanoparticles.* Adv Drug Deliv Rev, 2008. **60**(11): p. 1289-306.

61. Zharov, V.P., et al., *Photothermal nanotherapeutics and nanodiagnostics for selective killing of bacteria targeted with gold nanoparticles.* Biophys J, 2006. **90**(2): p. 619-27.

62. Kelkar, S.S. and T.M. Reineke, *Theranostics: combining imaging and therapy.* Bioconjugate chemistry, 2011. **22**(10): p. 1879-1903.

63. Iyer, A.K., et al., *Exploiting the enhanced permeability and retention effect for tumor targeting.* Drug discovery today, 2006. **11**(17): p. 812-818.

64. Wu, X.Y. and P.I. Lee, *Preparation and characterization of thermal- and pH-sensitive nanospheres.* Pharm Res, 1993. **10**(10): p. 1544-7.

65. Phillips, M.A., M.L. Gran, and N.A. Peppas, *Targeted Nanodelivery of Drugs and Diagnostics.* Nano Today, 2010. **5**(2): p. 143-159.

References

66.   Paciotti, G.F., et al., *Colloidal gold: a novel nanoparticle vector for tumor directed drug delivery.* Drug Deliv, 2004. **11**(3): p. 169-83.

67.   Heo, D.N., et al., *Gold nanoparticles surface-functionalized with paclitaxel drug and biotin receptor as theranostic agents for cancer therapy.* Biomaterials, 2012. **33**(3): p. 856-66.

68.   Kawano, T., et al., *PNIPAM gel-coated gold nanorods for targeted delivery responding to a near-infrared laser.* Bioconjug Chem, 2009. **20**(2): p. 209-12.

69.   Jain, P.K., et al., *Noble metals on the nanoscale: optical and photothermal properties and some applications in imaging, sensing, biology, and medicine.* Accounts of chemical research, 2008. **41**(12): p. 1578-1586.

70.   Melancon, M.P., W. Lu, and C. Li, *Gold-based magneto/optical nanostructures: challenges for in vivo applications in cancer diagnostics and therapy.* MRS bulletin, 2009. **34**(06): p. 415-421.

71.   Mahmood, U. and R. Weissleder, *Near-infrared optical imaging of proteases in cancer.* Molecular cancer therapeutics, 2003. **2**(5): p. 489-496.

72.   Bandyopadhyay, S., et al., *Synthesis and in vitro cellular interactions of superparamagnetic iron nanoparticles with a crystalline gold shell.* Applied Surface Science, 2014. **316**: p. 171-178.

73.   Gilchrist, R., et al., *Selective inductive heating of lymph nodes.* Annals of surgery, 1957. **146**(4): p. 596.

74.   Kim, J., et al., *Designed fabrication of multifunctional magnetic gold nanoshells and their application to magnetic resonance imaging and photothermal therapy.* Angewandte Chemie, 2006. **118**(46): p. 7918-7922.

75.   Lim, Y.T., et al., *Plasmonic Magnetic Nanostructure for Bimodal Imaging and Photonic-Based Therapy of Cancer Cells.* ChemBioChem, 2007. **8**(18): p. 2204-2209.

76.   Sönnichsen, C., et al., *Drastic reduction of plasmon damping in gold nanorods.* Physical review letters, 2002. **88**(7): p. 077402.

77.   Chou, C.-H., C.-D. Chen, and C.C. Wang, *Highly efficient, wavelength-tunable, gold nanoparticle based optothermal nanoconvertors.* The journal of physical chemistry B, 2005. **109**(22): p. 11135-11138.

78.   Noguez, C. and A.L. González, *Localized Surface Plasmons of Multifaceted Metal Nanoparticles.* Complex-Shaped Metal Nanoparticles: Bottom-Up Syntheses and Applications: p. 361-393.

79.   Maier, S.A., et al., *Local detection of electromagnetic energy transport below the diffraction limit in metal nanoparticle plasmon waveguides.* Nature materials, 2003. **2**(4): p. 229-232.

80.   Camden, J.P., et al., *Controlled plasmonic nanostructures for surface-enhanced spectroscopy and sensing.* Accounts of chemical research, 2008. **41**(12): p. 1653-1661.

References

81.   Jin, R., et al., *Controlling anisotropic nanoparticle growth through plasmon excitation.* Nature, 2003. **425**(6957): p. 487-490.

82.   Atwater, H.A. and A. Polman, *Plasmonics for improved photovoltaic devices.* Nature materials, 2010. **9**(3): p. 205-213.

83.   Zhang, J.Z. and C. Noguez, *Plasmonic optical properties and applications of metal nanostructures.* Plasmonics, 2008. **3**(4): p. 127-150.

84.   Huang, X., et al., *Cancer cell imaging and photothermal therapy in the near-infrared region by using gold nanorods.* Journal of the American Chemical Society, 2006. **128**(6): p. 2115-2120.

85.   Noguez, C., *Surface plasmons on metal nanoparticles: the influence of shape and physical environment.* The Journal of Physical Chemistry C, 2007. **111**(10): p. 3806-3819.

86.   Hartschuh, A., *Tip-enhanced optical spectroscopy.* Philosophical Transactions of the Royal Society of London A: Mathematical, Physical and Engineering Sciences, 2004. **362**(1817): p. 807-819.

87.   Harris, D. and M. Bertolucci, *Symmetry and Spectroscopy: an introduction to vibrational and electronic spectroscopy. 1989.* Mineola, NY: Dover Publications.

88.   Jeanmaire, D.L. and R.P. Van Duyne, *Surface Raman spectroelectrochemistry: Part I. Heterocyclic, aromatic, and aliphatic amines adsorbed on the anodized silver electrode.* Journal of Electroanalytical Chemistry and Interfacial Electrochemistry, 1977. **84**(1): p. 1-20.

89.   Albrecht, M.G. and J.A. Creighton, *Anomalously intense Raman spectra of pyridine at a silver electrode.* Journal of the American Chemical Society, 1977. **99**(15): p. 5215-5217.

90.   Jäckel, F. and J. Feldmann, *Surface‐Enhanced Raman Scattering Using Complex‐Shaped Metal Nanostructures.* Complex-shaped metal nanoparticles: Bottom-up syntheses and applications, 2012: p. 429-454.

91.   Jain, P.K., I.H. El-Sayed, and M.A. El-Sayed, *Au nanoparticles target cancer.* nano today, 2007. **2**(1): p. 18-29.

92.   Stehr, J., et al., *Gold nanostoves for microsecond DNA melting analysis.* Nano letters, 2008. **8**(2): p. 619-623.

93.   Gobin, A.M., et al., *Near infrared laser‐tissue welding using nanoshells as an exogenous absorber.* Lasers in Surgery and Medicine, 2005. **37**(2): p. 123-129.

94.   El-Sayed, I.H., X. Huang, and M.A. El-Sayed, *Selective laser photo-thermal therapy of epithelial carcinoma using anti-EGFR antibody conjugated gold nanoparticles.* Cancer letters, 2006. **239**(1): p. 129-135.

95.   Baffou, G., R. Quidant, and C. Girard, *Heat generation in plasmonic nanostructures: Influence of morphology.* Applied Physics Letters, 2009. **94**(15): p. 153109.

References

96.   Mullin, J. and B.H. Crystallization, *Boston, 4th edn, 2001 Search PubMed;(b) X. Ge, SY Song and HJ Zhang.* CrystEngComm, 2012. **14**: p. 7306.

97.   Schladt, T.D., et al., *Synthesis and bio-functionalization of magnetic nanoparticles for medical diagnosis and treatment.* Dalton Transactions, 2011. **40**(24): p. 6315-6343.

98.   Liu, X., *Heterogeneous nucleation or homogeneous nucleation?* The Journal of Chemical Physics, 2000. **112**(22): p. 9949-9955.

99.   Mullin, J.W., *Crystallization.* 2001: Butterworth-Heinemann.

100. Olderøy, M.Ø., et al., *Growth and nucleation of calcium carbonate vaterite crystals in presence of alginate.* Crystal Growth & Design, 2009. **9**(12): p. 5176-5183.

101. De Yoreo, J.J. and P.G. Vekilov, *Principles of crystal nucleation and growth.* Reviews in mineralogy and geochemistry, 2003. **54**(1): p. 57-93.

102. Hulteen, J.C. and C.R. Martin, *A general template-based method for the preparation of nanomaterials.* Journal of Materials Chemistry, 1997. **7**(7): p. 1075-1087.

103. Liu, H., et al., *Dendrimer-mediated hydrothermal synthesis of ultrathin gold nanowires.* Scientific reports, 2013. **3**.

104. Jana, N.R., L. Gearheart, and C.J. Murphy, *Wet chemical synthesis of high aspect ratio cylindrical gold nanorods.* The Journal of Physical Chemistry B, 2001. **105**(19): p. 4065-4067.

105. Petroski, J.M., et al., *Kinetically controlled growth and shape formation mechanism of platinum nanoparticles.* The Journal of Physical Chemistry B, 1998. **102**(18): p. 3316-3320.

106. Murphy, C.J., et al., *Anisotropic metal nanoparticles: synthesis, assembly, and optical applications.* The Journal of Physical Chemistry B, 2005. **109**(29): p. 13857-13870.

107. Gao, J., C.M. Bender, and C.J. Murphy, *Dependence of the gold nanorod aspect ratio on the nature of the directing surfactant in aqueous solution.* Langmuir, 2003. **19**(21): p. 9065-9070.

108. Chen, H.M., et al., *Controlling length of gold nanowires with large-scale: X-ray absorption spectroscopy approaches to the growth process.* The Journal of Physical Chemistry C, 2007. **111**(50): p. 18550-18557.

109. Liu, M. and P. Guyot-Sionnest, *Mechanism of silver (I)-assisted growth of gold nanorods and bipyramids.* The Journal of Physical Chemistry B, 2005. **109**(47): p. 22192-22200.

110. Jana, N.R., L. Gearheart, and C.J. Murphy, *Seed-mediated growth approach for shape-controlled synthesis of spheroidal and rod-like gold nanoparticles using a surfactant template.* Advanced Materials, 2001. **13**(18): p. 1389.

111. Zhang, X., et al., *Synthesis and growth mechanism of pentagonal bipyramid-shaped gold-rich Au/Ag alloy nanoparticles.* Langmuir, 2007. **23**(11): p. 6372-6376.

References

112.   Kou, X., et al., *Growth of gold nanorods and bipyramids using CTEAB surfactant.* The Journal of Physical Chemistry B, 2006. **110**(33): p. 16377-16383.

113.   Xu, X., et al., *Hyaluronic acid-based hydrogels: from a natural polysaccharide to complex networks.* Soft Matter, 2012. **8**(12): p. 3280-3294.

114.   Laurent, T.C., U. Laurent, and J. Fraser, *Functions of hyaluronan.* Annals of the rheumatic diseases, 1995. **54**(5): p. 429.

115.   Segura, T., et al., *Crosslinked hyaluronic acid hydrogels: a strategy to functionalize and pattern.* Biomaterials, 2005. **26**(4): p. 359-371.

116.   Hahn, S.K., et al., *Anti-inflammatory drug delivery from hyaluronic acid hydrogels.* Journal of Biomaterials Science, Polymer Edition, 2004. **15**(9): p. 1111-1119.

117.   Choi, Y.S., et al., *Studies on gelatin‑containing artificial skin: II. Preparation and characterization of cross‑linked gelatin‑hyaluronate sponge.* Journal of biomedical materials research, 1999. **48**(5): p. 631-639.

118.   Duranti, F., et al., *Injectable hyaluronic acid gel for soft tissue augmentation.* Dermatologic surgery, 1998. **24**(12): p. 1317-1325.

119.   Lee, K.Y. and D.J. Mooney, *Hydrogels for tissue engineering.* Chemical reviews, 2001. **101**(7): p. 1869-1880.

120.   Perka, C., et al., *Matrix‑mixed culture: New methodology for chondrocyte culture and preparation of cartilage transplants.* Journal of biomedical materials research, 2000. **49**(3): p. 305-311.

121.   Fussenegger, M., et al., *Stabilized autologous fibrin-chondrocyte constructs for cartilage repair in vivo.* Annals of plastic surgery, 2003. **51**(5): p. 493-498.

122.   Ye, Q., et al., *Fibrin gel as a three dimensional matrix in cardiovascular tissue engineering.* European Journal of Cardio-Thoracic Surgery, 2000. **17**(5): p. 587-591.

123.   Mosesson, M., *Fibrinogen and fibrin structure and functions.* Journal of Thrombosis and Haemostasis, 2005. **3**(8): p. 1894-1904.

124.   Cao, Z., R.J. Gilbert, and W. He, *Simple Agarose− Chitosan gel composite system for enhanced neuronal growth in three dimensions.* Biomacromolecules, 2009. **10**(10): p. 2954-2959.

125.   Borkenhagen, M., et al., *Three‑dimensional extracellular matrix engineering in the nervous system.* Journal of biomedical materials research, 1998. **40**(3): p. 392-400.

126.   Xu, J., J. Bartley, and R. Johnson, *Preparation and characterization of alginate hydrogel membranes crosslinked using a water‑soluble carbodiimide.* Journal of applied polymer science, 2003. **90**(3): p. 747-753.

127.   Gombotz, W.R. and S.F. Wee, *Protein release from alginate matrices.* Advanced drug delivery reviews, 2012. **64**: p. 194-205.

References

128. Baysal, K., et al., *Chitosan/alginate crosslinked hydrogels: Preparation, characterization and application for cell growth purposes.* International journal of biological macromolecules, 2013. **59**: p. 342-348.

129. Palma Santana, B., et al., *Preparation, modification, and characterization of alginate hydrogel with nano-/microfibers: a new perspective for tissue engineering.* BioMed research international, 2013. **2013**.

130. MacGregor, E.A. and C.T. Greenwood, *Polymers in nature.* 1980: John Wiley & Sons.

131. Srivastava, S., S. Gorham, and J. Courtney, *The attachment and growth of an established cell line on collagen, chemically modified collagen, and collagen composite surfaces.* Biomaterials, 1990. **11**(3): p. 162-168.

132. Auger, F., et al., *Tissue-engineered human skin substitutes developed from collagen-populated hydrated gels: clinical and fundamental applications.* Medical and Biological Engineering and Computing, 1998. **36**(6): p. 801-812.

133. Seliktar, D., et al., *Dynamic mechanical conditioning of collagen-gel blood vessel constructs induces remodeling in vitro.* Annals of biomedical engineering, 2000. **28**(4): p. 351-362.

134. Alfaro, A.D.T., et al., *Physical and chemical properties of wami tilapia skin gelatin.* Food Science and Technology (Campinas), 2013. **33**(3): p. 592-595.

135. Kuijpers, A., et al., *Characterization of the network structure of carbodiimide cross-linked gelatin gels.* Macromolecules, 1999. **32**(10): p. 3325-3333.

136. Choi, Y.S., et al., *Study on gelatin-containing artificial skin: I. Preparation and characteristics of novel gelatin-alginate sponge.* Biomaterials, 1999. **20**(5): p. 409-417.

137. Bhattarai, N., J. Gunn, and M. Zhang, *Chitosan-based hydrogels for controlled, localized drug delivery.* Advanced drug delivery reviews, 2010. **62**(1): p. 83-99.

138. Kumar, M.R., et al., *Chitosan chemistry and pharmaceutical perspectives.* Chemical reviews, 2004. **104**(12): p. 6017-6084.

139. Chenite, A., et al., *Novel injectable neutral solutions of chitosan form biodegradable gels in situ.* Biomaterials, 2000. **21**(21): p. 2155-2161.

140. Yuan, Y., et al., *The effect of cross-linking of chitosan microspheres with genipin on protein release.* Carbohydrate Polymers, 2007. **68**(3): p. 561-567.

141. Ono, K., et al., *Photocrosslinkable chitosan as a biological adhesive.* Journal of biomedical materials research, 2000. **49**(2): p. 289-295.

142. Kidane, A., J.M. Szabocsik, and K. Park, *Accelerated study on lysozyme deposition on poly (HEMA) contact lenses.* Biomaterials, 1998. **19**(22): p. 2051-2055.

143. Lu, S. and K.S. Anseth, *Photopolymerization of multilaminated poly (HEMA) hydrogels for controlled release.* Journal of Controlled Release, 1999. **57**(3): p. 291-300.

References

144. Stubbe, B., et al., *Swelling pressure observations on degrading dex-HEMA hydrogels.* Macromolecules, 2002. **35**(7): p. 2501-2505.

145. Lahooti, S. and M.V. Sefton, *Methods for microencapsulation with HEMA-MMA.* Tissue Engineering Methods and Protocols, 1999: p. 331-348.

146. Peppas, N.A. and E.W. Merrill, *Development of semicrystalline poly (vinyl alcohol) hydrogels for biomedical applications.* Journal of Biomedical Materials Research, 1977. **11**(3): p. 423-434.

147. Martens, P.J., S.J. Bryant, and K.S. Anseth, *Tailoring the degradation of hydrogels formed from multivinyl poly (ethylene glycol) and poly (vinyl alcohol) macromers for cartilage tissue engineering.* Biomacromolecules, 2003. **4**(2): p. 283-292.

148. Shaheen, S.M. and K. Yamaura, *Preparation of theophylline hydrogels of atactic poly (vinyl alcohol)/NaCl/H 2 O system for drug delivery system.* Journal of controlled release, 2002. **81**(3): p. 367-377.

149. Nguyen, K.T. and J.L. West, *Photopolymerizable hydrogels for tissue engineering applications.* Biomaterials, 2002. **23**(22): p. 4307-4314.

150. Buwalda, S.J., et al., *Hydrogels in a historical perspective: From simple networks to smart materials.* Journal of controlled release, 2014. **190**: p. 254-273.

151. Merrill, E., et al., *Platelet-compatible hydrophilic segmented polyurethanes from polyethylene glycols and cyclohexane diisocyanate.* ASAIO Journal, 1982. **28**(1): p. 482-487.

152. West, J.L. and J.A. Hubbell, *Photopolymerized hydrogel materials for drug delivery applications.* Reactive Polymers, 1995. **25**(2): p. 139-147.

153. Ratner, B.D., et al., *Biomaterials science: an introduction to materials in medicine.* 2004: Academic press.

154. Whitesides, G.M., et al., *Soft lithography in biology and biochemistry.* Annual review of biomedical engineering, 2001. **3**(1): p. 335-373.

155. Hern, D.L. and J.A. Hubbell, *Incorporation of adhesion peptides into nonadhesive hydrogels useful for tissue resurfacing.* Journal of biomedical materials research, 1998. **39**(2): p. 266-276.

156. West, J.L. and J.A. Hubbell, *Polymeric biomaterials with degradation sites for proteases involved in cell migration.* Macromolecules, 1999. **32**(1): p. 241-244.

157. Jeong, B., S.W. Kim, and Y.H. Bae, *Thermosensitive sol–gel reversible hydrogels.* Advanced drug delivery reviews, 2002. **54**(1): p. 37-51.

158. Dong, L.-c. and A.S. Hoffman, *A novel approach for preparation of pH-sensitive hydrogels for enteric drug delivery.* Journal of Controlled Release, 1991. **15**(2): p. 141-152.

159. Fisher, R. and B.E. Pettet, *Presbyopia and the water content of the human crystalline lens.* The Journal of physiology, 1973. **234**(2): p. 443.

References

160.   Liu, W., et al., *Collagen–phosphorylcholine interpenetrating network hydrogels as corneal substitutes.* Biomaterials, 2009. **30**(8): p. 1551-1559.

161.   Zhang, Q., et al., *High refractive index inorganic–organic interpenetrating polymer network (IPN) hydrogel nanocomposite toward artificial cornea implants.* ACS Macro Letters, 2012. **1**(7): p. 876-881.

162.   Rueda, J.C., et al. *Characterization of new thermo-responsive hydrogels for optical sensing applications*. in *Defense and Security Symposium*. 2007. International Society for Optics and Photonics.

163.   Wedgwood, J., A.J. Freemont, and N. Tirelli. *Rheological and Turbidity Study of Fibrin Hydrogels*. in *Macromolecular Symposia*. 2013. Wiley Online Library.

164.   Qiu, Y. and K. Park, *Environment-sensitive hydrogels for drug delivery.* Advanced drug delivery reviews, 2012. **64**: p. 49-60.

165.   Okay, O., *General properties of hydrogels*, in *Hydrogel sensors and actuators*. 2009, Springer. p. 1-14.

166.   Shiga, T., et al., *Electric field-associated deformation of polyelectrolyte gel near a phase transition point.* Journal of applied polymer science, 1992. **46**(4): p. 635-640.

167.   Schild, H.G., *Poly (N-isopropylacrylamide): experiment, theory and application.* Progress in polymer science, 1992. **17**(2): p. 163-249.

168.   Falamarzian, M. and J. Varshosaz, *The effect of structural changes on swelling kinetics of polybasic/hydrophobic pH-sensitive hydrogels.* Drug development and industrial pharmacy, 1998. **24**(7): p. 667-669.

169.   Kou, J.H., G.L. Amidon, and P.I. Lee, *pH-Dependent Swelling and Solute Diffusion Characteristics of Poly (Hydroxyethyl Methacrylate–CO–Methacrylie Acid) Hydrogels.* Pharmaceutical research, 1988. **5**(9): p. 592-597.

170.   Hoare, T.R. and D.S. Kohane, *Hydrogels in drug delivery: progress and challenges.* Polymer, 2008. **49**(8): p. 1993-2007.

171.   Lim, D.W., et al., *Rapid cross-linking of elastin-like polypeptides with (hydroxymethyl) phosphines in aqueous solution.* Biomacromolecules, 2007. **8**(5): p. 1463-1470.

172.   Chen, P., *Self-assembly of ionic-complementary peptides: a physicochemical viewpoint.* Colloids and Surfaces A: Physicochemical and Engineering Aspects, 2005. **261**(1): p. 3-24.

173.   Wu, J., Z.-G. Su, and G.-H. Ma, *A thermo-and pH-sensitive hydrogel composed of quaternized chitosan/glycerophosphate.* International Journal of Pharmaceutics, 2006. **315**(1): p. 1-11.

174.   Liu, J., et al., *Release of theophylline from polymer blend hydrogels.* International journal of pharmaceutics, 2005. **298**(1): p. 117-125.

175.   Jin, R., et al., *Enzyme-mediated fast in situ formation of hydrogels from dextran–tyramine conjugates.* Biomaterials, 2007. **28**(18): p. 2791-2800.

References

176. Kurisawa, M., et al., *Injectable biodegradable hydrogels composed of hyaluronic acid–tyramine conjugates for drug delivery and tissue engineering.* Chemical communications, 2005(34): p. 4312-4314.

177. Kakinoki, S., et al., *Injectable in situ forming drug delivery system for cancer chemotherapy using a novel tissue adhesive: characterization and in vitro evaluation.* European journal of pharmaceutics and biopharmaceutics, 2007. **66**(3): p. 383-390.

178. Butler, M.F., Y.F. Ng, and P.D. Pudney, *Mechanism and kinetics of the crosslinking reaction between biopolymers containing primary amine groups and genipin.* Journal of Polymer Science Part A: Polymer Chemistry, 2003. **41**(24): p. 3941-3953.

179. Nishi, K. and A. Jayakrishnan, *Preparation and in vitro evaluation of primaquine-conjugated gum arabic microspheres.* Biomacromolecules, 2004. **5**(4): p. 1489-1495.

180. Hiemstra, C., et al., *Novel in situ forming, degradable dextran hydrogels by Michael addition chemistry: synthesis, rheology, and degradation.* Macromolecules, 2007. **40**(4): p. 1165-1173.

181. Elbert, D.L., et al., *Protein delivery from materials formed by self-selective conjugate addition reactions.* Journal of Controlled Release, 2001. **76**(1): p. 11-25.

182. Shu, X.Z., et al., *Synthesis and evaluation of injectable, in situ crosslinkable synthetic extracellular matrices for tissue engineering.* Journal of Biomedical Materials Research Part A, 2006. **79**(4): p. 902-912.

183. Cai, S., et al., *Injectable glycosaminoglycan hydrogels for controlled release of human basic fibroblast growth factor.* Biomaterials, 2005. **26**(30): p. 6054-6067.

184. Zhang, F., et al., *Gold nanoparticles decorated with oligo (ethylene glycol) thiols: protein resistance and colloidal stability.* The Journal of Physical Chemistry A, 2007. **111**(49): p. 12229-12237.

185. Otsuka, H., Y. Nagasaki, and K. Kataoka, *PEGylated nanoparticles for biological and pharmaceutical applications.* Advanced drug delivery reviews, 2003. **55**(3): p. 403-419.

186. Wu, W., et al., *Core–shell hybrid nanogels for integration of optical temperature-sensing, targeted tumor cell imaging, and combined chemo-photothermal treatment.* Biomaterials, 2010. **31**(29): p. 7555-7566.

187. Wu, X., Y. Gao, and C.-M. Dong, *Polymer/gold hybrid nanoparticles: from synthesis to cancer theranostic applications.* RSC Advances, 2015. **5**(18): p. 13787-13796.

188. Kirui, D.K., D.A. Rey, and C.A. Batt, *Gold hybrid nanoparticles for targeted phototherapy and cancer imaging.* Nanotechnology, 2010. **21**(10): p. 105105.

189. Nayak, S. and L.A. Lyon, *Soft nanotechnology with soft nanoparticles.* Angewandte chemie international edition, 2005. **44**(47): p. 7686-7708.

190. Kaszuba, M., et al., *Measuring sub nanometre sizes using dynamic light scattering.* Journal of Nanoparticle Research, 2008. **10**(5): p. 823-829.

References

191. Instruments, L. *Dynamic Light Scattering: Measuring the Particle Size Distribution*. 2015 [cited 2015 15 June].

192. Koppel, D.E., *Analysis of macromolecular polydispersity in intensity correlation spectroscopy: the method of cumulants.* The Journal of Chemical Physics, 1972. **57**(11): p. 4814-4820.

193. Davis, U. *Spectrophotometry*. [cited 2015 15 June].

194. Nellist, P.D., *The principles of STEM imaging*, in *Scanning Transmission Electron Microscopy*. 2011, Springer. p. 91-115.

195. Egerton, R., *Physical principles of electron microscopy: an introduction to TEM, SEM, and AEM*. 2006: Springer Science & Business Media.

196. Fuciños, C., et al., *Temperature-and pH-sensitive nanohydrogels of poly (N-isopropylacrylamide) for food packaging applications: modelling the swelling-collapse behaviour.* PloS one, 2014. **9**(2): p. e87190.

197. Chakraborty, C., et al., *Nanoparticles as' smart'pharmaceutical delivery.* Frontiers in bioscience (Landmark edition), 2012. **18**: p. 1030-1050.

198. Smith, M.H. and L.A. Lyon, *Multifunctional nanogels for siRNA delivery.* Accounts of chemical research, 2011. **45**(7): p. 985-993.

199. Hossen, M.N., et al., *Therapeutic assessment of cytochrome c for the prevention of obesity through endothelial cell-targeted nanoparticulate system.* Molecular Therapy, 2013. **21**(3): p. 533-541.

200. Andersen, M.K., *Polymeric Hydrogels for Drug Delivery*. 2014, Norwegian University of Science and Technology: Trondheim.

201. Alvi, M.A.A., *Polymer-Nanoparticle Hybrids For Drug Delivery Applications*. 2015, Norwegian University of Science and Technology: Trondheim.

202. Hamidi, M., A. Azadi, and P. Rafiei, *Hydrogel nanoparticles in drug delivery.* Advanced drug delivery reviews, 2008. **60**(15): p. 1638-1649.

203. Amsden, B., *Solute diffusion within hydrogels. Mechanisms and models.* Macromolecules, 1998. **31**(23): p. 8382-8395.

204. Canal, T. and N.A. Peppas, *Correlation between mesh size and equilibrium degree of swelling of polymeric networks.* Journal of biomedical materials research, 1989. **23**(10): p. 1183-1193.

205. Mason, M.N., et al., *Predicting controlled-release behavior of degradable PLA-b-PEG-b-PLA hydrogels.* Macromolecules, 2001. **34**(13): p. 4630-4635.

206. Siepmann, J. and N. Peppas, *Modeling of drug release from delivery systems based on hydroxypropyl methylcellulose (HPMC).* Advanced drug delivery reviews, 2012. **64**: p. 163-174.

207. Bettini, R., et al., *Swelling and drug release in hydrogel matrices: polymer viscosity and matrix porosity effects.* European Journal of Pharmaceutical Sciences, 1994. **2**(3): p. 213-219.

208. Barzegar-Jalali, M., et al., *Kinetic analysis of drug release from nanoparticles.* Journal of Pharmacy and Pharmaceutical Sciences, 2008. **11**(1): p. 167-177.

209. Costa, P. and J.M.S. Lobo, *Modeling and comparison of dissolution profiles.* European journal of pharmaceutical sciences, 2001. **13**(2): p. 123-133.

210. Jain, P.K., et al., *Calculated absorption and scattering properties of gold nanoparticles of different size, shape, and composition: applications in biological imaging and biomedicine.* The Journal of Physical Chemistry B, 2006. **110**(14): p. 7238-7248.

211. McDonagh, B.H., et al., *Controlling the self-assembly and optical properties of gold nanoclusters and gold nanoparticles biomineralized with bovine serum albumin.* RSC Advances, 2015. **5**(122): p. 101101-101109.